Alma Mater Studiorum – Università di Bologna

DOTTORATO DI RICERCA IN

SCIENZE DELLA TERRA DELLA VITA E DELL'AMBIENTE

Ciclo XXXII

Settore Concorsuale: 04/A3

Settore Scientifico Disciplinare: GEO/05

Study of the dynamic behavior of earthflows, with particular reference to the solid-to-fluid transition characterizing stages of rapid movement

Presentata da: Gabriela Squarzoni

Coordinatore Dottorato **Supervisore**

Prof. Giulio Viola **Prof. Matteo Berti**

Esame finale anno 2020

ABSTRACT

Earthflows are landslide developing in clay-rich soil, characterized by elongated tongue-like shapes. They alternate periods of very slow motion (from millimeters to meters per year) with periods of rapid movement (from meters per day to meters per hour). Their behavior has been largely debated in literature. In particular, the periods of rapid motion have been interpreted in two different ways. Some authors suggest that, in spite of their flow-like morphology, earthflows essentially move like rigid bodies along well-defined slip surfaces. Other authors report that during the surging earthflow material becomes softer and can be considered as a viscous fluid. However, collecting data during the stages of rapid motion is still challenging and only minimal data concerning the real acceleration stage had been presented in literature. The purpose of the current study is to provide an insight into the reactivation stage in order to understand if any fluidization process can occur. Geophysical data have been treated: seismic surface wave techniques have been applied to detect shear stiffness variation over time in the periods near the rapid surging and two-pass conventional interferometry has been used to monitor landslide deformation patterns. Seismic data indicate that earthflow soils are affected by stiffness drops during the acceleration stage; the process is slowly reversed in the period following the rapid motion during which the materials become stiffer. This process is probably related to changes in void ratio and soil water content: after the failure the water content decreases, and the porosity of the soils decreases too. The data demonstrate that during the stages of rapid motion earthflows behave like viscous fluids; far from the failure they turn to be stiff and a rigid-like behavior is more likely. Mathematical theories can be used to fully describe the behavior but different types of field data concerning the rapid motion stage are necessary: to obtain a whole dataset we need to know in advance information about earthflow reactivation. For this reason, remote sense techniques have been tested in earthflows monitoring: conventional two-pass interferometry has been successfully applied to derive deformation patterns. Displacements information about two relatively-fast earthflows has been obtained: it's possible to detect the landslide areas before the reactivation occurring and pattern of deformation for very long periods before the rapid surging.

Contents

1. Introduction…… 1

State of the art…… 1

Motivation and focus of the current study……4

Study area…… 7

General guide through the thesis…… 12

References…… 14

2. Methodological notes…… 17

Seismic surveys…… 17

InSAR surveys…… 19

References…… 21

3. Paper 1: Dynamics of an active earthflow inferred from surface wave monitoring…… 25

4. Paper 2: Surface-wave velocity measurements of shear stiffness of moving earthflows…… 51

5. Methodological aspects about earthflows behavior interpretation…… 69

Iverson model…… 69

Assessing the Iverson model application……78

References…… 87

6. Paper 3: Pre and post failure behaviour of landslides in the Northern Apennines revealed by space-borne synthetic aperture radar interferometry (InSAR) …… 91

7. Conclusions…… 118

References…… 121

A) Appendix A: Acceleration point detection…… 122

B) Appendix B: Frames analysis…… 125

References…… 128

1. INTRODUCTION

State of the art

In the current document, I present the contents and the main findings of my PhD project. The work focuses on the dynamic behavior of earthflows. The purpose of this study is to understand the evolution of the earthflows through time, with particular reference to the activation/reactivation stage.

Earthflows are particular types of landslide (Figure 1.1). Following the most common classifications, they are defined as flow of slow to very rapid velocity involving mostly fine-grained material (Varnes, 1958; Cruden and Varnes 1996; Hungr et al., 2001; Hungr et al., 2014). They move intermittently forming a tongue-like shape (Figure 1.2). Continued movement may be maintained over long distances and periods of time; these periods are commonly interrupted by shorter periods of acceleration (e.g. Varnes, 1958; Keefer and Johnson, 1983; Hungr et al., 2001, Piccareli et al., 2005). Most earthflows move faster during periods of snowmelt or high precipitation than during drier seasons but the correlation between precipitation and velocity is complex (e.g. Keefer and Johnson, 1983; Iverson and Major, 1987; Berti et al. 2012).

Figure 1.1: Examples of earthflows in the Emilia Romagna region (Italy): on the left Marano earthflow (Bologna province) some days after the reactivation, on the right Montevecchio earthflow (Forlì-Cesena province).

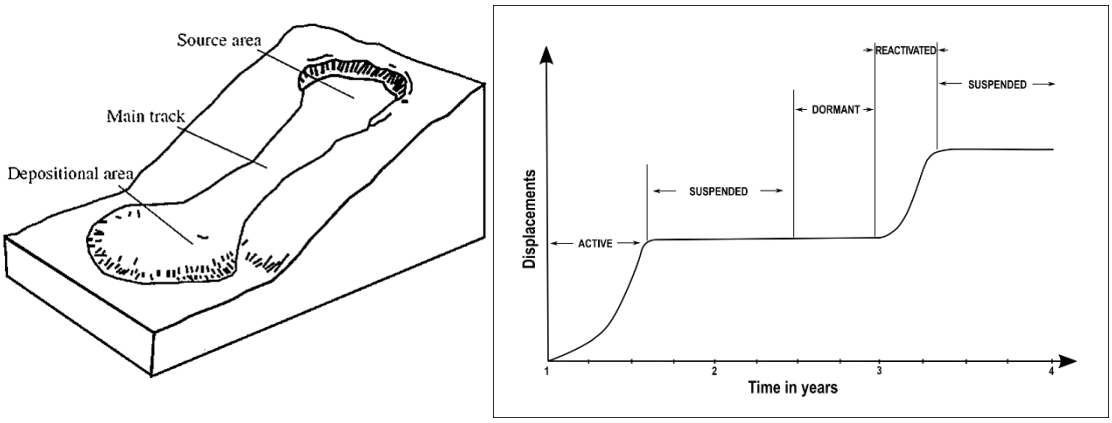

Figure 1.2: On the left, sketch of a typical earthflow; on the right earthflow pattern over time (Cruden and Varnes, 1996)

The term "earth" has been used in contrast with "debris" for indicating the weathering products of stiff clays and clayey rocks (Varnes, 1978). Other authors refer to earthflows by using different terminology (Hutchinson, 1988). However, earthflows occur in plastic, disturbed, and mixed soils, whose consistency is close to the Plastic Limit (Terzaghi and Peck, 1948, cited in Varnes, 1958; Keefer and Johnson, 1983). The source can be one or a series of rotational or compound slides. After the failure, the earthflow mass softens, and material moves downslope taking the typical tongue-like shape. Many earthflow tongues remain in a dormant state for many decades, allowing roads and buildings to be built on them. Acceleration ("surging") occurs when the source slide becomes destabilized, usually by a temporary increase in pore pressure (Keefer and Johnson, 1983; Hungr et al., 2014). Typical movement velocities are measured in meters per day during surges and millimeters per year in dormant stages (e.g. Keefer and Johnson, 1983; Picarelli et al. 2005).

Earthflow morphology is characterized by a rounded toe and a longitudinal profile which is concave upward near the head and convex upward near the toe. Such morphology suggests that earthflow movement involves a component of fluid-like flow; however other features, as bounding or internal shear surfaces, suggest that earthflows behave like rigid bodies. Keefer and Johnson (1983) observe the presence of numerous cracks inside the earthflows mass, well-defined lateral boundaries, and other rigid-like morphologies, but at the same time they notice that in the active earthflows "the material became so soft throughout that it would not support a person's weight" (Keefer and Johnson, 1983). Since the early study outcomes, the dynamic of the earthflow motion has been largely debated.

Keefer and Johnson (1983) conclude that, although some internal deformation occurs within earth flows, most movement takes place on or immediately adjacent to their boundaries. The thesis is

supported by different authors (Fleming et al. 1989; Baum et al. 2003; Schulz et al. 2009; Handwerger et al., 2015; Shulz et al., 2018). For example, Baum et al. (2003) remark that discrete lateral boundaries are typical of slow earthflows and most of them move primarily by sliding on discrete basal and lateral slip surfaces; distributed internal shear deformation contributes to the appearance of flowing movement.

Since many research papers underline the behavior described above, the same landslide classification had been discussed for validating a new term dealing with the sliding mechanism. In 1988, Hutchinson proposed a new classification that can properly deal with sliding behavior of the earthflows: he referred to earthflows using the term “mudslides” highlighting the presence of a translational component of the motion (Hutchinson, 1988). Also in the latest classifications the sliding component plays an important role: Hungr and colleagues define earthflows as flow-like movements facilitated by a combination of sliding along multiple discrete shear surfaces, and internal shear strains. The deformations are concentrated on the main shear surface during the steady motion phases and are distributed on internal “imbricate thrusts” during surges (Hungr et al., 2014).

Conversely, other interpretations exist: studies report that in some cases the distribution of velocities in the displacement mass resembles that of a viscous fluid and the earthflows propagation is associated with a significant increase in water content (Keefer and Johnson, 1983; Cruden and Varnes, 1996). Starting from this evidence some authors studied the earthflow behavior assessing the influence of a real flow component during the mobilization. Picarelli (2000) and Picarelli et al. (2005) state that after a rigid-like failure process, the soil fabric changes and, even if the parent formation is a stiff clay, it deteriorates and becomes a softened clay. The infiltration of the rainwater takes part in this process: the water can infiltrate in the earthflow cracks and contribute to remold the soil structure. The change of fabric and properties of the soil led to a flow developing.

Other studies (Mainsant et al., 2012; Jongmans et al., 2015) have been carried out by investigating the soil stiffness of the earthflow bodies in the periods near to the reactivation. These authors observe that the stiffness decreases during the earthflow acceleration leading to think about a sort of “solid-to-fluid transition” in which stiffness drop indicates the incoming of a fluid phase. Specifically, they used seismic properties of the soil to monitor the soil stiffness trend over time: they gathered data continuously for large periods and recorded stiffness variation just before and after the earthflow accelerations. During the hours before the reactivations, they detected stiffness decreases and, in the period after the reactivation, they observed a slow increase in the

stiffness values. They interpreted this behavior as a consequence of water content variation which leads to a change in the soil properties of the earthflow: when the water content increase (due to intense precipitations or snow melting processes) the soil loses the rigid structure and it starts to behave like a viscous fluid. So, during the reactivation, it really flows downslope. After the main surge, it starts to slow down and the water content decreases so that it can return rigid again.

Motivation and focus of the current study

It's quite evident that a univocal interpretation for such type of mass movement is hard to be provided. In any case, water certainly plays a key role. A pore-water pressure rise decreases the effective stress, thus the shear strength of the soil. In the former hypothesis (i.e. rigid-like behavior), pore-pressure increase leads to the developing of one or more bounded slip surfaces (Keefer and Johnson, 1983; Angeli et al., 1996; Hungr et al., 2001). In the latter hypothesis (i.e. flow-like behavior), beside the pore-water pressure influence, the soil water content should be considered: the water infiltration contributes to remold the soils and results in a decrease of stiffness (Picarelli, 2000; Mainsant et al., 2015).

Thus, the question remains open: do the earthflows move on well-defined slip surfaces or during the failure something happens and the soils change their properties? Is the typical tongue-like shape a consequence of a complex rigid-like behavior or a result of a real flow?

This topic is the main part of the PhD work. In particular, we focused on the solid-to-fluid transition that can affect the earthflow evolution during the reactivation, studying the process by means of field monitoring and geophysical investigation. Seismic surface shear wave data have been gathered to study the soil stiffness variation over time of a few earthflows of the Emilia-Romagna region (Italy). In Paper 1, we collected and analyzed continuous data concerning the Montevecchio earthflow (Forlì-Cesena province) during the reactivation and the close periods in order to asses changes in the soil properties: we derived stiffness trend over time and identified drops in stiffness values during the rapid surging. Periodic acquisitions were also carried out by using a slightly different technique: they validated the continuous data and allow to compare the measurements of the flowing mass with measurements concerning the "outside" soils not involved in the failure. My contribution to Paper 1 can be found in the interpretation and analysis of the data regarding the continuous acquisitions, both for which concern the series derived from the time-lapse camera acquisitions and for which concern some of the elaborations about the seismic data. The data

presented in this paper were gathered before my PhD started so that there is no personal contribution in this sense. On the other hand, I participated in the paper preparation and writing.

Periodic seismic acquisitions have been taken also for other landslides in the study area (Paper 2). Different types of landslides have been investigated and shear wave data compared: earthflows shear wave velocities tend to increase in the period after the failure, whereas the rockslides shear wave velocities do not. The earthflow shear velocity trends over time have been interpreted as void ratio trends by using empirical correlations (Santo and Correia, 2000). My contribution in this paper is larger than in the previous one: I collected the last part of the data of each series, helped in the paper preparation both for which concern the presentation of the data, the methodology, the results, and the discussion and for which concern the mathematical elaboration of the data.

In both these works (Paper 1 and Paper 2) we studied the variations of the seismic surface wave velocity over time by collecting Rayleigh wave data. The acquisitions were performed using Refraction Microtremors (ReMi) technique (Louie, 2001) and MASW (Multichannel Analysis of Surface Waves) technique (Park et al. 1999). Both exploit seismic signal arrives in order to derive Rayleigh wave velocity: as they travel faster or slower depending on the material properties it's possible to infer the stiffness of the soils. The main difference between the two techniques relies on the type of source causing the seismic signal: if there is a specific induced source, we are dealing with MASW surveys, otherwise if signal is produced only by surround noise (e.g., wind, people/cars transition, etc.) we are dealing with ReMi surveys. The latter technique has been applied to obtain continuous measurements (Paper 1); for periodical acquisitions, both techniques have been applied (Paper 1 and 2).

The results presented in the papers seem to fit quite well with the hypothesis of real flow-like behavior in the reactivation stage. The mass is fluidized during the rapid motion and slowly turns to be stiffer in the following period. In any case, several months or years occur before it really stops moving. The stiffness increases rapidly so that it reaches values close to the pre-failure ones before the earthflows are stabilized. Thus, our basic idea is that the fluidization process concerns only a particular stage of the earthflow evolution. After the rapid surging the fluidization process is reversed, and the mass becomes more similar to a rigid body. Other kinds of data can be exploited in this sense: exploring the velocity distribution of the earthflow mass in different periods helps to understand how the behavior can change; this one is the aim of the not yet published research presented in the second part of the thesis. The link between the seismic measurements presented in Paper 1 and 2 and the consequent researches can not be entirely understood if we don't consider that we are dealing with a very wide and complex topic that can

be faced from different points of view. Thus, we need a large perspective in order to be aware of all the aspects of the problem and having a large perspective means to integrate different approaches, as it will be shown in the following.

Iverson (1985, 1986a, 1986b) proposed a physically based mathematical theory that can explain the entire earthflow evolution. What emerges from our unpublished research (Chapter 5) is that Iverson's theory probably is consistent with the behavior of the studied landslides in the Emilia Romagna region. However, gathering data during the reactivation period is the real challenge. We need information about the incoming earthflow reactivations in order to be prepared to collect data during the rapid surging, otherwise the risk is to install devices and to carry out surveys only once the main event already happened. This information needs can be overcome by monitoring landslide-prone areas using techniques leading to large datasets collection and relatively low-cost expense. Remote sensing techniques result in gathering a lot of data over wide regions with low cost-effectiveness: they can be a useful instrument to solve the data needs problem.

Specifically, satellite interferometry can be used to monitor large areas over long periods: it allows us to know if the interested area is moving, how it's moving, and if the motion is continuous both in time and space at a very low-cost benefits-ratio. Like everything else, it presents also some disadvantages that partially depend on the type of motion you want to detect and on the type of interferometry technique you want to use. Since many interferometry techniques exist, and landslide movements are different from type to type, adapting the correct technique to the proper problem is the main challenge of the investigating approach. For this reason, in Paper 3 we tested satellite two-pass interferometry to two earthflows that recently reactivated.

Synthetic aperture radar interferometry (InSAR) is a well-known interferometry technique that provides the possibility to measure small displacements on the ground surface and had been widely used to retrieve spatial and temporal deformations of slopes (e.g. Colesanti et al., 2003; Handwerger et al., 2015; Bayer et al., 2018). For our purposes, the only limit of this technique is related to the high velocity that characterizes the Emilia-Romagna earthflows: even in the periods between reactivations, during which the mass slows down, the earthflows velocity is relatively high and leads phase discontinuity and consequent errors (Notti et al., 2011; Wasowski and Bovenga, 2014). The launch of Sentinel satellite missions helped in overcoming the limitation relating to the fast movements. We used the Sentinel satellite data to perform conventional two-pass interferometry on Ca Lita (Reggio Emilia province) and Marano (Bologna province) earthflows. The conventional two-pass interferometry analysis enabled studying deformation patterns of the two landslides which were not detectable by using more common InSAR

techniques as PS-InSAR (Permanent Scatters InSAR; Ferretti et al., 2001) or SBAS (Small Baseline Subset; Berardino, 2011). PS-InSAR had been tested without any result because of the relatively high velocity displacements characterizing even the pre-failure and post-failure stages: in such conditions, the technique fails due to loss of coherence and consequent no permanent scatter detection (Wasoswski and Bonvenga, 2014). Using conventional InSAR, producing a large number of interferograms and manually selecting the valid ones allowed us to derive information about spatial and temporal distribution of the displacements of the earthflows where the other InSAR techniques can not work properly.

Study area

The research project has been developed investigating different landslides located in the Emilia-Romagna side of the Northern Apennines (Figure 1.3).

The mountainous part of the Emilia-Romagna region is made up of weak rock types, with abundant or prevailing clayey component and is interested by an active tectonic uplift and by intense weathering processes that lead the accumulation of various types of deposits. Among all the deposits types, the landslide bodies are the most common in this part of the Apennines: most of them derive from complex slides, associating roto-transitional slides with earthflows. Typical velocities are millimeters to centimeters per year during the long dormant stages and may increase up to meters per hour during paroxysm. The region is characterized by a Mediterranean climate with separate seasons: spring and fall are the rainiest periods so that 75% of total rainfalls occur during that time (Bertolini and Pellegrini, 2001).

The primary cause of earthflow developing in this region has been recognized in weather conditions such as snow melting and, mainly, rainfall occurrences (Bertolini and Pellegrini, 2001; Bertolini et al, 2004). Several cases are reported in literature (see, for example, Corsini et al., 2006; Berti and Simoni, 2012). In some cases, other possible factors can be considered as triggering conditions. Keefer (1984; 2002) studied a large number of landslides and their relationship with the seismic activity of the nearer areas; he inferred that the correlation between earthquake occurrences and landslide event can be significant only if the earthquake magnitude is higher than M = 4. The size of the area that can be interested in an earthquake-generated landslide depends on the same shomagnitude. Tosatti et al. (2008) provided an interesting description of 18 landslides that occurred in the Emilia Romagna region after seismic events, from the eighteen century to the last decade: eleven of them were caused by the 1920 Garfagnana earthquake

(Magnitude = 6.5). He highlighted that also for this region the correlation between landslides triggering and seismic events largely depends on the magnitude, as previously stated by Keffer (1984): only earthquakes more powerful than M = 6 can affects areas further than 30/40 km from the epicenter. In our case we have no evidence about such events in the last decades (Figure 1.3).

Almost all the landslides to which we focused on are large landslides that activated/reactivated after very rainy periods (Figure 1.4): the total length of the displaced mass spans from 600 m (Montevecchio earthflow, Reggio Emilia province) to more than 3000 m (Valoria earthflow, Modena province); the only exception is the Puzzola earthflow (Bologna province) that is 300 m long. They develop along gentle slopes involving clayey lithologies (the main features are reported in Table 1). They are classified as reactivated earthflows (Cruden and Varnes, 1996).

Boceto earthflow develops in clay shales lithology (San Siro Shales Formation). It reactivated in 2014 after more than a hundred years of dormancy. The slope failed as roto-translational slide and evolved quickly as a flow. The earthflow deposits are fine-grained clay deriving from the bedrock weathering.

Ca Lita earthflow is located in a landslide-prone area. There, the involved lithologies belong to the Ligurian Units. In the very upper part, the hillslope is composed of flysch (Monghidoro Flysch Formation), whereas the rest is made of clay shales (Rio Cargnone Formation). Historically it reactivated several times: the failure typically develops as rock slide in the head zone and as earthflow in the middle and lower parts. The latter reactivations occurred in 2016 and 2017.

Marano is a reactivated earthflow. The bedrock geology is characterized by clay shales mélange (Palombini Shales Formation) that produces clay-rich soils when weathered. Before the 1996 activation, there were no signs of recent activity. In 2018, after a period of intense rainfalls and snowfalls, the landslide reactivated abruptly.

Montevecchio is a relatively small earthflow. It reactivated several times in the last century and the last period of activity started in 2014. The deposits are the results of the bedrock weathering process: the involved lithologies are silty clays belonging to the Colombacci Shales Formation.

Puzzola earthflow develops on sandy clayey soils. This is a small earthflow that occurred for the first time only in 2014. The triggering failure was caused by a small rotational slide that let the sediments move downslope in a massive flow.

Silla earthflow is located near to the Marano one. The bedrock lithology is the same (Palombini Shales Formation) and the deposits are very similar. It is a part of a large landslide complex that

covers a wide area (Simoni and Berti, 2007). In the last hundred years it reactivated twice: 1994 and 2014.

Valoria is the largest earthflow considered in this study. It is a complex earthflow that reactivated several times in the last century. It involves different lithologies belonging to the Ligurian Units, both arenaceous formations (Poggio Mezzature Formation) and clays ones (Palombini Shales Formation, Grizzana Morandi Shales Formation). The last reactivation stage started in 2009.

Data about three differently classified landslides have been considered in this study too (Sintria, Becusano, and Zattaglia; Figure 1.5; Table 1). They are rockslides developing in arenaceous rocks (Marnoso-Arenacea Formation): data about them have been treated for comparing the behaviors of the two different types of landslides.

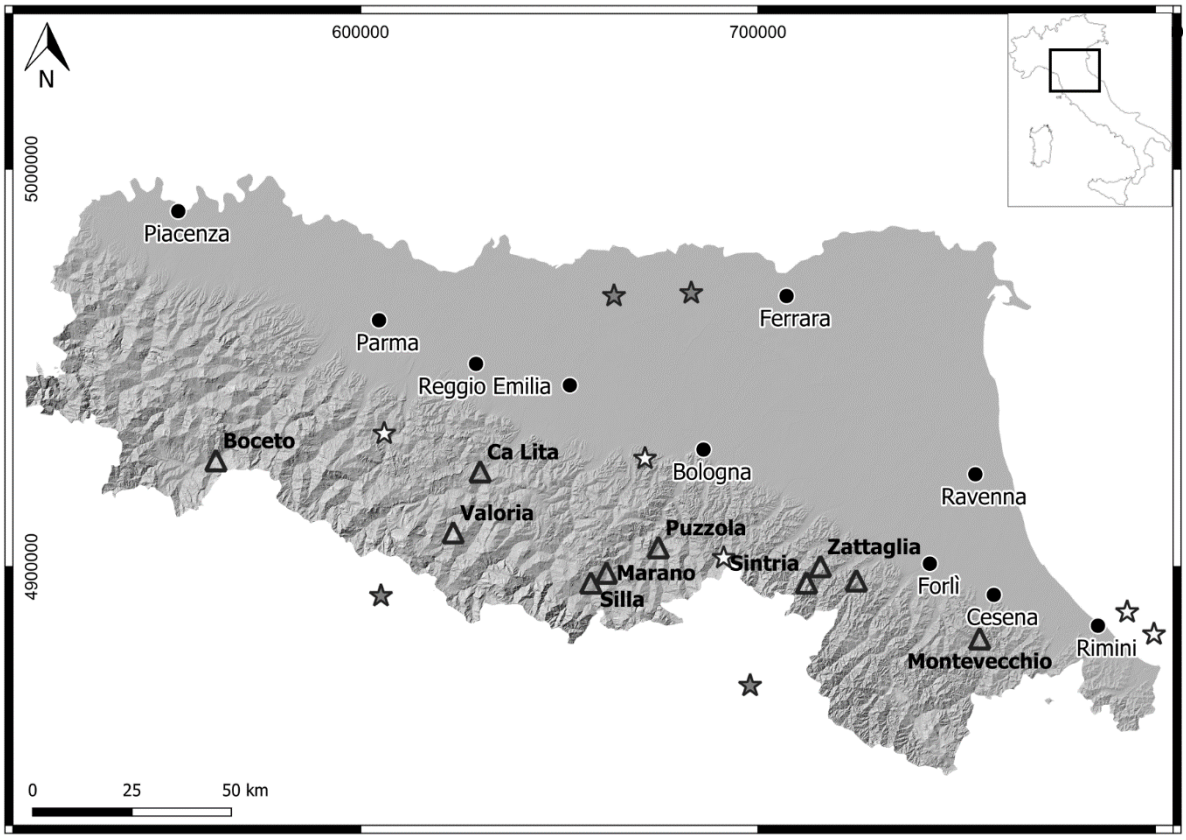

Figure 1.3: The location of the investigated earthflows is indicated by triangles: the names are the same as referred to in the text. The stars show the location of the earthquakes concerning the last century, in the region or the near areas of the Apennines: the white symbols state for 4 < M < 5.3 earthquakes, the grey symbols state for M > 5.3 earthquakes.

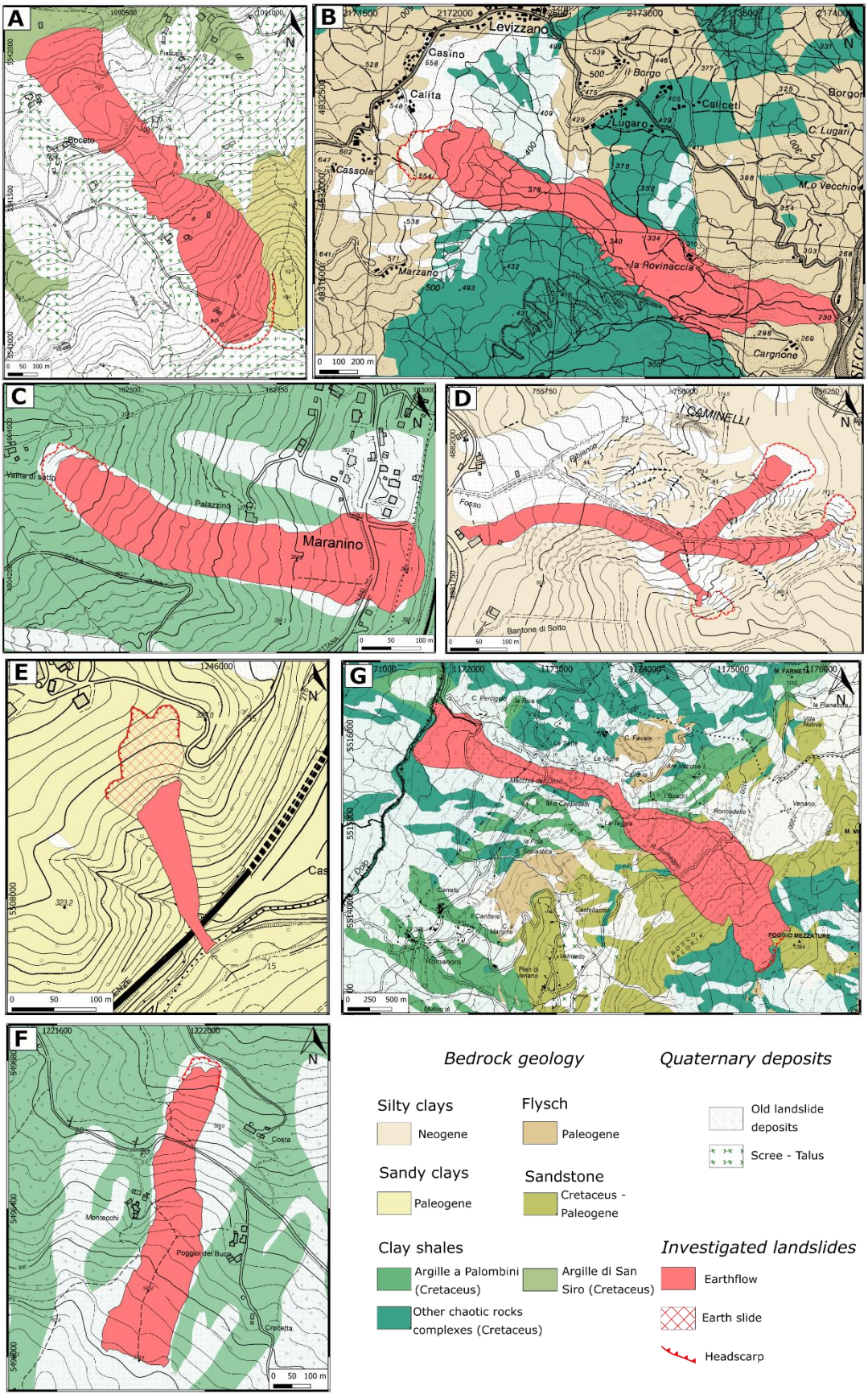

Figure 1.4: Geological maps of the earthflows studied in the current work (more detailed maps are provided in the Papers presented in the following chapters): a) Boceto; b) Ca Lita; c) Marano; d) Montevecchio; e) Puzzola; f) Silla; g) Valoria.

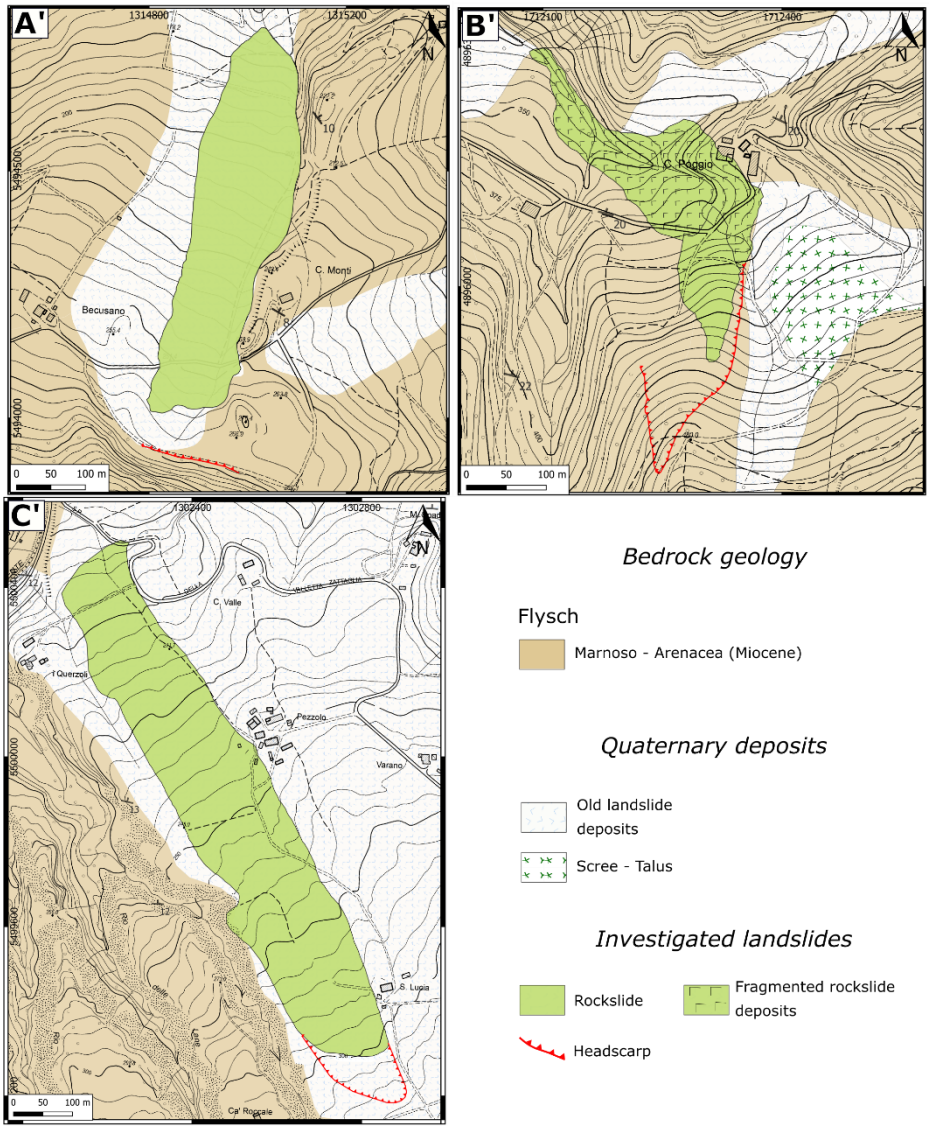

Figure 1.5: Geological maps of the rockslides mentioned in the current work (more detailed maps are provided in the Papers presented in the following chapters): a') Becusano; b') Sintria; c') Zattaglia.

Table 1: Characteristics of the landslides considered in this study. Latitude (Lat) and longitude (Lon) are in WGS84. The type of landslide is defined using the Cruden and Varnes classification (1996). Italic font indicates the cases used only for comparison in Paper 2.

Landslide	Lat. (°)	Lon. (°)	Type	Bedrock	Length (m)	Width (m)	First-time failure	Present work location
Boceto	44.49	9.80	Earthflow	Clay shales	750	160	No	Chap. 4
Ca Lita	44.45	10.63	Earthflow	Clay shales and flysch	2400	180 - 360	No	Chap. 6
Marano	44.22	11.02	Earthflow	Clay shales	700	100	No	Chap. 6
Montevecchio	44.05	12.20	Earthflow	Silty clay	600	40-50	No	Chap. 3 Chap. 4 Chap. 5
Puzzola	44.28	11.20	Earthflow	Sandy clay	300	25	Yes	Chap. 4
Silla	44.20	10.98	Earthflow	Clay shales	1200	250	No	Chap. 4
Valoria	44.32	10.54	Earthflow	Clay shales	3500	100 - 500	No	Chap. 5
Becusano	*44.19*	*11.81*	*Rockslide*	*Mudstone/ sandstone*	*610*	*120*	*Yes*	*Chap. 4*
Sintria	*44.19*	*11.66*	*Rockslide*	*Mudstone/ sandstone*	*450*	*120*	*Yes*	*Chap. 4*
Zattaglia	*44.22*	*11.70*	*Rockslide*	*Mudstone/ sandstone*	*950*	*150*	*No*	*Chap. 4*

General guide through the thesis

The document has been organized into seven chapters. The first Chapter is the current introduction. Chapter 2 provides some notes to the methodological approaches described in the papers. Chapter 3 and Chapter 4 deal with the fluidization process that affects the earthflows of the Emilia-Romagna region. Chapter 5 is a focus on the potential of the Iverson mathematical theory (Iverson, 1985; Iverson, 1986a; Iverson, 1986b) in describing the behavior of such type of earthflows. Chapter 6 is a digression about the relevance of the InSAR technique in giving information about the incoming earthflow reactivations. In Chapter 7 the conclusions are provided.

Three papers are the main themes of this thesis. In Paper 1 (Chapter 3) we presented data about a long monitoring period concerning the Montevecchio earthflow (Forlì-Cesena province). Rayleigh wave velocity data have been gathered in order to understand if that specific earthflow behaves like a real fluid or not. The periodic and continuous measurements show that the material is subjected to significant changes in shear stiffness during rapid surges. Soon after the acceleration, the earthflow soils are very soft and the estimated water content is above the liquid limit.

Paper 2 (Chapter 4) try to address the same problem of Paper 1. The substantial difference relies on the number of landslides that have been investigated. Once again, shear stiffness was measured by the use of Rayleigh wave velocity: periodical surveys were carried out on four active earthflows and three rockslides. Measurements concern periods 2-3 years long. The aim is studying the stiffness trend over time. In the earthflow cases, the stiffness increases in the month following the rapid surging. The same process doesn't result from rockslide's surveys. These data indicate that during the rapid movement both the soils remolding and the water infiltration lead to a decrease of the stiffness, which thus tends to increase in the following period.

Paper 3 (Chapter 6) deals with satellite interferometry. Conventional two-pass interferometry has been applied to two large earthflows that reactivated during the research period (Ca Lita, Reggio Emilia province, and Marano, Bologna province). They are relatively fast earthflows developing in partially vegetated areas. Even during the suspended stages, they move too fast for a correct application of multitemporal analysis as PS-InSAR (Ferretti et al., 2001) or Small Baseline Subset (SBAS, Berardino et al., 2002). Thus, we applied conventional two-pass interferometry to Sentinel 1A/B images: the launch of that mission allows to recover more continuous data partially avoiding decorrelation problems. The results are spatial and temporal patterns of deformation that can be useful information in characterizing the earthflow evolution.

References

Angeli, M. G., Gasparetto, P., Menotti, R. M., Pasuto, A., & Silvano, S. (1996). A visco-plastic model for slope analysis applied to a mudslide in Cortina d'Ampezzo, Italy. *Quarterly Journal of Engineering Geology and Hydrogeology*, *29*(3), 233-240.

Baum, R. L., Savage, W. Z., & Wasowski, J. (2003, May). Mechanics of earthflows. In *Proceedings of the International Conference FLOWS, Sorrento, Italy*.

Bayer, B., Simoni, A., Mulas, M., Corsini, A., & Schmidt, D. (2018). Deformation responses of slow moving landslides to seasonal rainfall in the Northern Apennines, measured by InSAR. *Geomorphology*, *308*, 293-306.

Berardino, P., Fornaro, G., Lanari, R., & Sansosti, E. (2002). A new algorithm for surface deformation monitoring based on small baseline differential SAR interferograms. *IEEE Transactions on geoscience and remote sensing, 40(11)*, 2375-2383.

Berti, M., & Simoni, A. (2012). Observation and analysis of near-surface pore-pressure measurements in clay-shales slopes. *Hydrological Processes*, *26*(14), 2187-2205.

Berti, M., Martina, M. L. V., Franceschini, S., Pignone, S., Simoni, A., & Pizziolo, M. (2012). Probabilistic rainfall thresholds for landslide occurrence using a Bayesian approach. *Journal of Geophysical Research: Earth Surface*, *117*(F4).

Bertolini, G., & Pellegrini, M. (2001). The landslides of the Emilia Apennines (Northern Italy) with reference to those which resumed activity in the 1994–1999 period and required civil protection interventions. *Quad. Geol. Appl*, *8*(1), 27-74.

Bertolini, G., Casagli, N., Ermini, L., & Malaguti, C. (2004). Radiocarbon data on Lateglacial and Holocene landslides in the Northern Apennines. *Natural Hazards*, *31*(3), 645-662.

Colesanti, C., Ferretti, A., Prati, C., & Rocca, F. (2003). Monitoring landslides and tectonic motions with the Permanent Scatterers Technique. *Engineering geology*, *68*(1-2), 3-14.

Corsini, A., Borgatti, L., Caputo, G., De Simone, N., Sartini, G., & Truffelli, G. (2006). Investigation and monitoring in support of the structural mitigation of large slow moving landslides: an example from Ca'Lita (Northern Apennines, Reggio Emilia, Italy).

Ferretti, A., Prati, C., & Rocca, F. (2001). Permanent scatterers in SAR interferometry. *IEEE Transactions on geoscience and remote sensing, 39(1)*, 8-20.

Fleming RW, Baum RL, Giardino M (1999). *Map and description of the active part of the Slumgullion landslide, Hinsdale County, Colorado* (p. 36). US Department of the Interior, US Geological Survey.

Handwerger, A. L., Roering, J. J., Schmidt, D. A., & Rempel, A. W. (2015). Kinematics of earthflows in the Northern California Coast Ranges using satellite interferometry. *Geomorphology*, *246*, 321-333.

Hungr, O., Evans, S. G., & Hutchinson, I. N. (2001). A Review of the Classification of Landslides of the Flow Type. *Environmental & Engineering Geoscience*, *7*(3), 221-238.

Hungr, O., Leroueil, S., & Picarelli, L. (2014). The Varnes classification of landslide types, an update. *Landslides*, *11*(2), 167-194.

Hutchinson, J. H. (1988). General report, morphological and geotechnical parameters of landslides in relation to geology and hydrogeology. In *Landslides, Proceedings of the Fifth International Symposium on Landslides, 1988*.

Notti, D., Meisina, C., Zucca, F., Crosetto, M., & Montserrat, O. (2011). Factors that have an influence on time series. In *Proceedings of FRINGE 2011 Workshop, ESA-ESRIN, Frascati, Italy* (pp. 19-23).

Iverson, R. M., & Major, J. J. (1987). Rainfall, ground-water flow, and seasonal movement at Minor Creek landslide, northwestern California: Physical interpretation of empirical relations. *Geological Society of America Bulletin*, *99*(4), 579-594.

Jongmans, D., Baillet, L., Larose, E., Bottelin, P., Mainsant, G., Chambon, G., & Jaboyedoff, M. (2015). Application of ambient vibration techniques for monitoring the triggering of rapid landslides. In *Engineering Geology for Society and Territory-Volume 2* (pp. 371-374). Springer, Cham.

Keefer, D. K., & Johnson, A. M. (1983). *Earth flows; morphology, mobilization, and movement* (No. 1264). USGPO.

Keefer, D. K. (1984). Landslides caused by earthquakes. *Geological Society of America Bulletin*, *95*(4), 406-421.

Keefer, D. K. (2002). Investigating landslides caused by earthquakes–a historical review. Surveys in geophysics, 23(6), 473-510.

Louie, J. N. (2001). Faster, better: shear-wave velocity to 100 meters depth from refraction microtremor arrays. *Bulletin of the Seismological Society of America*, *91*(2), 347-364.

Mainsant, G., Larose, E., Brönnimann, C., Jongmans, D., Michoud, C., & Jaboyedoff, M. (2012). Ambient seismic noise monitoring of a clay landslide: Toward failure prediction. *Journal of Geophysical Research: Earth Surface*, *117*(F1).

Mainsant, G., Chambon, G., Jongmans, D., Larose, E., & Baillet, L. (2015). Shear-wave-velocity drop prior to clayey mass movement in laboratory flume experiments. *Engineering geology*, *192*, 26-32.

Park, C. B., Miller, R. D., & Xia, J. (1999). Multichannel analysis of surface waves. Geophysics, 64(3), 800-808.

Picarelli, L. (2000). Mechanisms and rates of slope movements in fine grained soils. In *ISRM International Symposium*. International Society for Rock Mechanics and Rock Engineering.

Picarelli, L., Urciuoli, G., Ramondini, M., & Comegna, L. (2005). Main features of mudslides in tectonised highly fissured clay shales. *Landslides*, *2*(1), 15-30.

Santos, J. A., & Correia, A. G. (2000). Shear modulus of soils under cyclic loading at small and medium strain level. In *12th World Conference on Earthquake Engineering* (pp. 1-8).

Schulz, W. H., McKenna, J. P., Kibler, J. D., & Biavati, G. (2009). Relations between hydrology and velocity of a continuously moving landslide—evidence of pore-pressure feedback regulating landslide motion?. *Landslides*, *6*(3), 181-190.

Schulz, W. H., Smith, J. B., Wang, G., Jiang, Y., & Roering, J. J. (2018). Clayey landslide initiation and acceleration strongly modulated by soil swelling. *Geophysical Research Letters*, *45*(4), 1888-1896.

Simoni, A., & Berti, M. (2007, June). Transient hydrological response of weathered clay shales and its implication for slope instability. In *2007) Conference Presentations from 1st North American Landslide Conference, Vail, Colorado. AEG Special Publication* (Vol. 23, pp. 458-471).

Terzaghi, K. R. B. Peck (1948). Soil Mechanics in Engineering Practice.

Tosatti, G., Castaldini, D., Barbieri, M., D'Amato Avanzi, G., Giannecchini, R., Mandrone, G., ... & Tellini, C. (2008). Additional causes of seismically-related landslides in the Northern Apennines, Italy. *Revista de geomorfologie*, *10*, 5-21.

Varnes, D. J. (1958). Landslide types and processes. *Landslides and engineering practice*, *24*, 20-47.

Varnes, D. J. (1978). Slope movement types and processes. *Special report*, *176*, 11-33.

Wasowski, J., & Bovenga, F. (2014). Investigating landslides and unstable slopes with satellite Multi Temporal Interferometry: Current issues and future perspectives. *Engineering Geology*, *174*, 103-138.

2. METHODOLOGICAL NOTES

Investigating earthflow evolution can involve several approaches. In this work we chose to apply seismic techniques for which concerns the field surveys (Paper 1 and 2) and InSAR technique for which concerns the remote sensing surveys (Paper 3).

Seismic surveys

Seismic techniques have been largely applied to study the properties of the soils and shear-wave velocity (V_S) has emerged as a key geophysical parameter for characterizing soil layers in geotechnical engineering (Brown et al., 2000; Konno et al., 2000; Martin and Diehl, 2004). Compared with compressional waves, shear waves offer a wider range of velocity values, allowing to detect changing in lithological and compaction properties of the soils (Dasios et al., 1999). Surface-wave methods can be applied to measure V_S vertical profiles, using the dispersion properties of these waves (e.g. Heisey et al., 1982, Park et al., 1999; Stokoe and Santamarina, 2000). Surface-wave methods are divided into two categories: active methods, which record waves generated by an artificial source (Nazarian et al., 1983; Park et al., 1999), and passive methods, which record waves generated by ambient seismic noise (Liu et al., 2000; Louie, 2001). In recent years, different surface-wave techniques have been applied for landslides investigations (e.g., Jongmans et al., 2009; Renalier et al., 2010; Mainsant et al., 2012).

The seismic data which are treated in this study have been collected applying both active and passive methods. Geophones arrays have been used to obtain Rayleigh wave velocities. Active measurements have been performed using MASW (Park, 1999) technique, while passive ones have been derived by ReMi (Louie, 2001) method. Both techniques allow obtaining velocity-depth profiles of the soils. Details about the seismic techniques are provided in the papers (see Paper 1 and Paper 2). An insight into the survey settings is the aim of this subsection.

Our purpose was gathering data about the soil shear stiffness directly on the field. According to previous studies, stiffness variation in the failure stage are likely, but obtaining a suitable dataset is challenging (Mainsant et al., 2012). Passive seismic methods enabled us to collect a large number of measurements in difficult site conditions. In fact, passive methods do not require any specific seismic source so they can be performed in continuous only by recording seismic noise signals. The main disadvantage of the passive method is that seismic noise is not always detectable and it depends on the geophone amplification system and on the environmental background. For example, if no roads, rivers, or anthropogenic activities exist nearby, the seismic noise can not be detected properly. This is the reason why not all the passive measurements in the Montevecchio

earthflow (see Paper 1) could be considered. Differently from Mainsant and colleagues (2012) who placed only a geophone in each side of the landslide and performed Coda Wave Interferometry (Snieder et al., 2012), we used four geophones set in array across the earthflow deposits and apply ReMi method (Louie, 2001).This arrangement allowed to derive real values of Rayleigh wave velocity and not only the velocity variation as provided by the Coda Wave algorithm. ReMi techniques have been used also for not-continuous surveys. Periodical surveys have been carried out starting from the earlier days after the rapid surges occurring. Rayleigh wave velocity profiles have been measured in several earthflows (see Paper 2) using both passive (ReMi) and active (MASW) techniques. The main purpose was investigating as more cases as possible and extending the measurements both to different portions of the earthflows and outside the deposits. The outside deposits have been tested in order to demonstrate that Rayleigh velocity drops (that means stiffness drops) occur only into the earthflow materials. Repeating that type of survey for a long period was necessary to derive stiffness trends over time. Stiffness trends have been used to interpret the phenomenon in terms of void-ratio and water content variation. The seismic investigations involved also some rockslide activations. The comparison between the stiffness patterns in the earthflow cases and rockslide cases gave further support in earthflow behavior interpretation: since rockslides are certainly not subjected to a fluidization process, no stiffness variation over time should occur.

The number and the period of the investigations had been chosen in relation to the environmental conditions. Emilia-Romagna region is highly vulnerable to landslides and the heavy rainfalls concerning 2014 and 2015 winters lead to the reactivation of several landslide-prone areas (see Paper 2). The period in which the thesis has been developed started only after the landslide reactivation period: most of the seismic data have been only analyzed in the current work, since they have been gathered before. However, the data presented in the papers are related to landslides showing the same characteristics. For instance, they all are earthflows involving clayey lithologies; they have similar morphologies: elongated shapes with a well-defined crown area and a lobo-shaped toe; they reactivated after long rainy period; they show the typical morphology of a flowed mass; they all were very soft after the failure event so that it was very difficult walking on them and installing the proper monitoring devices. After months and years, the flow-like shapes were still well recognizable and there was no cover vegetation on them, but they were definitely stiffer. Comparison with rainfall and displacement data have been carried out only for which concerns continuous seismic surveys: in this case we were able to fully monitor three reactivation events.

InSAR surveys

Spaceborne Synthetic Aperture Radar interferometry (InSAR) is a remote sense technique that can be applied to detect very small ground displacements. Early applications can be found in Gabriel et al. (1989) who measured deformation in an agricultural area, Massonet et al. (1995) who performed satellite InSAR in a volcano area and Massonet and Feigl (1995) who applied the technique to an area deformed by a small earthquake (for a review of the early applications see Massonet and Feigl, 1998). The main advantage of the satellite InSAR concerns the capability of very small displacements detection over a very large area. At the same time, some drawbacks exist: the upper detection limit for displacements measuring requires that no large deformations occur between two consequent radar images and the reflection properties of the ground targets are coherent over time. Those limitations are related to the fact that interferometry measures displacements in order of 2π radians cycle (Massonet and Feigl, 1998; Rosen et al., 2000).

In last year, InSAR on landslide-prone areas have been increasingly applied (e.g. Colesanti et al., 2003; Hilley et al., 2004; Wasowski and Bovenga, 2014; Handwerger et al., 2015; Bayer et al., 2017, 2018). The development of new processing algorithms (Ferretti et al., 2001; Berardino et al., 2002; Hooper et al., 2004; Hooper, 2008; Ferretti, 2011) enhanced the ability to recover data even in difficult contests. However, obtaining valid data on fast-moving landslides is still a hard task. The needing to monitor landslide-prone areas in our region gave an input to try applying conventional two-pass interferometry (standard InSAR in the following) to two large earthflows. Thus, the last part of the thesis focuses on characterizing deformation patterns trough InSAR. We chose to perform standard InSAR on Satellite 1 A/B data. The approach is described in Paper 3, here some notes about the methodology are provided.

The earthflows we investigated are large earthflows involving clayey lithology as the ones studied in the previous papers (Paper 1 and Paper 2). They are subjected to rapid movement (meters per day) during the surges; no vegetation cover presence after years of dormancy suggests that they kept moving slowly during those years. They develop along slope more or less eastward looking, meaning that they move almost in line-of-sight satellite direction. Since interferometric SAR technique measures only one-dimensional changes along the line-of-sight, the selection of these two earthflows allowed to measure most of the real displacement. Finally, these earthflows can be identified into two ascending and two descending tracks, providing very extended datasets.

The investigated periods involve all the available Sentinel dataset before 2019; however, the interferograms referred to the earlier months of the satellite missions have been discarded because of high decorrelation occurring. All the interferograms have been hand-selected and

interpreted in order to retain only those that are sufficiently well-correlated. At the beginning of the process, we produced different types of interferograms depending on the temporal baseline: 24 days, 18 days, 12 days and 6 days. The last type started to be available only from April 2016, when the Sentinel 1B mission was launched. The studied earthflows resulted moving relatively fast even during the dormant stages. For this reason, only 6 days and 12 days interferograms have been finally considered.

We processed Sentinel data: IW (Interferometric Wide) swath-mode SLC (Single Look Complex) products have been downloaded and subjected to numerous computing steps. We used a multi-master method and obtained long interferograms series. The interferograms series have been analyzed with the purpose of getting information about the evolution pattern of the earthflows. Sentinel datasets were preferred to other satellite datasets because they concern data which temporally well distributed: the high-frequency radar acquisitions suit well with relatively fast landslides as those investigated in the Paper 3.

References

Bayer, B., Simoni, A., Schmidt, D., & Bertello, L. (2017). Using advanced InSAR techniques to monitor landslide deformations induced by tunneling in the Northern Apennines, Italy. *Engineering geology*, *226*, 20-32.

Bayer, B., Simoni, A., Mulas, M., Corsini, A., & Schmidt, D. (2018). Deformation responses of slow moving landslides to seasonal rainfall in the Northern Apennines, measured by InSAR. *Geomorphology*, *308*, 293-306.

Berardino, P., Fornaro, G., Lanari, R., & Sansosti, E. (2002). A new algorithm for surface deformation monitoring based on small baseline differential SAR interferograms. *IEEE Transactions on geoscience and remote sensing*, *40*(11), 2375-2383.

Brown, L. T., Diehl, J. G., & Nigbor, R. L. (2000). A simplified procedure to measure average shear-wave velocity to a depth of 30 meters (VS30). In *Proceedings of 12th world conference on earthquake engineering*.

Colesanti, C., Ferretti, A., Prati, C., & Rocca, F. (2003). Monitoring landslides and tectonic motions with the Permanent Scatterers Technique. *Engineering geology*, *68*(1-2), 3-14.

Dasios, A., McCann, C., Astin, T. R., McCann, D. M., & Fenning, P. (1999). Seismic imaging of the shallow subsurface: shear-wave case histories. *Geophysical Prospecting*, *47*(4), 565-591.

Ferretti, A., Prati, C., & Rocca, F. (2001). Permanent scatterers in SAR interferometry. *IEEE Transactions on geoscience and remote sensing*, *39*(1), 8-20.

Ferretti, A., Fumagalli, A., Novali, F., Prati, C., Rocca, F., & Rucci, A. (2011). A new algorithm for processing interferometric data-stacks: SqueeSAR. *IEEE Transactions on Geoscience and Remote Sensing*, *49*(9), 3460-3470.

Gabriel, A. K., Goldstein, R. M., & Zebker, H. A. (1989). Mapping small elevation changes over large areas: differential radar interferometry. *Journal of Geophysical Research: Solid Earth*, *94*(B7), 9183-9191.

Handwerger, A. L., Roering, J. J., Schmidt, D. A., & Rempel, A. W. (2015). Kinematics of earthflows in the Northern California Coast Ranges using satellite interferometry. *Geomorphology*, *246*, 321-333.

Heisey, J. S., Stokoe, K. H., & Meyer, A. H. (1982). Moduli of pavement systems from spectral analysis of surface waves. *Transportation research record*, *852*(22-31), 147.

Hilley, G. E., Bürgmann, R., Ferretti, A., Novali, F., & Rocca, F. (2004). Dynamics of slow-moving landslides from permanent scatterer analysis. *Science*, *304*(5679), 1952-1955.

Hooper, A., Zebker, H., Segall, P., & Kampes, B. (2004). A new method for measuring deformation on volcanoes and other natural terrains using InSAR persistent scatterers. *Geophysical research letters*, *31*(23).

Hooper, A. (2008). A multi-temporal InSAR method incorporating both persistent scatterer and small baseline approaches. *Geophysical Research Letters*, *35*(16).

Jongmans, D., Bièvre, G., Renalier, F., Schwartz, S., Beaurez, N., & Orengo, Y. (2009). Geophysical investigation of a large landslide in glaciolacustrine clays in the Trièves area (French Alps). *Engineering geology*, *109*(1-2), 45-56.

Konno, K., Kataoka, S. I., & Konno, K. (2000). New method for estimating the average s-wave velocity of the ground. In *Proc. of the 6th International Conf. on Seismic Zonation*.

Liu, H. P., Boore, D. M., Joyner, W. B., Oppenheimer, D. H., Warrick, R. E., Zhang, W., ... & Brown, L. T. (2000). Comparison of phase velocities from array measurements of Rayleigh waves associated with microtremor and results calculated from borehole shear-wave velocity profiles. *Bulletin of the Seismological Society of America*, *90*(3), 666-678.

Louie, J. N. (2001). Faster, better: shear-wave velocity to 100 meters depth from refraction microtremor arrays. *Bulletin of the Seismological Society of America*, *91*(2), 347-364.

Mainsant, G., Larose, E., Brönnimann, C., Jongmans, D., Michoud, C., & Jaboyedoff, M. (2012). Ambient seismic noise monitoring of a clay landslide: Toward failure prediction. *Journal of Geophysical Research: Earth Surface*, *117*(F1).

Martin, A. J., & Diehl, J. G. (2004). Practical experience using a simplified procedure to measure average shear-wave velocity to a depth of 30 meters (VS30). In *13th World Conf. on Earthquake Engineering*. Tokyo: International Association for Earthquake Engineering.

Massonnet, D., Briole, P., & Arnaud, A. (1995). Deflation of Mount Etna monitored by spaceborne radar interferometry. *Nature*, *375*(6532), 567.

Massonnet, D., & Feigl, K. L. (1995). Discrimination of geophysical phenomena in satellite radar interferograms. *Geophysical research letters*, *22*(12), 1537-1540.

Massonnet, D., & Feigl, K. L. (1998). Radar interferometry and its application to changes in the Earth's surface. *Reviews of geophysics*, *36*(4), 441-500.

Nazarian, S., & Stokoe, K. H. (1983). *Evaluation of moduli and thicknesses of pavement systems by spectral-analysis-of-surface-waves method* (No. FHWA-TX-83-26+ 256-4 Intrm Rpt.). The Center.

Park, C. B., Miller, R. D., & Xia, J. (1999). Multichannel analysis of surface waves. *Geophysics*, *64*(3), 800-808.

Renalier, F., Bièvre, G., Jongmans, D., Campillo, M., & Bard, P. Y. (2010). Clayey landslide investigations using active and passive Vs measurements. *Advances in near-surface seismology and ground-penetrating radar, Geophys. dev. Ser*, *15*, 397-414.

Rosen, P. A., Hensley, S., Joughin, I. R., Li, F. K., Madsen, S. N., Rodriguez, E., & Goldstein, R. M. (2000). Synthetic aperture radar interferometry. *Proceedings of the IEEE*, *88*(3), 333-382.

Snieder, R., Grêt, A., Douma, H., & Scales, J. (2002). Coda wave interferometry for estimating nonlinear behavior in seismic velocity. *Science*, *295*(5563), 2253-2255.

Stokoe, K. H., & Santamarina, J. C. (2000). Seismic-wave-based testing in geotechnical engineering. In *ISRM International Symposium*. International Society for Rock Mechanics and Rock Engineering.

Wasowski, J., & Bovenga, F. (2014). Investigating landslides and unstable slopes with satellite Multi Temporal Interferometry: Current issues and future perspectives. *Engineering Geology*, *174*, 103-138.

3. PAPER 1

Dynamics of an active earthflow inferred from surface wave monitoring*

Bertello L., Berti M., Castellaro S., Squarzoni G.

*Published in **Journal of Geophysical Research: Earth Surface**

Journal of Geophysical Research: Earth Surface

RESEARCH ARTICLE
10.1029/2017JF004233

Dynamics of an Active Earthflow Inferred From Surface Wave Monitoring

Lara Bertello[1], Matteo Berti[1], Silvia Castellaro[2], and Gabriela Squarzoni[1]

[1]Department of Biological, Geological and Environmental Sciences, University of Bologna, Bologna, Italy, [2]Department of Physics and Astronomy, University of Bologna, Bologna, Italy

Key Points:
- The earthflow material at our study site undergoes significant changes in shear stiffness during rapid movements
- Rayleigh velocity decreases as the earthflow accelerates, then gradually increases through time as the landslide decelerates
- Internal deformation clearly played an important role in the dynamics of the Montevecchio earthflow

Correspondence to:
M. Berti,
matteo.berti@unibo.it

Citation:
Bertello, L., Berti, M., Castellaro, S., & Squarzoni, G. (2018). Dynamics of an active earthflow inferred from surface wave monitoring. *Journal of Geophysical Research: Earth Surface*, *123*. https://doi.org/10.1029/2017JF004233

Received 2 FEB 2017
Accepted 7 JUL 2018
Accepted article online 23 JUL 2018

Abstract Earthflows are clay-rich, slow-moving landslides subjected to periodic accelerations. During the stage of rapid movement, most earthflows exhibit a change in behavior from a solid to a fluid-like state. Although this behavior has been extensively documented in the field, the mechanism leading to the rapid acceleration of earthflows is still poorly understood. Some studies suggest that earthflows essentially behave as Coulomb plastic solids, attributing the flow-like appearance to distributed internal shearing; others believe that these landslides can be treated as viscous fluids, pointing out that the material undergoes a phase transition by increasing its moisture content. Minimal data are currently available to support these different findings. In this study, we present the results of periodic and continuous measurements of Rayleigh wave velocity carried out in an active earthflow located in the northern Apennines of Italy. Our data indicate that the material undergoes significant changes in shear stiffness and undrained strength during rapid movements. In particular, the material exhibits a substantial drop of Rayleigh wave velocity as the earthflow accelerates, followed by a slow return to predisturbance Rayleigh velocities as the landslide decelerates. Soon after a surge, the earthflow material is extremely soft and the estimated gravimetric water content is above the liquid limit. In the following months, the shear stiffness gradually increases and the water content decreases to the plastic limit following a nonlinear trend typical of a consolidation process. These data demonstrate that the earthflow transforms into a viscous fluid by softening of the material and by water entrainment.

1. Introduction

Earthflows are among the most common type of landslides in many mountainous areas (Hungr et al., 2001; Keefer & Johnson, 1983; Picarelli et al., 2005; Simoni et al., 2013). They occur in fine-grained materials and are identified by a tongue or teardrop shape elongated in the downslope direction (Cruden & Varnes, 1996; Hutchinson, 1988). A specific feature of these landslides is their complex style of movement (Bovis & Jones, 1992; Hutchinson, 1970). Earthflows can continue to move slowly at a rate of less than 1 m/year over a long period, primarily by sliding on discrete basal and lateral slip surfaces (Baum et al., 2003; Keefer & Johnson, 1983; Schulz et al., 2009). Then, in response to critical rainfall conditions, they may suddenly accelerate and attain high velocities (up to several meters per hour) for a limited time (Coe et al., 2009; Varnes & Savage, 1996). During the surge of rapid movement, most earthflows create geomorphic features like bulging toes, arcuate ridges, and streamlines that suggest a flow-like behavior (D'Elia et al., 1998; Giordan et al., 2013; Handwerger et al., 2013).

Many researchers believe that the ability of earthflows to surge and rapidly accelerate is a consequence of excess pore water pressures generated along shear surfaces (Baum et al., 2003; Varnes & Savage, 1996; Van Asch & Malet, 2009). Others point out that such a behavior indicates a sudden change in the mechanical properties of the material, like a loss of shear stiffness or an increase of water content (Jongmans et al., 2015; Pastor et al., 2009, 2010; Picarelli et al., 2005). Although these factors are not mutually exclusive (an earthflow could be triggered by an increase of pore water pressures and subsequently undergo a change in mechanical properties as the movement continues) their relative importance is still poorly understood.

Pore water pressure is certainly the most significant factor that can trigger the initial movement, increase the displacement rate, or move earthflows on very gentle slopes (Coe et al., 2009; Hutchinson & Bhandari, 1971; Iverson & Major, 1987). However, clay-rich soils do not liquefy under an increase of pore water pressure (e.g. Seed et al., 2003). In soil mechanics, the term *liquefaction* denotes a condition where a granular material behaves like a fluid because the effective interparticle stress σ' (given by the difference between the total

overburden stress σ and the pore water pressure u; Terzaghi, 1943) reduces essentially to 0 causing the particles to lose contact with each other. Soil liquefaction occurs in loosely packed, cohesionless soils (mostly sand) that tend to decrease in volume when subjected to shear stress (Seed et al., 2003). Clay materials with measurable plasticity are not susceptible to liquefaction because they have undrained cohesion; thus, the shear strength of clays does not become 0 when the effective stress becomes 0 (Robertson, 2010; Seed et al., 2003). Accordingly, most researchers consider earthflows as Coulomb plastic solids that primarily move by sliding and attribute the flow-like appearance to distributed internal shearing rather than mass liquefaction (Baum et al., 2003; Hungr et al., 2001; Keefer & Johnson, 1983).

Nevertheless, fine-grained materials can change from solid to plastic to fluid as the water content increases, showing distinct changes in behavior and consistency. The Atterberg limits are a conventional measure of the critical water contents at which these changes occur (Casagrande, 1932). The transition from a plastic to a fluid state due to an increase of the water content is referred to hereafter as *fluidization*. Fluidization differs from liquefaction because the material undergoes a change in behavior with a change in volume, while liquefaction essentially assumes undrained conditions and constant void ratio. Field observations indicate that earthflows may exhibit a significant increase in water content during mobilization (Hutchinson et al., 1974; Prior et al., 1968). Most active earthflows are so soft that they do not support a person's weight (Keefer & Johnson, 1983) or become "so wet and mascerated that all the debris may truly flow by continuous internal deformation" (Craig, 1979 cited in Moore, 1988, p. 59). Fluid rheologists have extensively investigated the solid-fluid transition of clays in laboratory rheometrical tests, defining the existence of a yield stress that separates a rigid/elastic domain and a fluid domain (Ancey, 2007; Coussot et al., 1998; Mainsant, Larose, et al., 2012). Most of these experiments are conducted on clay slurries at or above the liquid limit (*LL*), which is the moisture content at which soil changes from a plastic to a fluid state measured using the conventional Casagrande apparatus (Casagrande, 1932).

The reasons for this different behavior (shear sliding of a plastic solid vs. viscous flow of a liquid material) are still unclear, but more can be learned by collecting relevant data from rapidly moving earthflows. The monitoring technique recently proposed by Mainsant, Jongmans, et al. (2012) can be useful for this purpose. The method relies on the continuous measurement of Rayleigh wave velocity (V_R) as an indicator of material fluidization (or loss of stiffness). Rayleigh waves are elastic waves which travel near the ground surface with a combination of longitudinal compression and dilation (Richart et al., 1970). These waves are the principal component of ground roll and propagate about 10% slower than shear waves (Telford et al., 1990). The idea behind the method is that, as the shear wave velocity in a fluid tends to 0 (Reynolds, 1997), the Rayleigh wave velocity measured inside a landslide should strongly decrease if the solid material fluidizes (Mainsant, Jongmans, et al., 2012; Mainsant et al., 2015). Mainsant, Jongmans, et al. (2012) monitored an earthflow located in the Swiss Alps and observed that Rayleigh velocities decreased continuously and rapidly for several days before a catastrophic stage of movement, suggesting a dramatic change in the mechanical properties of the material. To our knowledge, this is the only study that has documented the process of solid-to-fluid transition in earthflows. Therefore, more field data need to be collected in different geological and morphological settings in order to understand if rapid surging of earthflows is accompanied by softening and fluidization of the material or mainly occurs by shearing along internal and boundary shear surfaces.

In this study, we used Rayleigh wave velocity to investigate the behavior of the Montevecchio landslide, an active earthflow located in the northern Apennines of Italy (Savio River valley, Province of Cesena). In February 2014, the earthflow entered a period of intense activity that lasted for 17 months until June 2015. During this period, the earthflow experienced three surges of rapid movement characterized by the fluidization of the moving mass. We documented this process by periodic and continuous measurements of Rayleigh wave velocities carried out using the active multichannel analysis of surface waves (MASW) (Park et al., 1999) and the passive refraction microtremors (ReMi) techniques (Louie, 2001). Geophysical data were integrated by continuous measurements of rainfall and landslide displacement. The data reveal a complex relationship between rainfall, displacement rate, and Rayleigh velocity, providing new insight into the dynamics of active earthflows.

2. Study Area

The Montevecchio landslide is located in the northern Apennines of Italy, approximately 16 km to the south of the city of Cesena. The landslide occupies the valley of the Ribianco Creek, a tributary of the Savio River

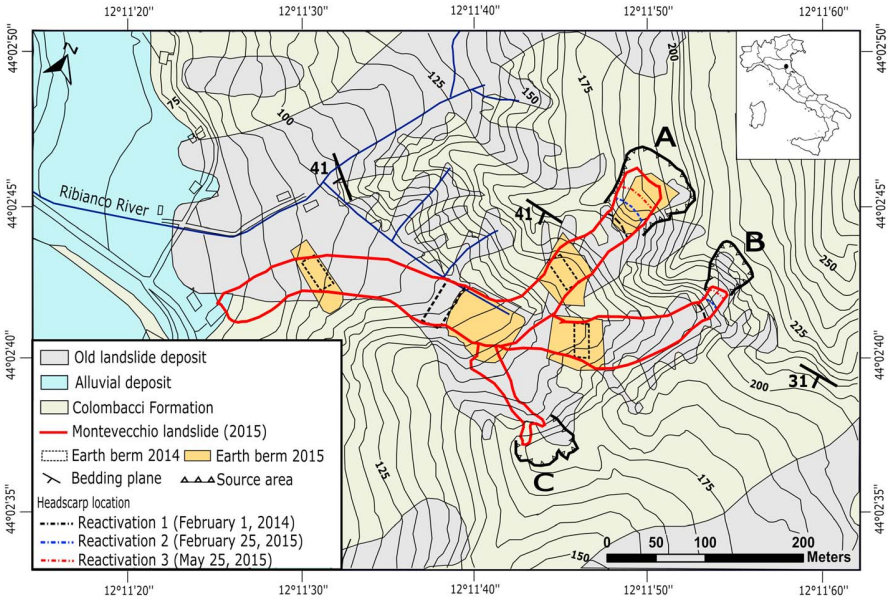

Figure 1. Geological map of the study area. The capital letters (A, B, and C) indicate the source areas of the Montevecchio earthflow. The red line shows the boundary of the landslide in July 2015. The colored dotted lines show the three reactivations and the evolution of the headwall scarp in source areas A and B.

(Figure 1). The area is characterized by relatively gentle slopes (inclination in the range of 7° to 17°) covered by grass and native brush and ranges in elevation from 70 to 215 m above sea level. The upper part of the basin has typical badland morphologies characterized by small gullies, steep slopes (35° to 45°), and low vegetation coverage.

Bedrock geology consists of shallow marine deposits belonging to the Colombacci Formation (Ricci Lucchi et al., 2002). This formation was deposited from the Late Miocene to the Holocene with a maximum thickness of 450 m. In the study area, the Colombacci Formation consists of predominant marly and silty clay interbedded with thin layers of fine sandstone (sandstone/clay ratio is lower than 1/3). The clay is stiff to very stiff with a dark gray-blue color when fresh and becomes soft and brown when weathered. The sandstone layers are loose or only weakly cemented, the color turning from gray to yellow with weathering. The Colombacci Formation is well exposed on the source areas of the earthflow (zone A-B-C; Figure 1).

Old landslide deposits originated by multiple earthflow events occupy about 45% of the Ribianco basin (Figure 1). These deposits consist of a clay-rich colluvium containing scattered blocks of weakly cemented sandstone of variable size. The slopes covered by landslide deposits have an average inclination of about 13°. These landslides are subjected to periodic reactivations. The term reactivation (or remobilization) is current to indicate a phase of high activity after a long period of dormancy (Cruden & Varnes, 1996). Herein, reactivation is used to indicate a stage of rapid movement (with a velocity of several meters per day or per hour) that leads to the complete mobilization of the earthflow material. In the last 50 years, the Montevecchio landslide reactivated once in 1979, when it almost reached the houses and the road at the toe, then in 1997, 1999, 2002, 2005, 2006, and 2008 with local movements in the upper part of the slope. During the last period of activity (February 2014 to June 2015) the earthflow underwent a new complete remobilization (see next section).

Results from geotechnical tests show that the earthflow material is fairly uniform. It has medium plasticity (liquid limit LL = 50%; plastic index = 26%), and it is composed on average of 15% sand, 45% silt, and 40% clay. Blue methylene tests provide a specific surface of the clay of 112 ± 1 m^2/g, which is a typical value for an illite (Hang & Brindley, 1970), and an activity index of the clay fraction (Acb; Lautrin, 1989) equal to 12.5 ± 0.5. The density is 1,850 kg/m^3 in saturated conditions and 1,500 kg/m^3 for the dry soil (average values of 500 g undisturbed samples taken within 1 m of the surface). Direct shear tests give a critical state friction angle ϕ'_{cs}=20° and a residual friction angle ϕ'_r=13°. The local climate is Mediterranean with two main rainy

periods from autumn to early winter (October to December) and during spring (March to May). The average annual precipitation is 780 mm, and the average annual snowfall is about 30 cm. The average annual temperature is 14 °C, and it ranges between 17 and 29 °C during the dry season and between 1 and 20 °C during the wet season.

3. Recent Activity of the Montevecchio Landslide

In February 2014, after a prolonged rainfall of 109 mm in 16 days, the Montevecchio earthflow entered into a new period of activity. The trigger rainfall was above the probabilistic rainfall threshold established for the area (Berti et al., 2012) and caused a large number of landslides in all the Emilia Romagna Region. The activity lasted for 17 months (until June 2015), and within this period the earthflow underwent three major reactivations (first reactivation: 1 February 2014; second reactivation: 25 February 2015; and third reactivation: 25 May 2015). As mentioned above, the term *reactivation* indicates the complete remobilization of the existing landslide deposits from the source area to the toe. Hereafter we also use the term *partial reactivation* to indicate the remobilization of only a portion of the landslide (generally the upper part) and *suspended phase* to indicate the time after a reactivation when the landslide slows down (Schadler, 2010). A reactivation corresponds to a stage of rapid earthflow movement with downslope velocity on the order of meters per hour. This stage generally lasts 2–5 days, then the velocity gradually decreases with time approaching some nonzero value. In fact, during the 17 months of activity, the landslide never stopped and the minimum recorded velocity was on the order of few millimeters per day.

The first reactivation (1 February 2014) started as sliding failure in the source area A (Figure 2a) and caused a retrogression of the head scarp of about 8 m. The landslide quickly propagated downslope (Figure 2b) at a speed of several meters per hour, and in a couple of days reached the toe (Figures 2c and 2d). Local authorities decided to protect the houses and the road by removing the advancing toe material, which was continuously excavated for weeks and deposited on the fluvial terrace to the other side of the road. In March and April 2014, the earthflow partially reactivated several times after heavy rain. The excavations at the toe continued, and four earth berms were built across the landslide to stop the movement (Figure 1). From May 2014, the earthflow entered a suspended phase that lasted about 9 months. During this period, the landslide velocity decreased gradually from meters per day to centimeters per day, with episodes of acceleration of 10–20 cm in a few days after intense rainfall events. The suspend phase ended with the second reactivation of 25 February 2015. This time the initial sliding failures involved both the source areas A and B (Figure 1) causing further retrogression of the head scarps, the complete mobilization of the earthflow, and the destruction of two earth berms. Further movements occurred in March 2015, then the landslide slowed down and almost stopped at the end of April 2015. The third and last reactivation was in 25 May 2015. Again, the landslide remobilized into a fluid, fast-moving earthflow that quickly reached the toe. Here local authorities removed the material 24 hr/day to save the houses. In June 2015, the earthflow almost stopped and significant consolidation works were carried out. Five earth berms were built across the landslide (Figure 1), and a trench drain system was realized to stabilize the middle upper part of the slope. The landslide remained essentially stable in the following years with some localized slides in the source area and along the north flank.

Field observations provide qualitative but valuable information on the reactivation mechanism of the Montevecchio earthflow. In all the three cases, the mobilization starts with a relatively small translational slide in the source area (zones A-B-C; Figure 1) that occur during or shortly after rainstorms. In the source area the bedding planes dip with the same direction as the slope scarp at an angle of 40° with the horizontal, promoting slope instability by translational sliding and flexural buckling. The rock exposed on the scarp is an alternation of marly clay and fine sandstone, with estimated values of the uniaxial compressive strength in the range 1–5 MPa (measured in the field by simple index tests; Hoek & Brown, 1977). Although the rock is fresh or only slightly weathered, it completely disintegrates after rupture and turns into loose, fine-grained debris. The material detached from the scarp accumulates on the head of the gently inclined earthflow deposits causing ground bulging, cracks openings, and the formation of lateral shear surfaces. Hutchinson and Bhandari (1971) first introduced the term undrained loading to describe the failure of a saturated landslide deposit due to undrained compression and consequent rise of pore water pressures.

Figure 2. Photographs of the Montevecchio earthflow in July 2015. (a) Panoramic view of the source area A with the upper part of the earthflow channel; (b) main reach of the earthflow channel; (c, d) deposition area after the second reactivation of February 2015.

After the initial slide, a surge of rapid movement can occur leading to the transformation of the earth slide into an earthflow. Evidence for this change in behavior includes the following: (i) the landslide suddenly accelerates from millimeter to centimeters per day to meters per hour; (ii) a variety of flow structures appear on the ground surface, such as arcuate pressure ridges parallel to the contour lines, hummocks, lateral levees, and tongue-shaped lobes; and (iii) the material softens by increasing the water content. This latter evidence is of particular interest. After each surge we surveyed the landslide and perform several simple tests to assess material softness by inserting a steel tube (5-cm diameter, 2 m long) into the ground. These qualitative data confirm that soon after a reactivation the earthflow is in a fluid state, at least within the upper 2 m. The material shows the consistency of a clay slurry, and we could easily insert the steel tube into the ground by hand throughout its length. Unfortunately, the depth of the fluidized layer remains unknown because the earthflow was not accessible to heavy machinery after a surge.

After the stage of rapid movement, the earthflow decelerates. The velocity at the toe and along the main track gradually decreases from meters per day to centimeters per day, and the landslide continues to move within lateral shears zones with minor internal deformation. Interestingly, the material in the shear bands (20

to 40 cm thick) remain very soft for several weeks after the surge, while the landslide body becomes apparently stiffer and stronger.

4. Field Data

4.1. In Situ Measurements of Rayleigh Wave Velocity

4.1.1. Methodology

We documented the reactivation of the Montevecchio earthflow by means of periodic and continuous measurements of Rayleigh wave velocities, carried out using two standard techniques: the active MASW (Park et al., 1999) and the passive ReMi techniques (Louie, 2001). Both techniques exploit the properties of Rayleigh waves of different wavelengths to excite the material at different depths, thus traveling at different velocity: short wavelengths normally propagate slower (due to the lower velocity of shallow layers), while long wavelengths, which excite deeper layers, propagate faster (Aki & Richards, 1980; Ben-Menahem & Singh, 1981). MASW focuses on the signal produced by artificial sources, while ReMi exploits signals from natural sources.

The velocity of Rayleigh waves of different wavelengths into the ground is derived from the seismic signal recorded at different positions (a minimum of two) over time. Different mathematical algorithms can be used for this derivation. One of the simplest is to filter the signal at different frequencies and cross-correlate the filtered signal among all the geophone couples to find the time lag. Since the distance between each geophone couple is known, the propagation velocity can be obtained by dividing this distance by the time lag. The result of the cross-correlation algorithm (normalized to the autocorrelation function) can be plotted in frequency-velocity plots as shown in the conceptual example of Figure 3.

Since the dispersion of surface waves is a multimodal phenomenon, different velocity values are possible at the same frequency, each one corresponding to a different propagation mode. In the case of an ideal source, ideal receiver geometry, and ideal material (homogeneous and isotropic half-space), the fundamental mode is dominant in terms of energy. However, in real cases this does not always happen. Selecting the dispersion curve of the fundamental mode or correctly sorting the higher modes implies a degree of subjectivity which represents one of the limits of the method as extensively discussed in the literature (Castellaro, 2016; Foti et al., 2014; Gucunski & Woods, 1992; Tokimatsu et al., 1992). Here we restrict the discussion to what can be inferred from Figure 3. The propagation velocity distribution of a surface wave at a specific frequency is given by the normalized cross-correlation function at that frequency. The graduated color bar in Figure 3 represents the probability density distribution (in linear scale from 0 to 1) of the normalized cross-correlation function. The maxima of the distribution (blue dots in Figure 3) are the velocities associated with each frequency. The narrower the peaks (red shaded areas), the better the degree of accuracy of the velocity determination. Point A in Figure 3 indicates the Rayleigh velocity for a frequency of 30 Hz and the associated error bar, defined as the velocity range with a probability value higher than 0.8.

Rayleigh waves induce the maximum displacement in the subsoil at a depth which is approximately $z = \left[\frac{\lambda}{3}, \frac{\lambda}{2}\right]$, where λ is their wavelength and the range depends on the Poisson's ratio (Jones, 1962). This approximate relation provides a way to determine both the velocity profile in the subsoil (remembering that $\lambda = V_R/f$, where the velocity V_R and the frequency f are those of Figure 3) and the maximum investigation depth. Refined inversion algorithms can be used to evaluate the velocity profile in complex multilayered media. Here we refer to the common approximation of converting wavelength to depth by using the relation $z = \lambda/2.5$ (Castellaro, 2016; Foti et al., 2014). From this relation it also follows that the ideal aperture of the array is at least half the desired investigation depth $z_{max}/2$ (Park et al., 2007; Rix & Leipski, 1991), although arrays with $z_{max}/4$ can still be effective under specific circumstances (Castellaro, 2016).

These standard techniques differ from the method used by Mainsant, Jongmans, et al. (2012) in a major aspect. Mainsant, Jongmans, et al. (2012) derived the velocity values in the subsoil from the cross correlation of the signal between two geophones at known distance. The two geophones are planted in the stable ground on both sides of the landslide and provide the average Rayleigh velocity across the investigated section. Since the geophones are located outside the landslide, the system can operate even when the earthflow is rapidly moving. This is an important advantage compared to standard techniques that instead require access to the landslide area. However, the use of two geophones is appropriate only when the

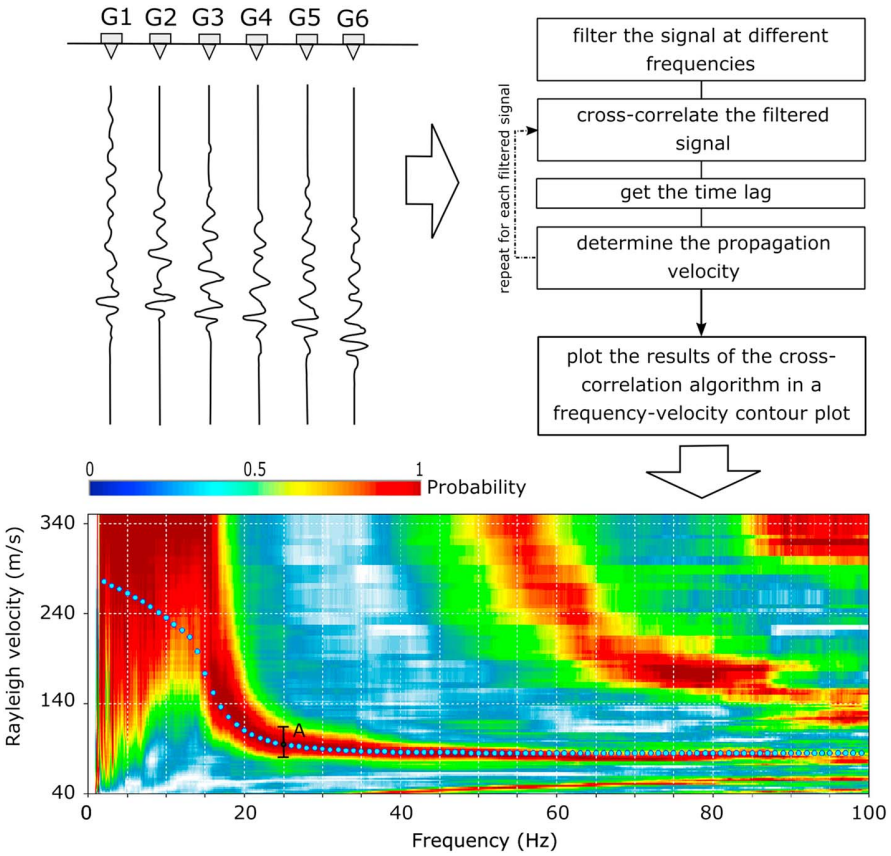

Figure 3. Conceptual example of the multichannel analysis of surface waves/refraction microtremors analysis. (top left) Schematic geophone array (G1–G6). (top right) Flowchart of the solving algorithm. (bottom) Frequency-velocity plot showing the experimental propagation velocity distribution of a surface wave at a specific frequency. The graduated color bar shows the probability density distribution of the normalized cross-correlation function; the blue dots indicate the most probable velocity values for each frequency. The point A indicates the Rayleigh velocity for a frequency of 30 Hz and the associated error bar, defined as the velocity range with a probability value higher than 0.8.

signal propagation is aligned with the geophone line. If this is not the case, the method provides apparent velocity values, larger than the real values by a factor 1/ cos α where α is the angle between the signal propagation direction and the geophone alignment. The method can still provide correct results (that is an apparent velocity distribution centered on the real velocity value) provided that the noise distribution around the geophone line is homogeneous (Mulargia & Castellaro, 2013).

To overcome this limitation, we decided to use standard methods by employing the following: (a) active sources in line with the array, thus ensuring observation of real velocity values; (b) a larger number of geophones, which allows one to compute more precise (statistically redundant) velocity values with depth; and (c) in the case of purely passive surveys, where the source position with respect to the array is unknown, examination of several dispersion curves and retention in the analysis of only those showing the lowest velocity values, which are by definition those closer to the real velocity values (given that $V_{apparent} = V_{real}/\cos\alpha$). Moreover, standard techniques provide measurements of Rayleigh velocity that allow comparing the state of the material in different locations along the landslide.

4.1.2. Periodic Surveys

At Montevecchio, periodic measurements were done every 1–2 months (Table 1) along seven seismic lines. Four lines were located within the landslide area and three just outside the landslide as shown in Figure 4.

We used six vertically polarized 4.5-Hz geophones, pressed firmly into the ground and set at intervals of 2 m each (total length of the seismic lines was 10 m). A 10-m aperture antenna can detect waves as long as 40 m, which corresponds to maximum investigation depth of ~12. The first 5 min of each acquisition was done in

Table 1
Periodic Seismic Surveys Carried Out at Montevecchio (Location of the Measurement Sections in Figure 4)

	Measurement section						
Date	A	B	C	D	E	F	G
2014/05/07	X	X	X	X	X	X	X
2014/06/06	X	X	X	X	X	X	X
2014/06/06	X	X	X	X	X	X	X
2014/07/27	X	X	X	X	X	X	X
2014/08/28		X	X	X			
2015/01/23		X	X	X			
2015/02/18			X				
2015/03/11		X	X	X			
2015/03/24		X	X	X			
2015/04/17		X	X	X			
2015/04/24	X	X	X	X			
2015/04/30			X		X	X	X
2015/05/07	X	X	X	X			
2015/05/19	X	X	X	X	X	X	X
2015/06/08	X	X	X	X			
2015/06/19		X	X	X			
2015/07/09	X	X	X	X			
2015/07/16		X	X				
2015/08/05	X	X	X	X			
2015/08/27			X				
2015/09/04	X	X	X	X			

Note. Dates are formatted as year/month/day.

the passive mode (ReMi), just acquiring the ambient seismic noise, while the last minute was in the active mode (MASW) by putting a seismic source (a jump of the operator) about 5 m apart from the first geophone, in order to ensure as planar as possible wavefronts at the geophones. All the geophones were connected to a Soilspy Rosina acquisition system, and data were processed using the software Grilla (http://moho.world).

The data were analyzed to obtain the fundamental dispersion curves. Besides the problems generally related to the interpretation of dispersion curves (see above), the difficult field conditions provided further sources of uncertainty. During the dry season, the surface of the landslide was pervaded by desiccation cracks and open fractures (Figures 5a and 5b), and a firm coupling of the geophones with the ground was difficult. Conversely, during the rainy season or after the major reactivation events (Figure 5c) the material was fluid and most measuring points were not accessible. Both the variable ground conditions and the different locations of the measuring points affected the accuracy of the results.

Figure 6 shows a typical Rayleigh wave phase velocity versus frequency plot (spectrum) obtained at Montevecchio using active (Figure 6a) and passive (Figure 6b) methods. The dispersion curve can be traced by following the red shaded areas of the frequency-velocity plots. In the active mode (Figure 6a) the dispersion curve is generally well defined over a wide range of frequencies and fundamental mode can easily be identified. In the passive mode (Figure 6b) the curve is discontinuous and the fundamental mode can be recognized only in some frequency intervals. For example, the dispersion curve shown in Figure 6b is not well defined around 10 Hz, from 13 to 17 Hz, and above 25 Hz. In fact, active source methods are generally capable of resolving higher frequencies than passive methods because the source and receiver array can be tailored to the desired frequency range. On the contrary, the source for the ReMi survey was ambient seismic noise that typically contains significant low-frequency energy and lacks high-frequency signal, which can lead to poor resolution of shallow soil layers (Cox & Wood, 2010; Louie, 2001; Strobbia & Cassiani, 2011).

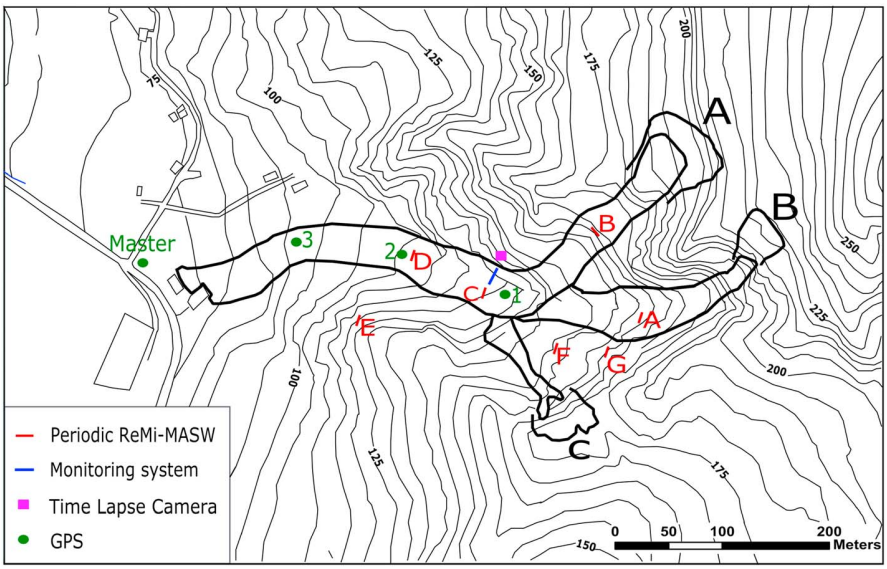

Figure 4. Map showing the location of the monitoring system and periodic seismic surveys. ReMi = refraction microtremors; MASW = multichannel analysis of surface waves; GPS = Global Positioning System.

Figure 5. Photographs showing the difficult ground conditions encountered during periodic seismic surveys. (a, b) Cracks and open fractures characterize the landslide surface during the dry period; (c) water ponds and soft soil reduce the accessibility soon after a reactivation or an intense rainfall.

4.1.3. Continuous Measurements

Periodic surveys were integrated by continuous measurements of surface wave velocity. To this aim, a cost-effective self-produced monitoring system was designed to include these features: (1) easy to install in the field and quick to remove; (2) low maintenance; (3) light enough to be carried by hand; (4) resistant to harsh field conditions (intense rainfall events and large ground displacements); (5) minimal energy consumption; and (6) compatibility with other geotechnical sensors. A number of preliminary tests were conducted to find the optimal configuration. Different combinations of sampling rate (50 to 300 Hz), number

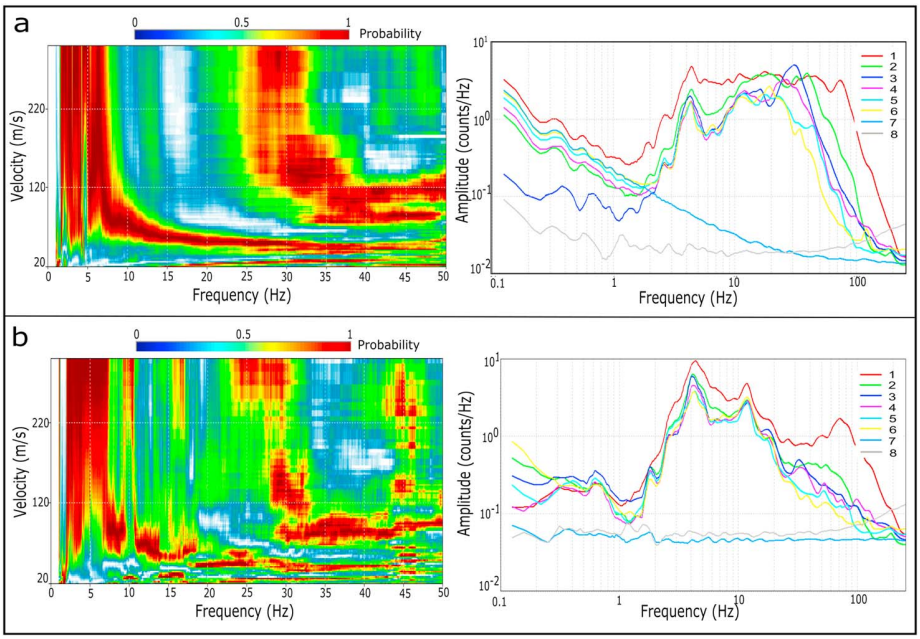

Figure 6. Rayleigh wave phase velocity spectra acquired on 23 January 2015 along section C: (a) active survey; (b) passive survey. Numbers 1 to 8 indicate the geophones.

Figure 7. Photographs of the Montevecchio monitoring system. (a) Geophone amplifiers inserted in a plastic box; (b) continuous monitoring system installed in the main track of the earthflow channel. (c, d) Equipment damaged by a reactivation of the earthflow.

of geophones (two to four) and duration of the acquisition session (from 30 s to 5 min) were tested in order to balance the desired signal accuracy with the capabilities of the datalogger and the power requirement. This appeared to be a suitable configuration for our needs: (i) Campbell CR1000 data logger with CFM100 Compact Flash Module (2 GB); (ii) four vertical geophones at 4.5 Hz with four signal amplifiers (gain = 500); (iii) power supplied by a 12-V 7-Ah battery recharged by a 20-W solar panel. Good results were obtained by reading the four geophones at 300 Hz for 2 min every 1 hr, thus simulating the execution of 24 ReMi surveys every day.

The monitoring system was installed at Montevecchio on 16 May 2014. The geophones were placed on the main track of the earthflow channel with a spacing of 2 m (Figure 4, blue line) and buried at a depth of 20 cm (Figures 7a and 7b) to avoid the atmospheric thermal effect and to ensure an adequate coupling with the ground (Beekman, 2008). In the periodic surveys burial was not required because we hand-tamped around the geophones to ensure good coupling. The signals acquired with this type of approach require to be stable in time, implying a relatively constant background noise over the period of interest (Hadziioannou et al., 2009). Based on direct observation during the first field tests, the main source of ambient seismic noise vibration was the national road located at the toe of the landslide (about 400 m away from the monitoring system) which constitutes a spatially stable background noise. The data collected from the datalogger were periodically downloaded and analyzed using the same software adopted for periodic surveys (Grilla).

Also, in this case, dispersion curves were sometimes difficult to interpret; thus, we decided to classify each curve as *good*, *fair*, or *bad* according to the quality of the phase velocity spectrum (Figure 8). Figure 8a shows a dispersion curve classified as good: Here the fundamental as well as a number of higher modes can clearly be distinguished in a wide frequency interval (5–50 Hz). The case (b) shows a fair dispersion curve in which the fundamental mode can be recognized only at low frequencies (5–10 Hz). Case (c) shows a dispersion curve classified as bad because the fundamental mode cannot be detected. Bad curves are generally due to electrical problems with the signal amplifiers, cable ruptures, or bad ground coupling. For the purpose of the analysis, we only considered the good (a) or fair (b) dispersion curves. As representative velocity values, we picked the central points of the red range (which represents the highest probability range of velocity), while we used the red range boundaries (probability value higher than 0.8) to define the error bars (Figure 3).

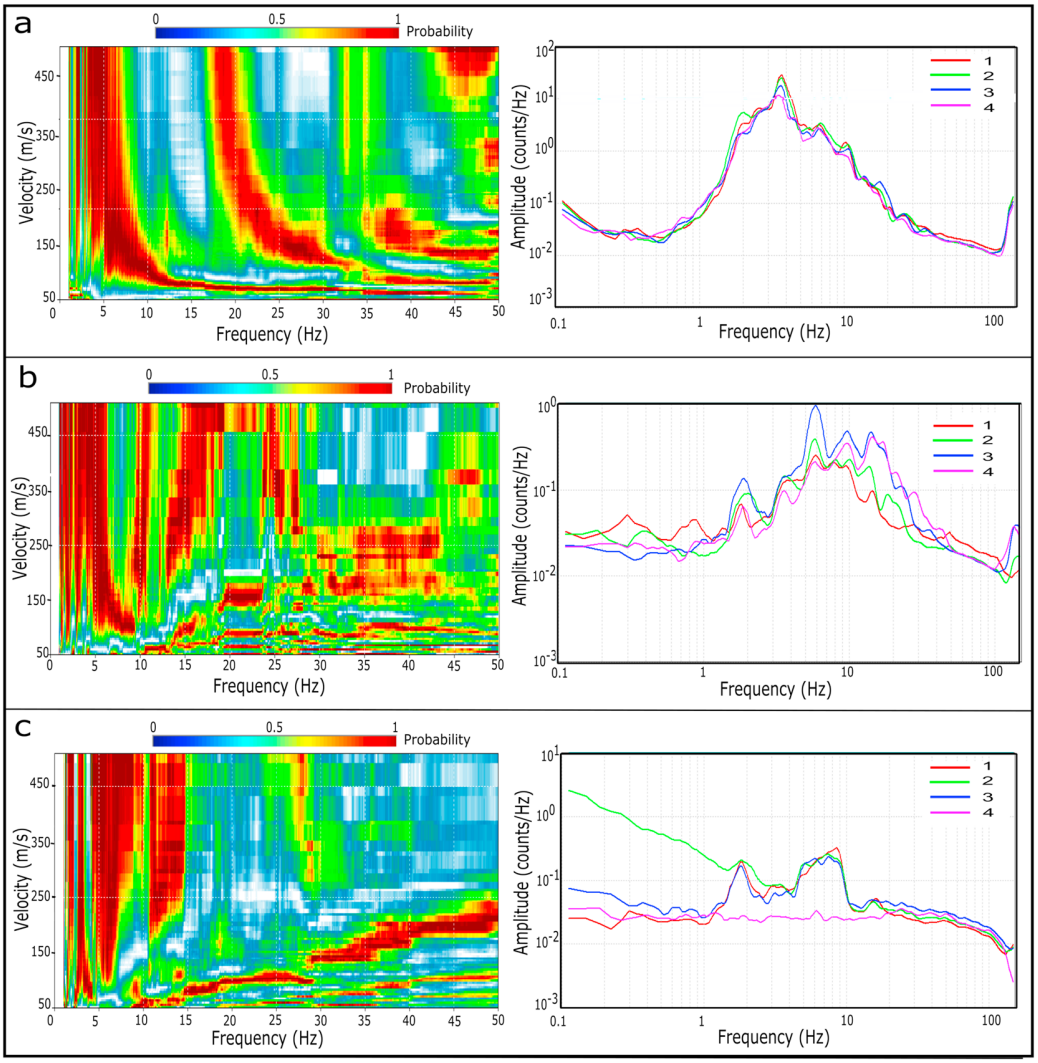

Figure 8. Example of three dispersion curves acquired by the monitoring system. These curves were classified as *good* (a), *fair* (b), and *bad* (c) according to the quality of the phase velocity spectrum (see text). Numbers 1 to 8 indicate the geophones. The graduated color bars show the probability density distribution of the normalized cross-correlation function.

Field monitoring was difficult and sometimes risky due to the strong landslide activity. Figures 7c and 7d show the monitoring system just after the reactivation of 25 February 2015: All the equipment was moved downslope for about 100 m, the rain gage was destroyed, and both the geophones and the amplifiers were lost. The landslide was not accessible for almost 2 months, not even to retrieve the equipment. The system was rebuilt and reinstalled on 7 May 2015. Less than 1 month later, the earthflow reactivated again and the monitoring system was again destroyed. During the monitoring period, we reinstalled the system six times because of the continuous landslide movements.

4.2. Landslide Displacement

Landslide movement was measured using continuous Global Positioning System (GPS) monitoring and a time lapse camera. The GPS system consists of one reference station located in a stable area outside the landslide and three rover stations installed along the earthflow (Figure 4). Rover GPS devices were LEICA-GMX901 antenna (single frequency; 10-Hz update; horizontal accuracy: 3 mm + 0.5 ppm; vertical accuracy: 5 mm + 0.5 ppm) powered by two batteries (12 V 14 Ah in parallel) and recharged by a 60-W solar panel. Rover stations were equipped with Wi-Fi direction antennas (model Ubiquiti Nanostation M5) for

transmitting data to the reference station. The GPS receiver, the control unit, and the Wi-Fi antenna were installed on a 2-m-long pole equipped with a helicoid tip that was screwed into the ground. The reference station was a dual-frequency LEICA GMX902 antenna connected to an industrial PC. The PC ran the software Leica GNSS Spider to process the data in real time. Power to the reference station was provided via a connection to the grid at 220 V. Raw data are processed in real time to determine the GPS coordinates of rovers in differential mode with respect to the reference station, that is, by calculating the baseline, which is the distance between rover and reference GPS antennas. Since the baseline of rover 1 (the one closest to the monitoring station) is nearly coincident with the direction of movement of the landslide, the measured displacements were not projected.

The time-lapse camera is a Brinno TLC200 that was placed outside the right flank of the earthflow (Figure 4) shooting the monitoring system. The camera has a focal length of 36 mm, and it was set to take one picture every 30 min with a resolution of 640 × 480 pixels. An AVI video is created in the camera during recording, which results in a file of about 0.2 MB/frame stored on an 8-GB SD card. The analysis of these videos was carried out with the free software Tracker. The displacement was calculated knowing the dimension of an object in the camera view (a wood pole with red/white markings) and its distance from the camera. The pole was placed in the midline of the channel in order to measure the maximum velocity of the earthflow.

5. Results

5.1. Periodic Acquisitions

Periodic seismic surveys were performed at Montevecchio from May 2014 to September 2015. For the sake of clarity, we divide the data set into the three periods that followed the three main reactivations.

Figure 9 illustrates the data collected after the first reactivation (May 2014 to January 2015). The charts show the profiles of Rayleigh wave velocity (V_r) measured inside (sections A, B, C, and D) and outside (sections E and F) the landslide area in the different campaigns (location in Figure 3). The dates of the seismic surveys are reported as days elapsed since the last mobilization (in this case the partial reactivation of 27 April 2014) in order to highlight the variation of V_r with time. As it can be seen, the Rayleigh wave velocity increased over time inside the landslide, while it remained constant outside. In particular, soon after the reactivation (10 days later) the landslide material was characterized by very low values of $V_r \approx 50$ m/s with no significant differences between the four sections. Then V_r increased. The rate of recovery along the earthflow was however different: In the source area (section A) it was faster than in the lower part (section D), whereas sections B and C showed intermediate values. For instance, in 271 days, the Rayleigh wave velocity at a depth of 5 m increased by 100, 45, 30, and 15 m/s moving from sections A to D.

The data collected after the second reactivation (March to May 2015) provided similar results (Figure 10). The first survey was done only 14 days after the reactivation of 25 February, when the landslide material was still partially fluid. The data show very low velocity profiles throughout the earthflow (see sections B, C, and D; section A is missing because it was not accessible) revealing a sharp drop in V_r compared to initial conditions (end of the period in Figure 9). V_r remained low in the next 2 weeks due to the continuous movements of the earthflow, then gradually increased to the values shown before the mobilization. In this case, the recovery rate was similar in the three sections. The Rayleigh wave velocity outside the landslide remained constant and equal to that measured in the first period ($V_r \approx 200$–250 m/s).

The data of the third period (June to September 2015) show a similar trend (Figure 11). Again, the lowest values of V_r occurred soon after the reactivation of 25 May 2015, then the wave velocity increased to the initial value. During this third period the variation of V_r with time was quite complex (especially in sections B and C) because of the extensive consolidation works carried out from July to September 2015, that triggered partial reactivations of the earthflow around the construction area of the earth berms. The last survey was on 4 September 2015. After that, local authorities installed a dense network of trench drains and drainage channels to stabilize the landslide, and most of the material was reworked up to a depth of 2–4 m.

The chart in Figure 12 summarizes the data collected inside and outside the landslide area over the whole period. For this comparison, we used the Rayleigh wave velocity measured at a depth of 2 m, where the dispersion curves are well defined. Despite the difficulties posed by the harsh field conditions and the uncertainties in these geophysical measurements, a clear trend emerges from the data: The Rayleigh wave velocity

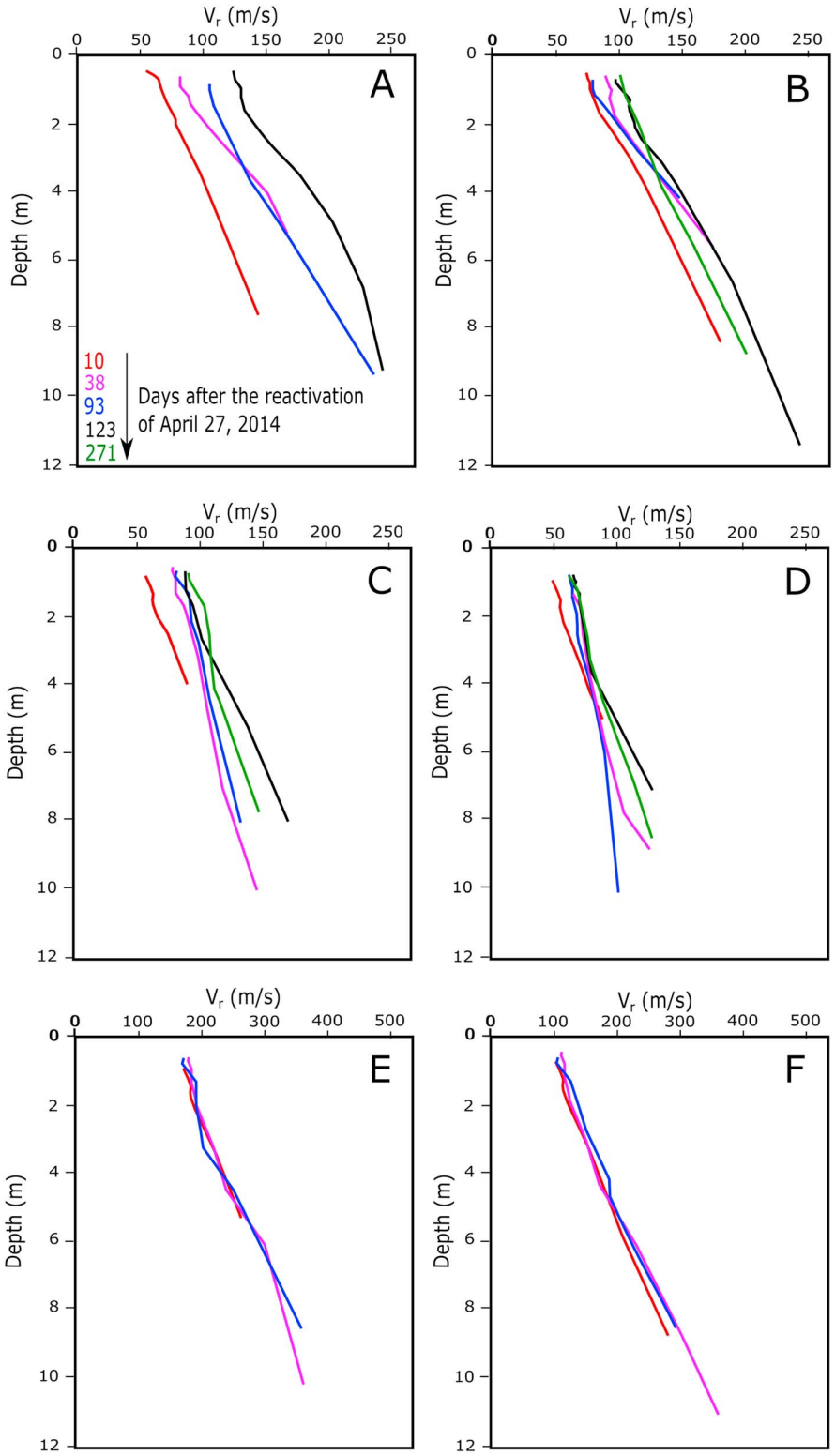

Figure 9. Rayleigh wave velocity profiles measured after the reactivation of 27 April 2014 inside (a–d) and outside (e, f) the landslide. Note the change in scale between (a–d) and (e, f). Locations of each site are shown in Figure 4.

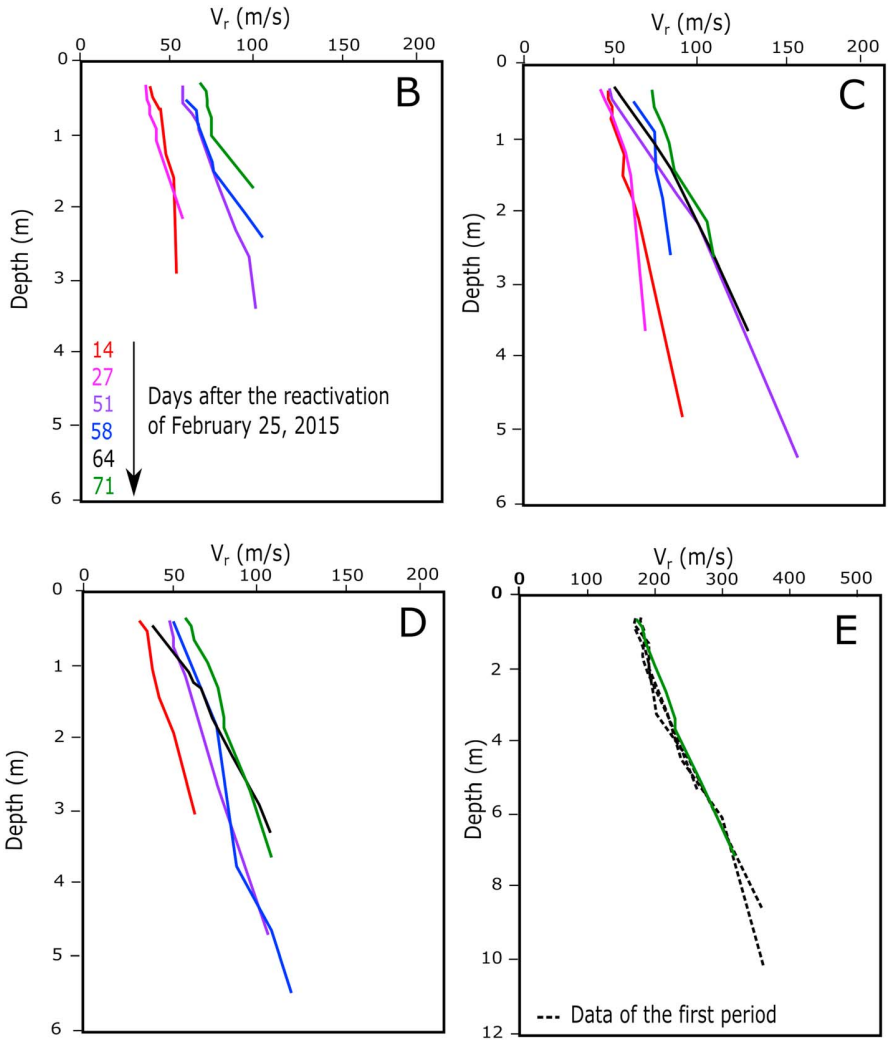

Figure 10. Rayleigh wave velocity profiles measured after the reactivation of 25 February 2015 inside (b–d) and outside (e) the landslide. Note the change in scale for site E. Sites F and G (located outside the landslide) are not shown because the Rayleigh velocity profiles remained constant. Locations of each site are shown in Figure 4.

dropped to very low values as the earthflow reactivated, then it increased to the initial values following a nonlinear trend.

5.2. Continuous Monitoring

Continuous monitoring was designed to capture the change in material properties during the mobilization of the earthflow. The Montevecchio monitoring system was installed in May 2014 (after the first reactivation of 1 February 2014) and recorded the second and third reactivations. The third reactivation of 25 May 2015 is the best documented, both the GPS and the time lapse camera being active. Figure 13 shows the data collected 3 weeks before and after this event. The red and blue dots indicate the Rayleigh wave velocity at a frequency of 11 and 15 Hz, which correspond to an approximate depth of 1 and 2 m, respectively. The gray dots are the velocities at 8 Hz (approximately 3 m). The investigation depth is restricted to the first meters because the dispersion curves obtained by the monitoring system are poorly represented for low frequencies (section 4.1). However, since the velocity profiles obtained by the periodic surveys are almost linear with depth and vary evenly over time (Figure 11), we believe that these data are representative of the general behavior of the landslide.

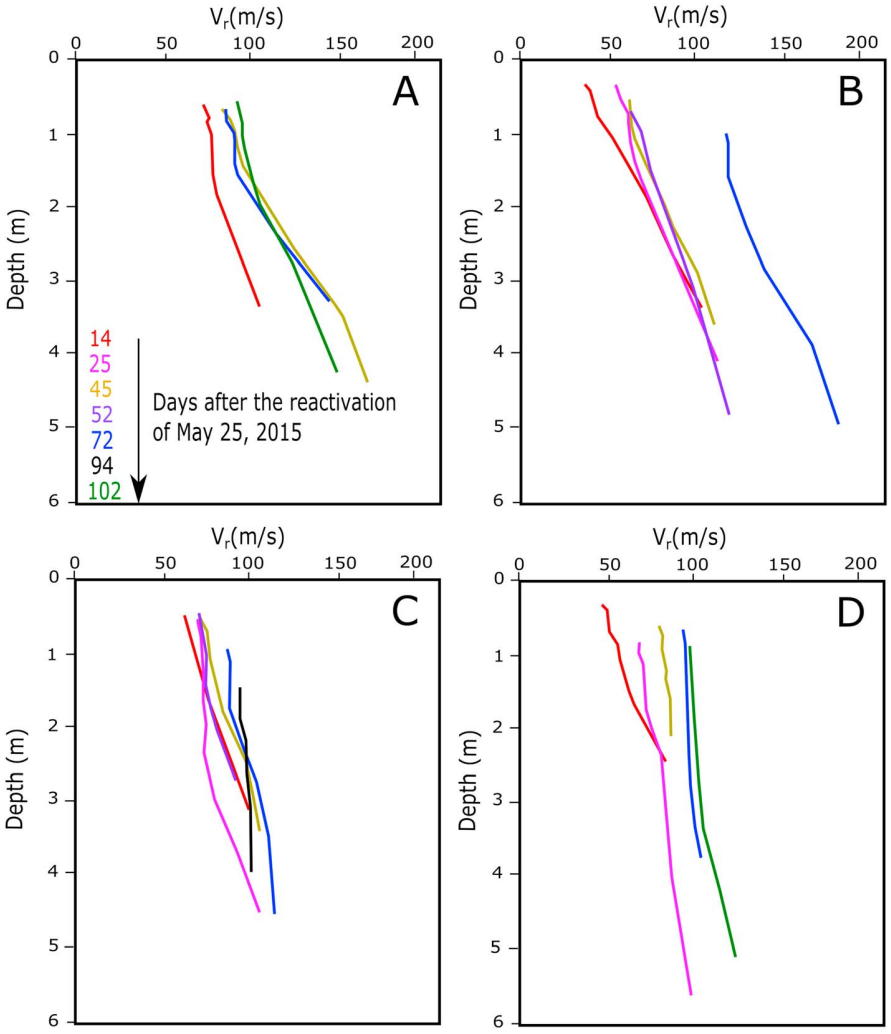

Figure 11. Rayleigh wave velocity profiles measured in the period June 2015 to September 2015 inside the landslide. Sites F and G (located outside the landslide) are not shown because the Rayleigh velocity profiles remained constant. Locations of each site are shown in Figure 4. (a–d) Sites A–D.

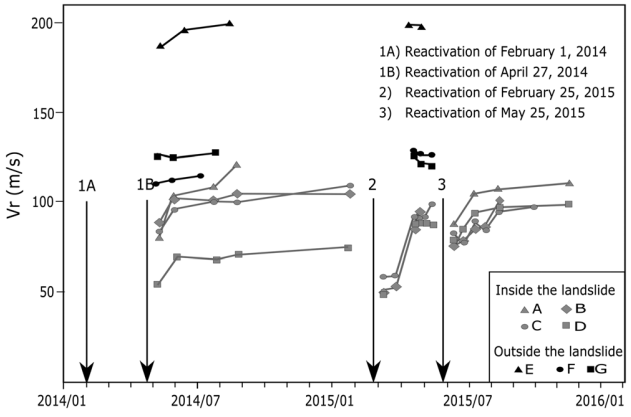

Figure 12. Variation of Rayleigh wave velocity with time during the whole period of measurement. Each point indicates the value measured at a depth of 2 m. Arrows show the start of the main reactivation events of the earthflow.

In the first 3 weeks of May 2015, the landslide was slowly moving at a rate of less than 1 cm/day. Rayleigh velocities were fluctuating around 50–55 m/s, as typically observed during the suspended state of activity of the landslide. On 22 May, it started to rain at 01:10 a.m. and continued until 24 May at 08:40 a.m. with 47 mm in 56 hr. About 11 hr after the beginning of the rain (small inset in Figure 13a) the landslide started to accelerate and the displacement rate increased by 5 times (from 0.8 to 4 cm/day, Figure 13b). The Rayleigh velocity dropped to 30–35 m/s (30% drop) and remained low for the next 2 days, 23 and 24 May, until the first surge of rapid movement (Figure 13c). The first surge started around midnight on 24 May, 16 hr after the end of the rain: The landslide quickly accelerated to 5.8 m/day and reached the peak velocity of 10 m/day (200 times higher than the day before) in the morning of 25 May. In a few hours the earthflow moved downslope of 5–7 m disrupting the geophones array. The landslide then slowed down, and the velocity decreased to 1.2 m/day in the following 10 hr. A second rainfall event of 24 mm in 3 hr occurred on 26 May at 05:30 p.m., leading to the complete reactivation of the

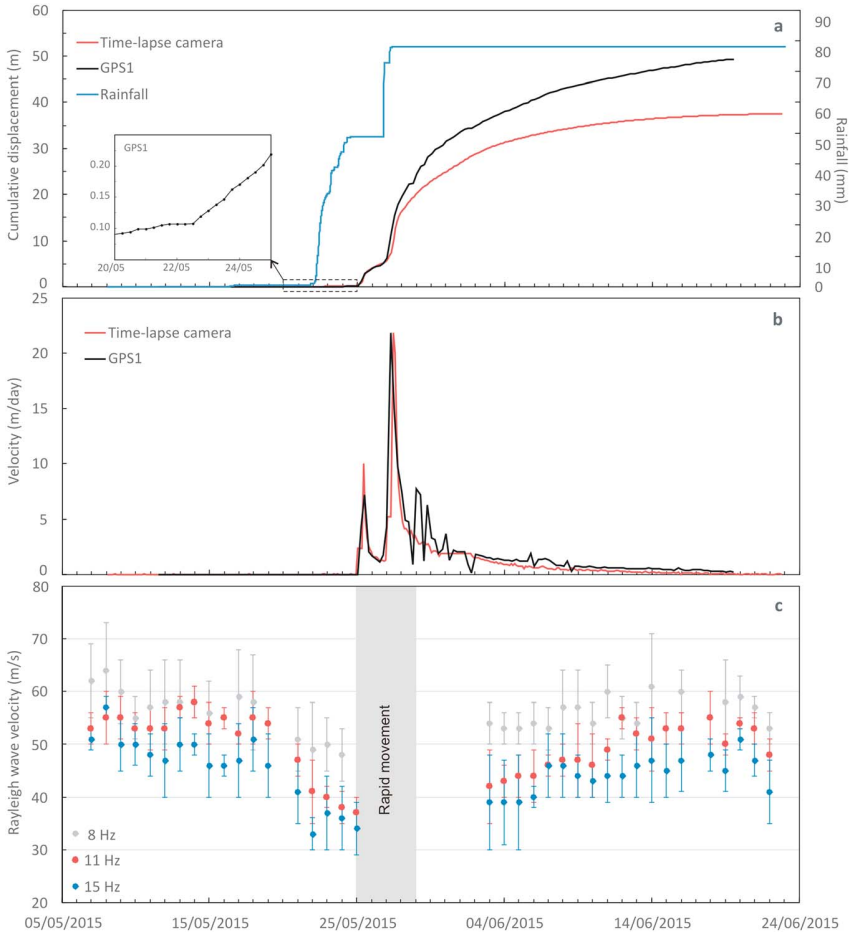

Figure 13. Comparison between (a) rainfall and cumulative displacement, (b) displacement rate, and (c) Rayleigh velocity measured by the monitoring system before and after the reactivation of 25 May 2015.

earthflow. This second surge lasted 3 days with a peak velocity of 22 m/day and a total displacement of about 35 m. The geophones were buried by the landslide, and most of the equipment was destroyed.

The monitoring system was reinstalled on 3 June 2015. The data collected after the surges confirm the results of periodic surveys, showing an increase of Rayleigh velocities as the landslide decelerates. Three weeks after the reactivation, V_r almost returned to the initial values of 50–60 m/s. Rayleigh velocities remained essentially constant until the end of July 2015 (Figure 14). On 26 July, the local authorities started to build an earth dam in the source area A (location in Figure 1) causing a partial reactivation of the landslide. The monitoring system recorded an increase of the displacement rate (from about 5 to 40 cm/day) accompanied by a decrease in V_r of about 20% (Figure 14c). Again, V_r increased to 50–60 m/s as the earthflows decelerates.

Figure 15 shows the data collected during the second reactivation of 25 February 2015. The general trend depicts a progressive increase of the displacement rate (Figures 15a and 15b) accompanied by a decrease of the Rayleigh velocity (Figure 15c). However, a closer look shows some complexity. Rayleigh velocity started to decrease below its normal range on 31 January, while the landslide was slowly moving at a constant speed of about 5 cm/day. Time lapse videos revealed that in those days the ground started to bulge due to the rapid loading of an upload slide. In the next days the Rayleigh velocity remained low (around 45 m/s) and essentially constant, although the displacement rate increased in response to the rainfall event of 3–6 February (160 mm in 4 days). The lowest values of Rayleigh velocity (less than 40 m/s) were recorded anyway just before the complete reactivation of 25 February.

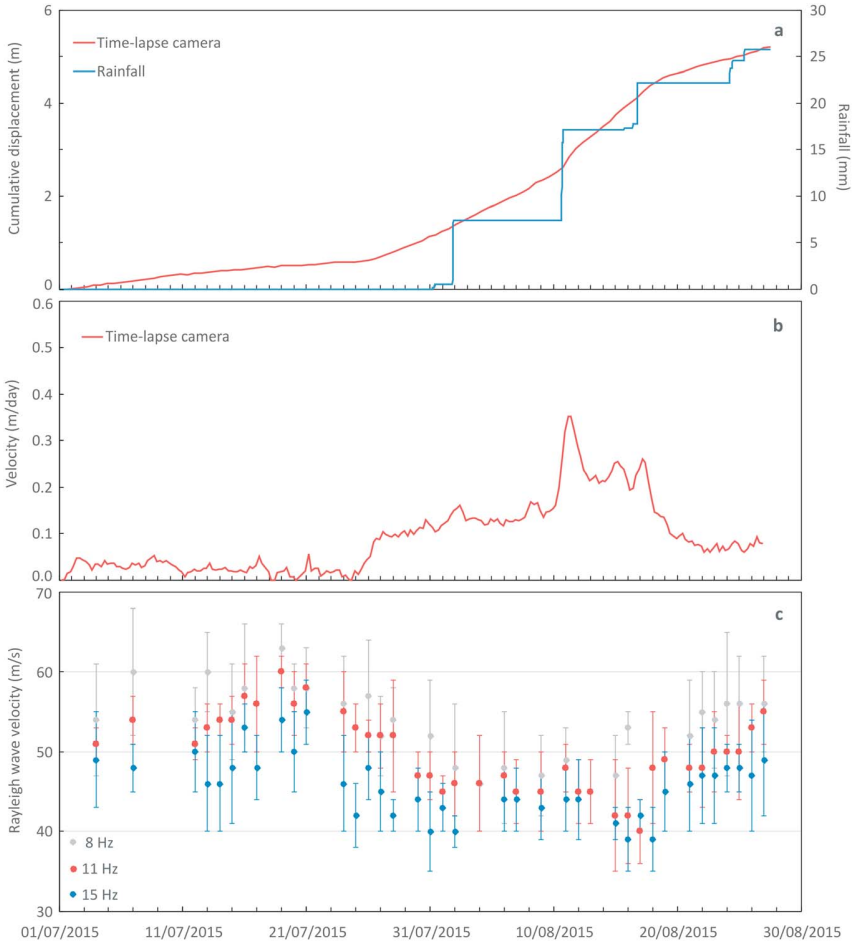

Figure 14. Comparison between (a) rainfall and cumulative displacement, (b) displacement rate, and (c) Rayleigh velocity measured by the monitoring system from June to August 2015.

Figure 16 shows the data recorded 5 months after the first surge, during a long stage of suspended activity (July to November 2014). In that period, the landslide was moving very slowly (Figure 16a) with a trend of slightly decreasing velocity (few millimeters per day, Figure 16b). As expected, the Rayleigh velocities remained essentially constant with small fluctuations around 50 m/s (Figure 16c). The temporary accelerations exhibited by the landslide in response to the rainfall events did not cause any detectable decrease of Rayleigh velocity.

6. Discussion

The data collected at Montevecchio indicate that the mechanical properties of the earthflow material change during surges. The periodic measurements of Rayleigh wave velocity (Figures 9–11) provide the clearest evidence of this variation. Soon after a surge, the values of V_r are very low within the entire thickness of the flowing mass, then they gradually increase through time as the landslide decelerates. The general trend is similar for the three reactivations and across the landslide (Figure 12), although the absolute values of V_r and the rate of recovery are quite different. Possible reasons for these differences are the variable thickness of the landslide, the influence of partial reactivations, the different rate of residual movement, and the effect of consolidation works. For instance, the construction of an earth berm close to section A (Figure 1) is the reason for the rapid increase of V_r observed in that area after the first reactivation (Figure 9a), while the continuous excavations carried out at the toe of the landslide explain the low rate of recovery in section D (Figure 9d).

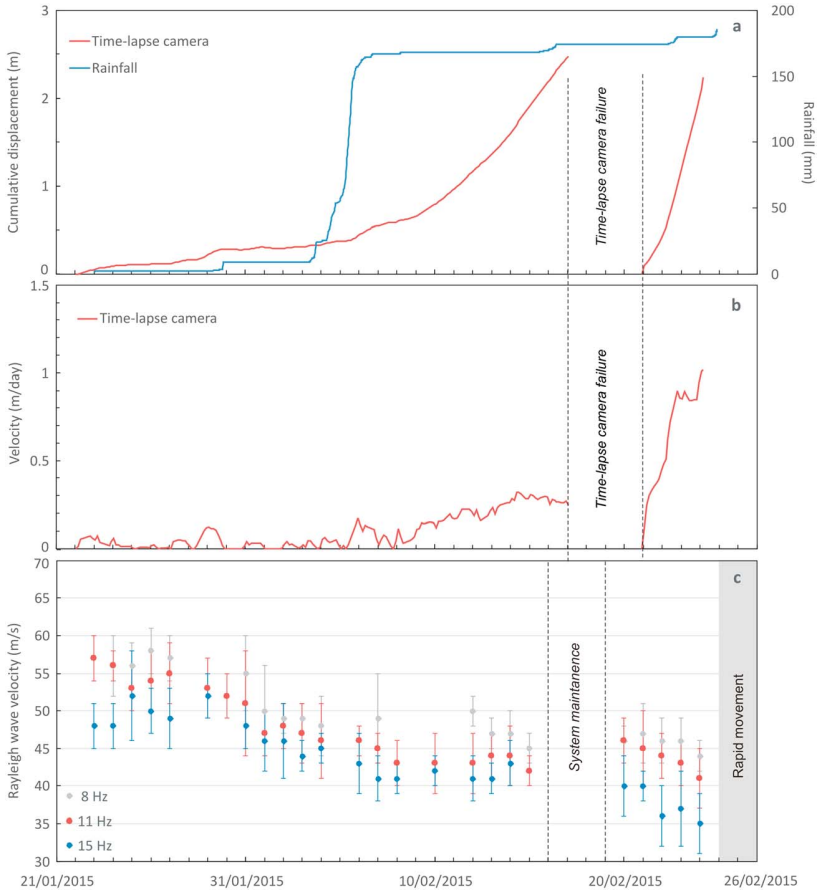

Figure 15. Comparison between (a) rainfall and cumulative displacement, (b) displacement rate, and (c) Rayleigh velocity measured by the monitoring system before the reactivation of 25 February 2015.

Figure 17a provides an overall view of the data collected by periodic surveys. Each point shows the mean Rayleigh velocity measured at a depth of 2 m inside (sections A to D) and outside (sections E and F) the landslide area. Time is reported as number of days elapsed since the last surge. The chart shows that inside the earthflow the Rayleigh velocity increases with time of 30–40% following a power function. A strong increase of V_r occurs in the first 50–70 days after a reactivation, then the velocity seems to attain a constant value (though the curve is not well constrained in the long term). Outside the landslide area, V_r is constant and remarkably higher. These data can be interpreted according to the general theory of surface wave propagation. Rayleigh waves travel with a horizontal wave speed V_r slightly lower than the shear wave speed V_s. The ratio V_r/V_s is a function of the material's Poisson ratio ν (Achenbach, 2012):

$$\frac{V_r}{V_s} = \frac{0.862 + 1.14\nu}{1 + \nu} \tag{1}$$

varying from 0.90 for ν = 0.5 (soft soils in undrained conditions) to 0.95 for ν = 0.2 (stiff soils in drained conditions). In an elastic solid, the velocity of a shear wave is controlled by the solid's density (ρ) and shear modulus (G_0):

$$V_s = \sqrt{\frac{G_0}{\rho}} \tag{2}$$

where the notation G_0 indicates the initial shear modulus at very small strains (0.001% or less). Since the density ρ has a negligible effect on V_s compared to G_0, the observed variation of Rayleigh velocity at

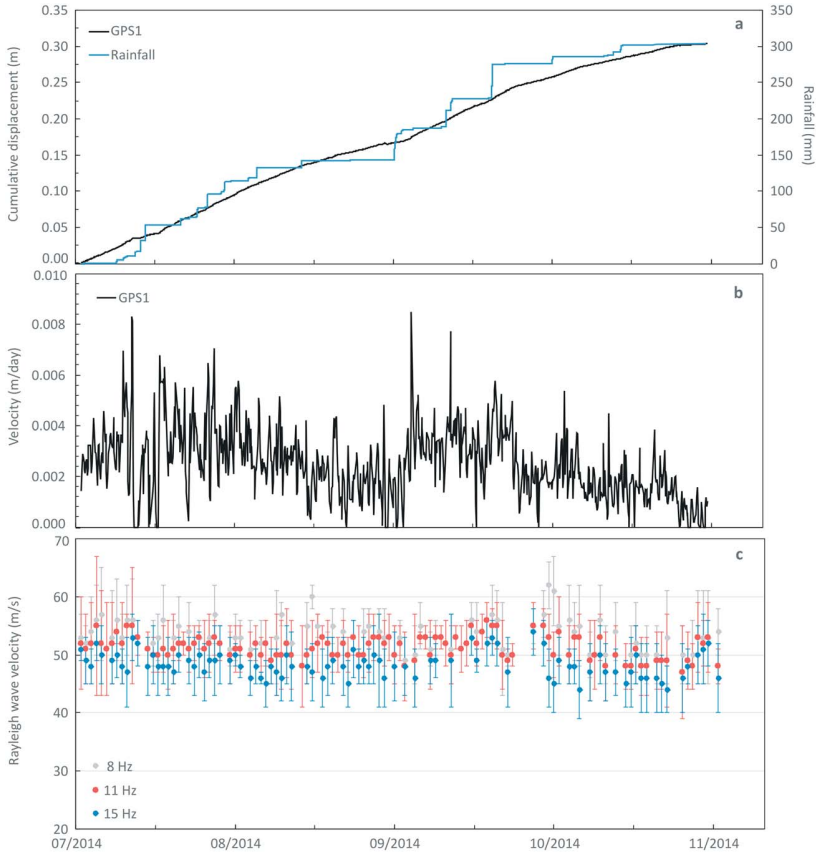

Figure 16. Comparison between (a) rainfall and cumulative displacement, (b) displacement rate, and (c) Rayleigh velocity measured by the monitoring system during the suspended phase from July to November 2014.

Montevecchio can be interpreted as a change in the shear stiffness of the earthflow material. Figure 17b shows the values of G_0 computed from the shear velocity assuming $\nu = 0.5$ and constant soil density $\rho = 1,600$ kg/m^3 (taken as the average between the density at the liquid limit $\rho \approx 1,400$ kg/m^3 and the average density measured in the field $\rho \approx 1,800$ kg/m^3). As can be seen, the shear modulus of the earthflow material is very low soon after mobilization ($G_0 \approx 5$ MPa) then increases up to 15–20 MPa in a few months. This change in shear stiffness suggests a transition from a very soft to a stiff clay (Ortiz & Simo, 1986).

Similar results are obtained using undrained shear strength (s_u). A number of V_s-based correlations have been proposed in the literature to estimate s_u. Mayne (2007) derived a generalized relation between shear wave velocity and cone tip resistance (q_t in kilopascals) suitable for clay materials from soft to firm:

$$V_s = 1.75 q_t^{0.627} \tag{3}$$

Nguyen et al. (2014) found a correlation between G_0 and net cone tip resistance ($q_t - \sigma_{v0}$, where σ_{v0} is the total vertical stress) better constrained for soft clays:

$$G_0 = 89.1 (q_t - \sigma_{v0})^{1.50} \tag{4}$$

These relationships can be inverted to obtain q_t and combined with the classical formula $s_u = (q_t - \sigma_{v0})/N_{kt}$ (where $N_{kt} \approx 14$ is a bearing factor; Robertson, 2009) to get an estimate of undrained strength. The results obtained with the two formulas (using V_s from 64 to 109 m/s in equation (3), and G_0 from 7 to 19 MPa in equation (4)) are similar: The undrained strength is as low as 10–20 kPa soon after reactivation and increases up to 30–50 kPa in a few months. Two cone penetration tests carried out at the toe of the earthflow 3 weeks after the first reactivation confirm these estimates: in the first 8 m, the tests show a uniform profile of s_u with

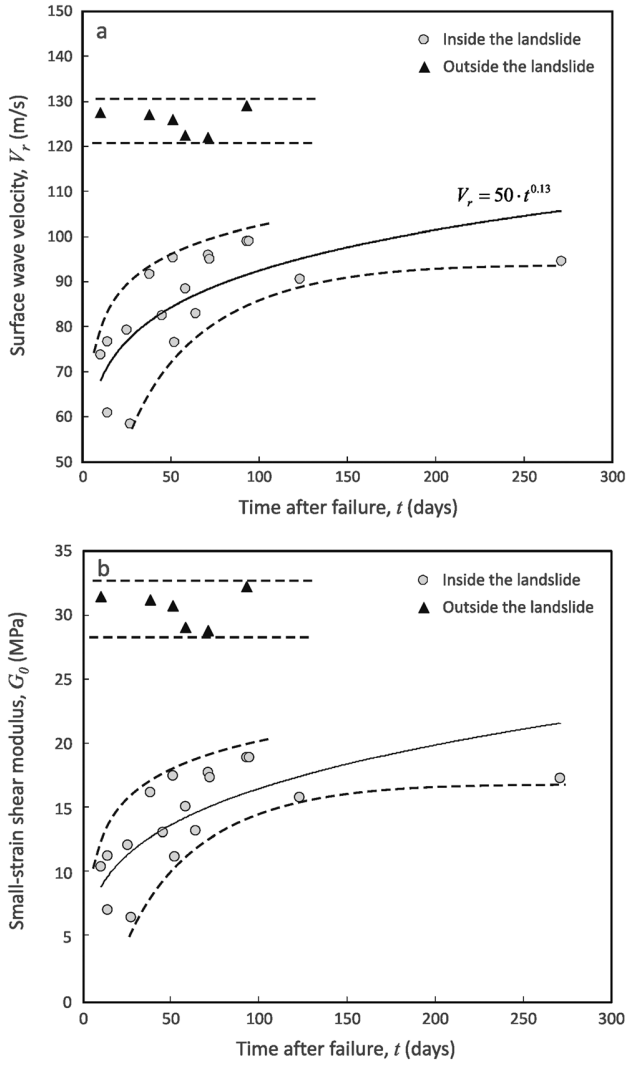

Figure 17. Charts showing the variation of Rayleigh velocity at a depth of 2 m (a) and the corresponding variation of small-strain shear stiffness (b) with the time elapsed after a surge. Each point represents the mean value of V_r or G_0 obtained by periodic surveys inside (gray dots) or outside (black triangles) the landslide area.

depth with average values in the range 15–20 kPa. According to the British Standard 5930 (BSI, 2015), this change in strength indicates the transition from a very soft to a firm clay.

The data collected by the monitoring system provide evidence of changes in the material properties before a surge. Rayleigh velocity decreases about 20–30 m/s (about 30% of the initial value) just before the rapid movements of February and May 2015 (Figures 13–15), indicating that the material softened as the earthflow approached a new reactivation. The observed drop is about 10 times larger than the standard deviation of measurements computed when the landslide is not moving (2.2 m/s obtained as the average of the standard deviations calculated for the three frequencies in Figure 16). However, the relationship between displacement rate and Rayleigh velocity is not simple. In particular, there is no correlation between landslide speed and V_r drop (apparently, V_r decreases a similar amount regardless of the velocity attained by the landslide) and also the timing of the drop may differ (section 5.2). Unfortunately, available data do not allow one to establish why there are these differences, mostly because of the limited accuracy of the measurements. A series of tests conducted in the field showed that the dispersion curve obtained without an active seismic source and using only four geophones instead of the six used in periodic surveys is often discontinuous or poorly defined. This makes it difficult to detect the Rayleigh velocity of the fundamental mode and introduces significant uncertainties in the data.

Despite these uncertainties, the data seem to provide a consistent picture: The earthflow material softens during a surge and then recovers to the initial state when the velocity decreases and the landslide comes to rest. The observed behavior cannot be explained by a simple sliding mechanism in which the landslide moves as a plastic solid. The drop in shear stiffness clearly plays an important role in the rapid movement of the Montevecchio earthflow.

What is now more difficult to establish is whether the measured variation of V_r may indicate a solid-to-fluid transition of the earthflow. In principle, we could infer the void ratio e of the material from the shear stiffness G_0 and compute the gravimetric water content at saturation w ($w = e/G_s$, where $G_s \approx 2.7$ is the specific gravity of solids) in order to evaluate the state of the earthflow. However, going from Rayleigh velocities to void ratio is fraught with uncertainties, mostly because the various forms of the $G_0 - e$ functions published in the literature might not apply to our field conditions. In particular, the measured change of Rayleigh velocity at Montevecchio could be due to the opening (or closing) of fissures and cracks within the earthflow rather than dilation (or contraction) of the soil skeleton. The following analysis therefore provides only a rough estimate of e and should be taken with care.

Santos and Correia (2000) compared a number of empirical $e - G_0$ relationships and proposed the following function for soils with high percentages of fines:

$$G_0 = 4,000\, e^{-1.3} p^{0.5} \tag{5}$$

where p is the mean effective stress. Inverting the equation and assuming $p \approx \sigma'_{v0} = 12$ kPa (effective vertical stress at a depth of 2 m considering ρ = 1, 600 kg/m^3 and water table at the ground surface), we can estimate e from G_0. According to equation (5) the observed increase of shear stiffness after a surge (G_0 from 5 to 20 MPa) corresponds to a decrease of void ratio from $e \approx 2$ to $e \approx 0.7$. The equivalent change in terms of gravimetric water content is from $w \approx 80\%$ to $w \approx 30\%$. By comparing these values with the Atterberg limits

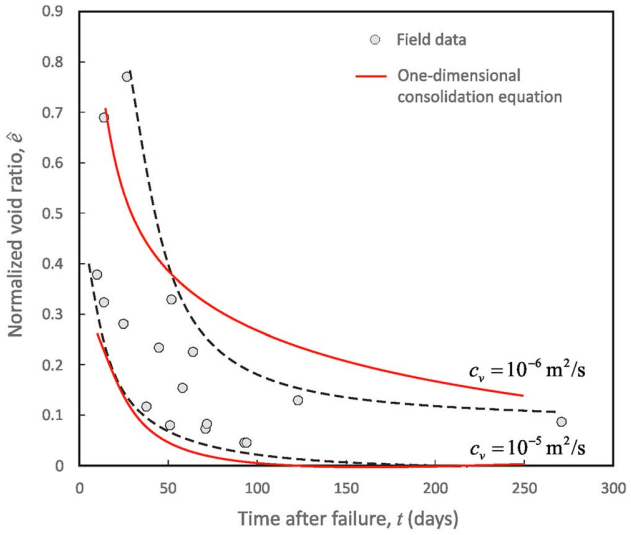

Figure 18. Variation of the normalized void ratio (see text) with the time elapsed after a surge. Each point represents the mean value of void ratio obtained by periodic surveys inside the landslide area. Red lines indicate the theoretical trend predicted by the one-dimensional Terzaghi equation for two values of the coefficient of consolidation c_v typical of fine-grained materials.

(plastic limit PL = 26%; liquid limit LL = 50%), it turns out that the water content of the earthflow material is well above the liquid limit soon after a surge and close to the plastic limit a few months later. These results are consistent with the field evidence of a fluidized surface of the earthflow that becomes stiffer with time (section 3).

The change of void ratio with time is of particular interest because it allows a quantitative analysis of observed behavior. Figure 18 shows this trend using a normalized void ratio index ($\hat{e}$) that depicts the relative variation of e with respect to the minimum and maximum values estimated above (e_{min} = 0.7 and e_{max} = 2):

$$\hat{e} = \frac{e_{max} - e}{e_{max} - e_{min}} \tag{6}$$

The trend of the experimental points is consistent with the exponential decrease of pore volume (and increase of material stiffness) that occurs with time during the consolidation of a porous material. In fact, it agrees well with the theoretical trend (red curves in Figure 18) predicted by the one-dimensional consolidation theory (Terzaghi, 1943). Terzaghi's consolidation theory allows one to compute the change in void ratio of the soil skeleton to the change in effective stress by means of a coefficient of consolidation (c_v) determined in the oedometer test. The theoretical curves in Figure 18 are computed using typical values of c_v for fine-grained material (Holtz & Kovacs, 1981). These simple calculations suggest that the Montevecchio earthflow is in a fluid state soon after a rapid stage of movement and returns to a plastic state as the material consolidates.

A further point of discussion is the possible use of this technique for early warning of earthflow movement. Mainsant, Jongmans, et al. (2012) detected a decrease of the relative Rayleigh wave velocity well before the reactivation of their monitored landslide (a first 2% drop about 1 month before the movement, and a second 7% drop 4 days before). Mainsant et al. (2015) carried out some laboratory experiments on artificial clay slopes having different water content and confirmed a drop in V_r values before the failure. Based on these, the authors suggested that field monitoring of surface wave velocity could be potentially used to predict landslides (Mainsant, Jongmans, et al., 2012). These results are more uncertain. Also, in our case the Rayleigh velocities start to drop a few days before a surge (Figures 13 and 15), but the relationship between V_r and landslide speed is not straightforward. Besides the uncertainty in the data (as discussed above), a possible explanation is that we started to monitor the landslide after a major reactivation (February 2014) that completely remobilized the existing deposits, generating a dense network of pervasive cracks and fissures within the landslide mass. The two surges of February and May 2015 were subsequent reactivations of a completely remolded material. In these conditions, the effect of prefailure cracking and deformations is probably negligible, and we could only detect the main changes in shear stiffness associated with the very rapid movements. Therefore, our data cannot prove (or disprove) the use of Rayleigh wave monitoring for early landslide detection.

Finally, we comment on the technique adopted at Montevecchio for the continuous monitoring of Rayleigh wave velocity. The system configuration (four vertical geophones at 4.5 Hz; 2-min sessions at 300 Hz every 1 hr; passive mode) proved its effectiveness but with a low accuracy compared to periodic surveys. Several modifications can be done to improve results: (1) Combine active and passive mode acquisition in order to improve the dispersion curve at high-frequency ranges (for example, using an automatic hammer controlled by the datalogger that hits the ground during the measurement session); (2) use more geophones to ensure an adequate data redundancy (Tokimatsu, 1997). As an alternative to surface wave monitoring, one could use a down-hole probe specifically designed for long-term monitoring in order to get direct measurements of shear wave velocity inside an active landslide. A further improvement is to combine geophysical data with geotechnical sensors to monitor the water content of the material. Conventional dieletric sensors have an accuracy of 2–3% (Starr & Paltineanu, 2002) and should easily detect the dramatic change of water content required for the earthflow to transition to a liquid state.

7. Conclusions

Rayleigh wave monitoring proved to be an effective method to investigate changes in material properties that occur in active earthflows. In this study, we monitored rainfall, ground displacement, and Rayleigh wave velocity of an earthflow located in the northern Apennines of Italy during a two-year period of intense activity. Based on these data, several conclusions can be drawn:

1. As the earthflow accelerates approaching a stage of rapid movement, the material exhibits a significant drop of Rayleigh wave velocity (V_r); V_r then gradually increases through time as the landslide decelerates, returning to the initial values in a few months.
2. The observed variation of Rayleigh velocity indicates that the earthflow material undergoes a significant change in shear stiffness and undrained strength during each reactivation.
3. A simple mechanism of rigid-block sliding cannot account for the observed changes of material properties; therefore, internal disturbance and remolding play an important role in the dynamics of the Montevecchio earthflow.
4. Tentative estimates of the gravimetric water content suggest that the earthflow material is well above the liquid limit soon after a surge and decreases with time to the plastic limit following a nonlinear trend typical of a consolidation process; these estimates are consistent with the field evidence of a fluidized surface of the earthflow that becomes stiffer with time.
5. At Montevecchio, there is no clear evidence that Rayleigh velocity starts to decrease well before the landslide starts to move, as found by Mainsant et al. (2015). However, in our case the material was completely remolded by previous movements; thus, we probably missed the initial cracking that occurs when the landslide reactivates after a long period of dormancy.
6. Because of the difficult field conditions and limited accuracy of the data, available measurements do not allow the precise identification of the relationship between rainfall, displacement rate, and Rayleigh velocity. In order to get better results from field monitoring, we suggest the use of six to eight geophones (instead of four), the use of an active seismic source controlled by the data logger, and installation of soil moisture sensors at different depths for direct measurement of water content inside the landslide.

Acknowledgments
This work was supported by the Civil Protection Agency of the Emilia-Romagna Region under the framework agreement "Special activities on support to the forecast and emergency planning of Civil Protection with respect to hydrogeological risk" (ASPER-RER, 2011–2015 and 2016–2021). The authors would also like to acknowledge the Editor, the Associate Editor, and the anonymous reviewers of JGR, who provided constructive comments and suggestions which improved the quality of the paper. All the data used in this paper are listed in the references or are included in the figures and tables.

References

Achenbach, J. D. (2012). *Wave propagation in elastic solids*. Amsterdam, The Netherlands: Elsevier.
Aki, K., & Richards, P. G. (1980). *Quantitative seismology, theory and methods*. San Francisco: W. H. Freeman & Co. https://doi.org/10.1017/S0016756800034439
Ancey, C. (2007). Plasticity and geophysical flows: A review. *Journal of Non-Newtonian Fluid Mechanics*, *142*(1-3), 4–35. https://doi.org/10.1016/j.jnnfm.2006.05.005
Baum, R. L., Savage, W. Z., & Wasowski, J. (2003). Mechanics of earth flows. Paper presented at International Workshop on Occurrence and Mechanisms of Flows in Natural Slopes and Earthfills, Sorrento, Italy.
Beekman, A. N. (2008). A comparison of experimental ReMi measurements with various source, array, and site condition, (Master's thesis). University of Arkansas.
Ben-Menahem, A., & Singh, S. J. (1981). *Seismic waves and sources*. New York: Springer-Verlag. https://doi.org/10.1007/978-1-4612-5856-8
Berti, M., Martina, M. L. V., Franceschini, S., Pignone, S., Simoni, A., & Pizziolo, M. (2012). Probabilistic rainfall thresholds for landslide occurrence using a Bayesian approach. *Journal of Geophysical Research*, *117*, F04006. https://doi.org/10.1029/2012JF002367
Bovis, M. J., & Jones, P. (1992). Holocene history of earth flow mass movement in south central British Columbia: The influence of hydroclimatic changes. *Canadian Journal of Earth Sciences*, *29*(8), 1746–1755. https://doi.org/10.1139/e92-137
BSI (2015). *BS 5930: 2015—The code of practice for site investigations*. Milton Keynes: British Standards Institute.
Casagrande, A. (1932). Research on the Atterberg limits of soils. *Public Roads*, *13*(8), 121–136.
Castellaro, S. (2016). Soil and structure damping from single station measurements. *Soil Dynamics and Earthquake Engineering*, *90*, 480–493. https://doi.org/10.1016/j.soildyn.2016.08.005
Coe, J. A., McKenna, J. P., Godt, J. W., & Baum, R. L. (2009). Basal-topographic control of stationary ponds on a continuously moving landslide. *Earth Surface Processes and Landforms*, *34*(2), 264–279. https://doi.org/10.1002/esp.1721
Coussot, P., Laigle, D., Arattano, M., Deganutti, A., & Marchi, L. (1998). Direct determination of rheological characteristics of debris flow. *Journal of Hydraulic Engineering*, *124*(8), 865–868. https://doi.org/10.1061/(ASCE)0733-9429(1998)124:8(865)
Cox, B. R., & Wood, C. M. (2010). A comparison of linear array surface wave methods at soft soil site in the Mississippi embayment. Paper presented at GeoFlorida 2010, Orlando, Florida.
Craig, D. (1979). Some apsects of mudslide stability in East County Antrim, Northern Ireland, (Doctoral thesis). Queen's University of Belfast, Ireland.
Cruden, D. M., & Varnes, D. J. (1996). Landslide types and processes. In A. K. Turner, & R. L. Shuster (Eds.), *Landslides: Investigation and mitigation*, (Vol. 247, pp. 36–75). Washington: National Academy Press.
D'Elia, B., Picarelli, L., & Leroueil, S. (1998). Geotechnical characterization of slope movements in structurally complex clay soils and stiff jointed clays. *Rivista Italiana di Geotecnica*, *33*, 5–32.
Foti, S., Lai, G. C., Rix, G. J., & Strobbia, C. (2014). *Surface wave methods for near-surface site characterization*. London: CRC Press. https://doi.org/10.1201/b17268
Giordan, D., Allasia, P., Manconi, A., Baldo, M., Santangelo, M., Cardinali, M., et al. (2013). Morphological and kinematic evolution of a large earthflow: The Montaguto landslide, southern Italy. *Geomorphology*, *187*, 61–79. https://doi.org/10.1016/j.geomorph.2012.12.035

Gucunski, N., & Woods, R. D. (1992). Numerical simulation of the SASW test. *Soil Dynamics and Earthquake Engineering*, *11*(4), 213–227. https://doi.org/10.1016/0267-7261(92)90036-D

Hadziioannou, C., Larose, E., Coutant, O., Roux, P., & Campillo, M. (2009). Stability of monitoring weak changes in multiply scattering media with ambient noise correlation: Laboratory experiments. *The Journal of the Acoustical Society of America*, *125*(6), 3688–3695. https://doi.org/10.1121/1.3125345

Handwerger, A. L., Roering, J. J., & Schmidt, D. A. (2013). Controls on the seasonal deformation of slow-moving landslides. *Earth and Planetary Science Letters*, 377–378.

Hang, P. T., & Brindley, G. W. (1970). Methylene blue absorption by clays minerals. Determination of surface areas and cation exchange capacities (clay organic studies XVIII). *Clays and Clay Minerals*, *18*(4), 203–212. https://doi.org/10.1346/CCMN.1970.0180404

Hoek, E., & Brown, E. T. (1977). Practical estimates of rock mass strength. *International Journal of Rock Mechanics and Mining Sciences*, *34*(8), 1165–1186.

Holtz, R. D., & Kovacs, W. D. (1981). *An introduction to geotechnical engineering*, *Civil Engineering and Engineering Mechanics Series*, (). New Jersey: Prentice-Hall.

Hungr, O., Evans, S. G., Bovis, M. J., & Hutchinson, J. N. (2001). A review of the classification of landslides the flow type. *Environmental and Engineering Geoscience*, *7*(3), 221–238. https://doi.org/10.2113/gseegeosci.7.3.221

Hutchinson, J. N. (1970). A coastal mudflow on the London clay cliffs at Beltinge, North Kent. *Geotechnique*, *20*(4), 412–438. https://doi.org/10.1680/geot.1970.20.4.412

Hutchinson, J. N. (1988). General report: Morphological and geotechnial parameters of landslides in relation to geology and hydrogeology. Paper presented at Fifth International Symposium on Landslides, Rotterdam, Netherlands.

Hutchinson, J. N., & Bhandari, R. K. (1971). Undrained loading, a fundamental mechanism of mudflows and other mass movements. *Geotechnique*, *21*(4), 353–358. https://doi.org/10.1680/geot.1971.21.4.353

Hutchinson, J. N., Prior, D. B., & Stephens, N. (1974). Potentially dangerous surges in an Antrim [Ireland] mudslide. *Quarterly Journal of Engineering Geology*, *7*(4), 363–376.

Iverson, R. M., & Major, J. J. (1987). Groundwater seepage vectors and potential for hillslope failure and debris flow mobilization. *Water Resources Research*, *22*(11), 1543–1548. https://doi.org/10.1029/WR022i011p01543

Jones, R. (1962). Surface wave technique for measuring the elastic properties and thickness of roads: Theoretical development. *British Journal of Applied Physics*, *13*(1), 21–29. https://doi.org/10.1088/0508-3443/13/1/306

Jongmans, D., Baillet, L., Larose, E., Bottelin, P., Mainsant, G., Chambon, G., & Jaboyedoff M. (2015). Application of ambient vibration techniques for monitoring the triggering of rapid landslides. Paper presented at Engineering Geology for Society and Territory,Torino, Italy.

Keefer, D. K., & Johnson, A. M. (1983). Earthflows: Morphology, mobilization and movement. U.S. Geological Survey Professional Paper (1264), U.S. Government Printing Office.

Lautrin, D. (1989). Utilisation pratique des parametres derives de l'essai au blue de methylene dans le les projets de genie civile. *Bulletin de Liaison des Laboratories des Ponts et Chaussees*, *160*, 29–41.

Louie, J. N. (2001). Faster, better: Shear-wave velocity to 100 meters depth from refraction microtremor arrays. *Bulletin of Seismological Society of America*, *91*(2), 347–364. https://doi.org/10.1785/0120000098

Mainsant, G., Chambon, G., Jongmans, D., Larose, E., & Baillet, L. (2015). Shear-wave-velocity drop prior to clayey mass movement in laboratory flume experiment. *Engineering Geology*, *192*, 26–32. https://doi.org/10.1016/j.enggeo.2015.03.019

Mainsant, G., Jongmans, D., Chambon, G., Larose, E., & Baillet, L. (2012). Shear-wave velocity as an indicator for rheological changes in clay materials: Lessons from laboratory experiments. *Geophysical Research Letters*, *39*, L19301. https://doi.org/10.1029/2012GL053159

Mainsant, G., Larose, E., Bronnima, C., Jongmans, D., Michoud, C., & Jaboyedoff, M. (2012). Ambient seismic noise monitoring of a clay landslide: Toward failure prediction. *Geophisical Research Letters*, *117*, F01030. https://doi.org/10.1029/2011JF002159

Mayne, P. (2007). *Cone penetration testing, a synthesis of highway practice*. Trasportation Research Board: Washington, DC.

Moore, R. (1988). The clay mineralogy, weathering and mudslide behaviour on coastal cliffs, (Doctoral thesis). King's College, University of London.

Mulargia, F., & Castellaro, S. (2013). A seismic passive imaging step beyond SPAC and ReMiTM. *Geophysics*, *78*, 63–72.

Nguyen, H. Q., DeGroot, D. J., & Lunne, T. (2014). Small strain shear modulus of marine clays from CPT. Paper presented at 3rd International Symposium on Cone Penetration Testing, Las Vegas, Nevada, USA.

Ortiz, M., & Simo, J. S. (1986). An analysis of a new class of integration algorithms for elastoplastic constitutive relation. *International Journal for Numerical Methods in Fluids*, *23*(3), 353–366.

Park, C., Miller, R., & Xia, J. (1999). Multi-channel analysis of surface waves. *Geophysics*, *64*(3), 800–808. https://doi.org/10.1190/1.1444590

Park, C. B., Miller, R. D., Xia, J., & Ivanov, J. (2007). Multichannel analysis of surface waves (MASW)—Active and passive methods. *The Leading Edge*, *26*(1), 60–64. https://doi.org/10.1190/1.2431832

Pastor, M., Blanc, T., & Pastor, M. J. (2009). A depth integrated viscoplastic model for dilatant saturated cohesive-frictional fluidized mixtures: Application to fast catastrophic landslides. *Journal of Non-Newtonian Fluid Mechanics*, *158*(1–3), 142–153. https://doi.org/10.1016/j.jnnfm.2008.07.014

Pastor, M., Manzanal, D., Fernandez Merodo, J. A., Mira, P., Blanc, T., Drempetic, V., et al. (2010). From solids to fluidized soils: Diffuse failure mechanisms in geostructures with applications to fast catastrophic landslides. *Granular Matter*, *12*(3), 211–228. https://doi.org/10.1007/s10035-009-0152-4

Picarelli, L., Urcioli, L., Ramondini, G., & Comegna, L. (2005). Main features of mudslides in tectonised highly fissured clays shales. *Landslides*, *2*(1), 15–30. https://doi.org/10.1007/s10346-004-0040-2

Prior, D. B., Stephens, N., & Archer, D. R. (1968). Composite mudflows on the Antrim coast of north East Ireland. *Geografiska Annaler*, *50*(2), 65–78. https://doi.org/10.1080/04353676.1968.11879773

Reynolds, J. M. (1997). *An introduction to applied and environmental geophysics*. Chichester: John Wiley.

Ricci Lucchi, F., Bassetti, M. A., Manzi, V., & Roveri, M. (2002). Il Messiniano trent'anni dopo: Eventi connessi alla crisi di salinità dell'avanfossa appenninica. *Studi Geologici Camerti*, *1*, 127–142.

Richart, F. E., Hall, J. R., & Woods, R. D. (1970). *Vibrations of soils and foundations*. Englewood Cliffs, NJ: Prentice-Hall, Inc.

Rix, G. J., & Leipski, E. A. (1991). Accuracy and resolution of surface wave inversion. In S. K. Bhatia, & G. W. Blaney (Eds.), *Recent advances in instrumentation, data acquisition and testing in soil dynamics* (pp. 17–32). San Diego, CA: American Society of Civil Engineers.

Robertson, P. K. (2009). Evaluation of flow liquefaction and liquefied strength using the cone penetration test. *Journal of Geotechnical and Geoenvironmental Engineering*, *136*(6), 842–853.

Robertson, P. K. (2010). Estimating in situ state parameter and friction angle in sandy soils from CPT. Paper presented at 2nd Internation Symposium of Cone Penetration Test, Signal Hill, California, USA.

Santos, J. A., & Correia, G. (2000). Shear modulus of soils under cyclic loading at small and medium strain level. Paper presented at 12WCEE 2000, Auckland, New Zeland.
Schadler, W. (2010). *Slope movements of the earthflow type - engineering -geological investigation, geotechnical assessment, and modelling of the source areas on the basis of case studies from the Alps and Apennines*. Berlin: Logos verlag Berling GmbH.
Schulz, W. H., Mackenna, J. P., Kibler, J. D., & Biavati, G. (2009). Relations between hydrology and velocity of a continuously moving landslide —Evidence of pore pressure feedback regulating landslide motion? *Landslides*, *6*(3), 181–190. https://doi.org/10.1007/s10346-009-0157-4
Seed, R. B., Cetin, K. O., Moss, R. E. S., Kammerer, A. M., Wu, J., Pestana, J. M., et al. (2003). Recent advances in soil liquefaction engineering: A unified and consistent framework. Eartquake Engineerig Research Center, Report No. EERC 2003-6, California, USA.
Simoni, A., Ponza, A., Picotti, V., Berti, M., & Dinelli, E. (2013). Earthflow sediment production and Holocene sediment record in a large Apennine catchment. *Geomorphology*, *188*, 42–53. https://doi.org/10.1016/j.geomorph.2012.12.006
Starr, J. L., & Paltineanu, I. C. (2002). Methods for measurement of soil water content: Capacitance devices. In J. H. Dane & G. C. Topp (Eds.), *Methods of soil analysis: Part 4 physical methods* (1660 pp.). Madison, WI: Soil Science Society of America.
Strobbia, C., & Cassiani, G. (2011). Refraction microtremors: Data analysis and diagnostics of key hypotheses. *Geophysics*, *76*(3), MA11–MA20. https://doi.org/10.1190/1.3560246
Telford, M. W., Geldart, L. P., & Sheriff, E. R. (1990). *Applied geophysics*. Cambridge, UK: Cambridge University Press. https://doi.org/10.1017/CBO9781139167932
Terzaghi, K. (1943). *Theoretical soil mechanic*. New York: John Wiley. https://doi.org/10.1002/9780470172766
Tokimatsu, K. (1997). Geotechnical site characterization using surface waves. Paper presented at 1st Intl. Conf. Earthquake Geotechnical Engineering, Tokyo.
Tokimatsu, K., Tamura, S., & Kojima, H. (1992). Effects of multiple modes on Rayleigh wave dispersion characteristics. *Journal of Geotechnical Engineering*, *118*(10), 1529–1543. https://doi.org/10.1061/(ASCE)0733-9410(1992)118:10(1529)
Van Asch, T. W. J., & Malet, J. P. (2009). Flow-type failures in fine-grained soils: An important aspect in landslide hazard analysis. *Natural Hazards and Earth System Sciences*, *9*(5), 1703–1711. https://doi.org/10.5194/nhess-9-1703-2009
Varnes, D. J., & Savage, W. Z. (1996). The Slumgullion earth flow: A large scale natural laboratory. U. S geological survey bulletin (2130), U.S. Government Printing Office.

4. PAPER 2

Surface-wave velocity measurements of shear stiffness of moving earthflows *

Berti M., Bertello L., Squarzoni G.

*Published in **Landslides**

Original Paper

Landslides
DOI 10.1007/s10346-018-1102-1
Received: 24 April 2018
Accepted: 5 November 2018

Matteo Berti · Lara Bertello · Gabriela Squarzoni

Surface-wave velocity measurements of shear stiffness of moving earthflows

Abstract Earthflows are a flow-like movement of plastic clayey soils characterized by long periods of slow motion (at rates averaging a few meters per year or less) alternated with short periods of rapid surges at high velocity (up to meters per hour). During rapid surges, most earthflows move over a long distance with a fluid-like behavior. Although the generation of flow-type failures is an important issue for hazard assessment, our knowledge is limited by the difficulty of monitoring the process in the field. This has led to different explanations for rapid earthflows including high pore–pressure generation along the basal slip surface, pervasive shearing, or material fluidization. One key question is whether or not earthflows can fluidize through remolding and water entrainment. If this occurs, the material can change from plastic to fluid as the soil moisture increases, causing the landslide to move as a viscous flow; if not, the material remains in a plastic state and, as suggested by many authors, the flow-like morphology shown by earthflows would result by distributed internal shears rather than real mass flow. In this study, we provide the first answer to this question by measuring the shear stiffness of four large active earthflows in the Northern Apennines of Italy. Shear stiffness was measured using two geophysical techniques, the multichannel analysis of surface waves (MASW) and the passive refraction microtremors (ReMi). Measurements were carried out just a few days after the mobilization of the landslides and repeated in the following 2–3 years to evaluate the change of elastic properties with time. Field data show that soon after the mobilization, earthflows are characterized by very low values of shear stiffness (about 5–15 MPa), typical of soft clay soils with the high-void ratio. Shear stiffness then increases 4–5 times in the following months (up to 40–60 MPa) as the earthflows slow down and the material consolidates. These data indicate that during a rapid movement, earthflows undergo a dramatic increase of porosity and water content that probably drive the transition from a solid to a fluid-like state.

Keywords Earthflow · Fluidization · Consolidation · Surface waves · Northern Apennines

Introduction

Flow-like landslides can occur in almost any geologic material on both terrestrial and submarine slopes (Hungr et al. 2005). These landslides show a high mobility compared to other types of landslides and move downslope as viscous fluids, flowing over the ground surface to spread on low-gradient areas (Hutchinson 1988; Cruden and Varnes 1996). Landslides of the flow type exhibit a great variability in dynamics and velocity (Mackey and Roering 2011; Simoni et al. 2013; Schulz et al. 2018). Hungr et al. (2001, 2014) identified 11 types of flow-like landslides based on a combination of material type and moisture content. The authors make a clear distinction between debris flows, mud flows, and earthflows. Earthflows are landslides in plastic clayey soils that move persistently over long periods at slow rates (meters per year or less) and undergo short rapid surges (velocity up to meters per hour) following critical rainfall (Malet et al. 2005; Ronchetti et al. 2007; Guerriero et al. 2017). Debris flows and mud flows are very rapid to extremely rapid landslides that travel downstream at a high speed (meters per minute or meters per second), and whose original water content "has been modified by mixing with surface water during motion" (Hungr et al. 2014, p. 170). Hungr et al. (2001) proposed that the term "mud" be used for clayey soils in or close to the liquid limit (liquidity index > 0.5), and the term "earth" for clayey soil close to the plastic limit (liquidity index < 0.5). Many researchers agree with the idea that earthflows remain in a plastic state even during a rapid motion (Keefer and Johnson 1983; Brunsden 1984; Coe et al. 2003) and attribute the flow-like morphology to distributed, internal shears rather than real mass flow (Fleming et al. 1988; Baum et al. 2003; Schulz et al. 2009).

Interestingly, however, there are a number of documented cases in which earthflows did not behave like rigid-plastic bodies. Several studies have shown that during a rapid motion, earthflows may entrain water and turn from plastic solids to viscous liquids, with a significant increase of soil porosity and a sudden drop of shear resistance (Picarelli et al. 2005; Pastor et al. 2010; Jongmans et al. 2015). The possibility that earthflows can significantly increase the water content relative to the source material is not considered in the Hungr's et al. classification, but it has both scientific and practical interest. In fact, any change of soil moisture directly affects landslide mobility and it is of special importance for hazard assessment, emergency response, and remediation works (Van Asch et al. 2007; Van Asch and Malet 2009). While a vast literature exists on these topics for debris flows (Choi et al. 2015; Aaron and Hungr 2016; Ashwood and Hungr 2016; Ng et al. 2017), the process of solid-to-fluid transition is basically unknown for earthflows and very few studies have been conducted so far to investigate this process in the field (Mainsant et al. 2012b; Mainsant et al. 2015; Carrière et al. 2018).

Mainsant et al. (2012a) first developed a novel monitoring technique based on the continuous measurements of surface-wave velocity specifically designed to study active earthflows. The authors detected a significant drop of shear wave velocity just before the reactivation of a monitored earthflow and, since surface wave velocity is closely related to shear stiffness, they concluded that there was a "decay in clay mechanical properties [..] in agreement with a yield stress viscoplastic behavior" (Mainsant et al. 2012a, p.9). Bertello et al. (2018) used a similar technique to monitor an active earthflow in the Northern Apennines of Italy. They showed that the shear stiffness of the clay soil is very low soon after a reactivation, then increases with time as the landslide slows down and the material consolidates. Both these studies provide evidence of changes in the material properties during surging. In particular, low-shear stiffness indicates high-void ratio and (since the material is fully saturated) high-water content.

Published online: 23 November 2018

Therefore, in these two cases, the earthflows softened by entraining water and the change of soil moisture probably spanned the solid-fluid boundary.

In this study, we used Rayleigh wave velocity to characterize four large earthflows that occurred recently in the Emilia-Romagna region (Northern Apennines of Italy). Rayleigh velocities were measured using the active multichannel analysis of surface waves (MASW) (Park et al. 1999) and the passive refraction microtremors (ReMi) techniques (Louie 2001). Periodic measurements were carried out to evaluate the variation with time of shear stiffness, and to infer the state of the earthflow material during surging. The same analysis was conducted for three rockslides to validate the methodology and compare the results. For the Montevecchio earthflow, we re-analyze some of the data published by Bertello et al. (2018) to make a connection with previous findings.

Case studies

The study focuses on seven landslides that occurred between February 2014 and March 2015 in the Emilia-Romagna region (Northern Apennines of Italy; Fig. 1). The mountainous part of the region is characterized by weak rocks, active tectonic uplift, and a mild Mediterranean climate with average annual rainfall around 1300–1400 mm. These factors make the region highly vulnerable to landslides, with more than 20% of the mountain territory covered by landslide deposits (Bertolini et al. 2005; Simoni et al. 2013).

The Emilia-Romagna region was recently hit by severe floods and landslides triggered by two periods of heavy rainfall. During the first period (25 December 2013–5 March 2014; Fig. 2a), more than 1500 mm of rainfall were recorded at higher elevations near the Apennine divide, and about 600 mm at lower elevations near the Po Plain (Fig. 1). These rainfalls exceeded the long-term mean values by a factor of 2–3 and triggered more than 500 landslides. According to the local geological survey, 18 landslides had an area greater than 1 ha. The second period of heavy rainfall (4 February 2015–27 March 2015; Fig. 2b) was characterized by a series of short-duration high-intensity rainfall events that occurred after two relatively dry months. The accumulated rainfall exceeded the long-term values by a factor of 3–5, triggering 17 landslides with an area greater than 1 ha.

Intensive field surveys were conducted to map the landslides that occurred during these two periods. For seven landslides, we carried out seismic surveys just a few days after the mobilization and repeated the measures several times in the following 2–3 years to evaluate the change of shear stiffness with time. Table 1 summarizes the main characteristics of the investigated landslides. Four are earthflows in clay or sandy-clay soils (Boceto, Montevecchio, Silla, and Puzzola) while three are rockslides in mudstone-sandstone flysch (Sintria, Becusano, and Zattaglia). The three rockslides were included as "control group" to validate the results obtained for the earthflows.

Boceto is a large earthflow located in the Parma province (Fig. 3a). It covers an area of 12 ha, and it is made up of fine-grained plastic clay derived from the weathering of a clay-shales bedrock (Argille di San Siro Fm., Cretaceous). The landslides reactivated in late 1896, then entered a long period of dormancy. The last mobilization occurred on February 10, 2014, after a rainfall of about 260 mm in 10 days. The failure started in the upper part of the slope as a roto-translational slide and rapidly evolved into an earthflow that propagated downslope reactivating the existing landslide deposit. Eyewitnesses reported a peak velocity of about 40 m/day. We surveyed the landslide 12 days after the failure. At that time, most of the earthflow surface was soft and apparently fluidized, with large areas where the material had the consistency of a clay slurry.

The Silla earthflow is located in the Bologna Province, on the left side of the Silla Valley (Fig. 3b). The earthflow is part of a large landslide complex which extends for more than 60 ha (Simoni and Berti 2007). The landslide material is a silty clay regolith with a scattered block of limestone produced by the weathering of a chaotic clay-shales mélange (Argille a Palombini Fm., Cretaceous). In the last century, the Silla earthflow reactivated two times (November 1994 and February 2014). The last mobilization occurred on February 10, 2014, at the end of a rainfall period characterized by 330 mm in 30 days. The mobilization started again as a single slide in the source area and propagated downslope with a peak velocity of about 50 m/day. In this case, however, the downslope movement mostly occurred as multiple, successive slides without a complete fluidization of the material. Eight days after the failure, when we surveyed the landslide, the material was completely disrupted but still relatively stiff.

The Montevecchio earthflow is located in the Forlì-Cesena province along the Savio Valley (Fig. 3c). It is a relatively small earthflow (about 18 ha) with a badland morphology in the upper part. Bedrock geology consists of recent marine deposits (Argille a Colombacci Fm., Messinian) made of marly and silty clay interbedded with thin layers of fine sandstone. These deposits form a clay-rich colluvium with scattered cobbles of weak sandstone. The Montevecchio earthflow reactivated eight times in the last century. The last period of activity started in February 2014 after a rainfall of 110 mm in 16 days and lasted for 17 months until June 2015. During this period, the earthflow underwent three major mobilization events characterized by the complete fluidization of the moving mass (Bertello et al. 2018). Peak velocities by GPS monitoring reached 20 m/day.

The Puzzola landslide is a small earthflow located in the Bologna province (Fig. 3d). Unlike the others, this landslide is a first-time failure of an undisturbed slope. The slope consists of a sandy-clay regolith overlying a parent rock made of massive arenites interbedded by pelitic turbidites. The landslide occurred in the night of February 10, 2014, after a rainfall of 106 mm in 9 days. The landslide was triggered by a small rotational slide (with an area less than 1 ha) located in the upper part of the slope that liquefied and flowed downslope entraining about 30–50.000 m^3 of material along the tracking path. Eyewitnesses reported a peak velocity of a few m/s. Such high velocities are not typical of earthflows, and can depend on a large number of sand particles (about 30%) that enhanced the mobility of the flow (Hungr et al. 2001).

The three rockslides (Sintria, Becusano, and Zattaglia; Fig. 4) occurred in the same valley during the same rainfall event (Fig. 2b). The bedrock consists of a regular alternation of thickly bedded sandstone and mudstone layers (Marno-Arenacea Formation). The sandstone/mudstone ratio is typically 2:1 to 1:2 with sandstone beds usually less than 1–2 m thick. Sliding failures are common in this rock when the bedding planes daylight with dip angles are greater than 8°–10°. The three rockslides show different characteristics that are significant for this study. The Sintria

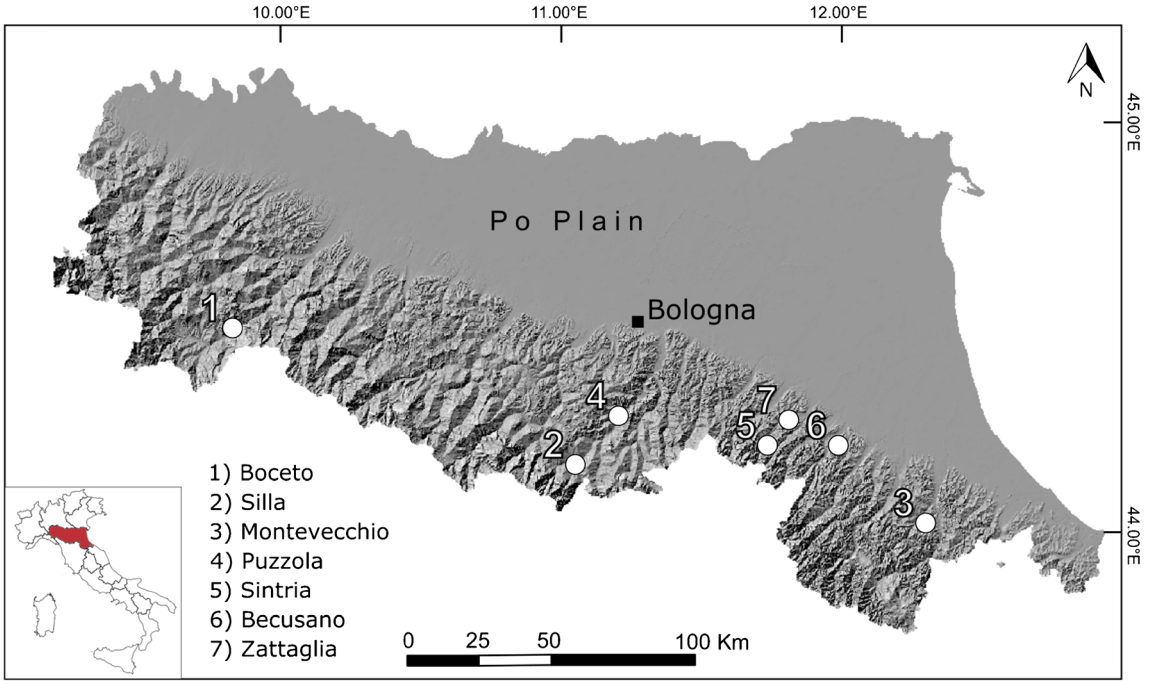

Fig. 1 Hillshade map of the Emilia-Romagna Region (Northern Italy) showing the location of the studied landslides

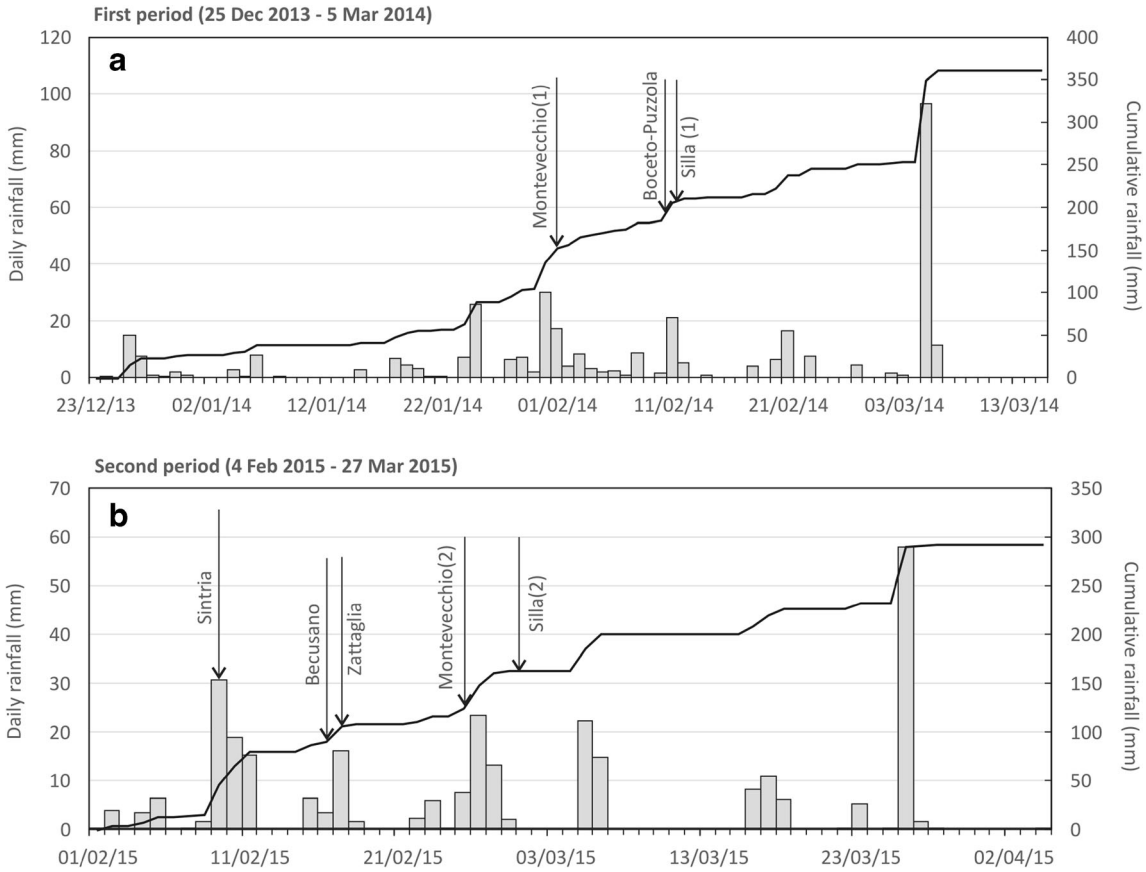

Fig. 2 Daily and cumulative rainfall recorded during the two critical rainfall periods (Casola Valsenio rain gage station; data from the Hydrological and Climate Services of the Emilia-Romagna Region). The arrows indicate the date of occurrence of the landslides

Table 1 Characteristics of the seven landslides considered in this study. Latitude (Lat) and longitude (Lon) are in WGS84. The type of landslide is defined using the Cruden and Varnes classification (1996). Multiple dates indicate different reactivation events

Landslide	Lat. (°)	Lon. (°)	Type	Bedrock	Length (m)	Width (m)	First-time failure	Date
Boceto	44.49	9.80	Earthflow	Clay shales	750	160	No	10/02/2014
Silla	44.20	10.98	Earthflow	Clay shales	1200	250	No	1) 11/02/20314
								2) 01/03/2015
Montevecchio	44.05	12.20	Earthflow	Silty clay	600	40–50	No	1) 01/02/2014
								2) 25/02/2015
								3) 25/05/2015
Puzzola	44.28	11.20	Earthflow	Sandy clay	300	25	Yes	10/02/2014
Sintria	44.19	11.66	Rockslide	Mudstone/sandstone	450	120	Yes	09/02/2015
Becusano	44.19	11.81	Rockslide	Mudstone/sandstone	610	120	Yes	16/02/2015
Zattaglia	44.22	11.70	Rockslide	Mudstone/sandstone	950	150	No	17/02/2015

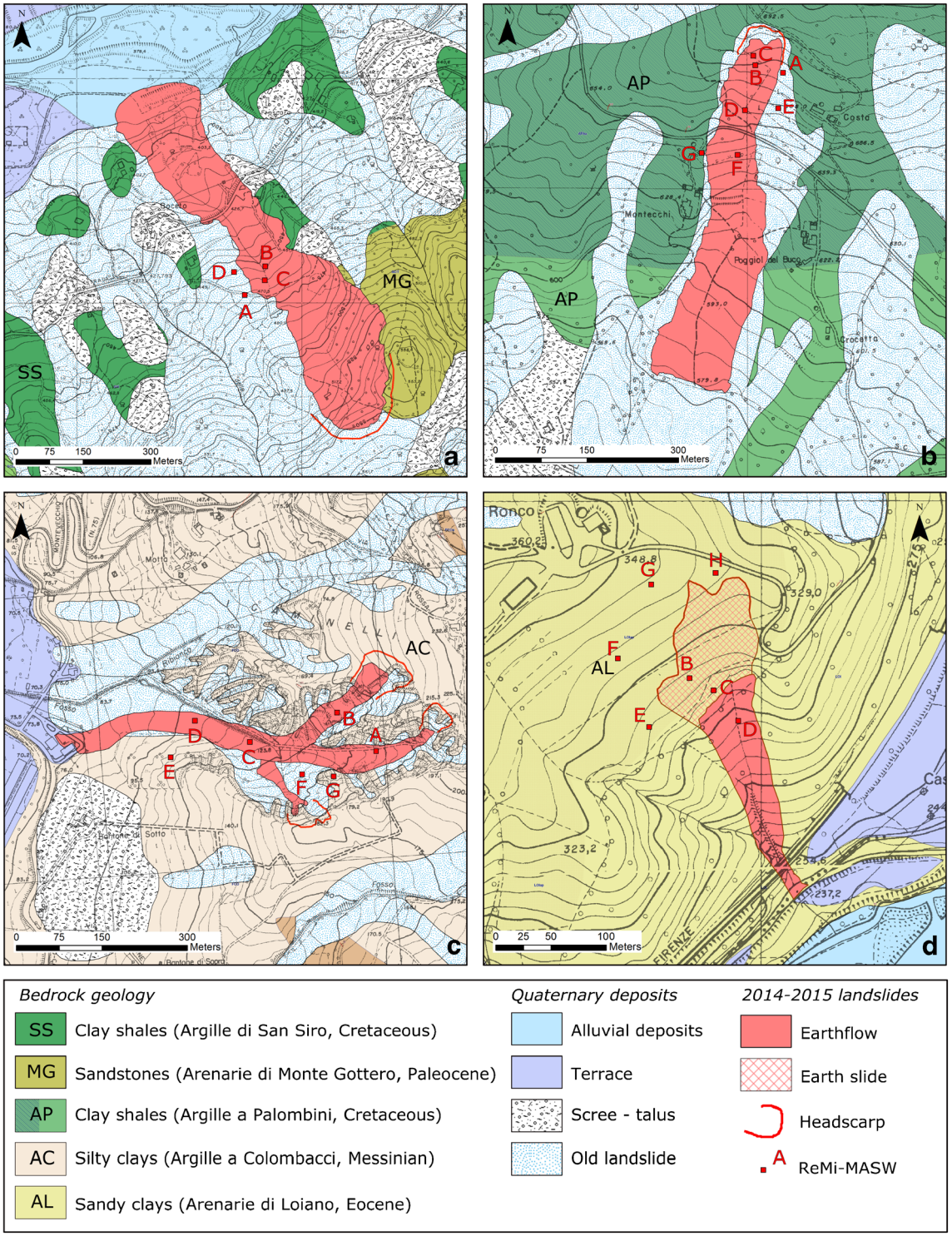

Fig. 3 Schematic geological maps of the four earthflows. (**a**) Boceto; (**b**) Silla; (**c**) Montevecchio; (**d**) Puzzola

rockslide (Fig. 4a) is a catastrophic, first-time failure that displaced about 250.000 m^3 of undisturbed rock mass down the slope for about 150 m. The displaced material dammed the river and run up the opposite valley side destroying a house. The landslide deposit has two parts: a mostly intact rock block that came to rest after having moved along the slip surface, and a frontal coarse-grained debris (Fig. 4a). The Becusano rockslide (Fig. 4b) is an incipient first-time failure that had not yet collapsed. On February 16, 2015, the landslide moved downslope of about 10 m. Numerous extension cracks and trenches appeared in the upper part of the slope but the displaced mass quickly came to rest and no further movements occurred. Zattaglia (Fig. 4c) is a dormant rockslide

characterized by periodic, impulsive movements. During the last century, the landslide reactivated three times though the slope and did not collapse. On February 16, 2015 the rockslide moved downslope for several meters then stopped.

Methodology

Periodic seismic surveys were carried out in the seven landslides to characterize the elastic properties of the material and their variation over time. The basic idea is to use shear stiffness as an indicator of material state. In general, the shear modulus of a soil depends on the void ratio, shear strain, and effective stress level (Lambe and Whitman 1969). Typical values of small-strain shear modulus range from 5 to 10 MPa for soft clays to 50–350 MPa for dense sands and gravels (Ortiz and Simo 1986). In the special case of a liquefied material, the shear stiffness should be close to zero because the shear wave velocity is zero in fluids (Reynolds 1997). Therefore, if an earthflow turns into a viscous fluid, the shear stiffness would be very low during the surge (or immediately after) and progressively increase over time as the earthflow slows down and the material returns to a plastic state. On the contrary, if the earthflow moves as a rigid-block and the material does not fluidize, the shear stiffness should remain relatively high (although somewhat smaller than the source material) and constant with time. Both the absolute value and the variation of shear stiffness with time can provide insights into earthflow dynamics.

Field surveys combined the multichannel analysis of surface waves (MASW; Park et al. 1999) and the refraction microtremors (ReMi; Louie 2001) techniques. These techniques allow evaluating the shear-wave velocity of the subsoil through the analysis of Rayleigh surface waves (Addo and Robertson 1992). The two techniques basically exploit the dispersive nature of the seismic waves that travel along the earth's surface. Wave dispersion results in different propagation velocities and penetration depths for different wavelengths. Short wavelengths have shallow penetration depth and normally propagate slower (due to the low velocity of the shallow layers) while longer ones have a deeper penetration and propagate faster. The plot of wave velocity versus frequency is called a dispersion curve (Aki and Richards 1980). In the MASW technique, geophones are placed along a straight line and a seismic signal is provided by an artificial source. ReMi technique has the same field setup but uses the seismic ambient noise (e.g., traffic, wind, or ocean waves) as the energy source (Louie 2001). Seismic ambient noise spans a wider frequency range and potentially works better in the mid- to the low-frequency domain (mid to high depths). However, the signal produced by an artificial source is generally stronger and better defined (Mulargia and Castellaro 2013). As result, the investigation depth of ReMi surveys is generally higher but the measurements are less accurate.

In both cases, the seismic signal arrives at the various geophones at different times, depending on material properties and on the distance from the source. A cross-correlation analysis of the recorded signals allows evaluating the Rayleigh velocity of the subsoil (Park et al. 1998; Park et al. 1999). The analysis involves the following steps (Fig. 5): (i) the recorded trace of each geophone is transformed from the time to the frequency domain by applying the Fourier transform; (ii) the wavefields existing at all traces are summed in one field record; (iii) the summation is repeated by considering different time-offsets that correspond to different velocities of surface waves (loop in Fig. 5b). Each phase velocity generates an amplitude spectrum which has the largest value for the correct (most probable) phase velocity. The amplitude spectra are then normalized in the range 0–1 to obtain a frequency-velocity graph (dispersion pattern) like the one shown in Fig. 5c. In the figure, the colors indicate the amplitude of Rayleigh velocity for each frequency. The locus along the peaks of amplitude over different frequency gives the dispersion curve of the subsoil. Since for a given frequency, there are multiple velocities at which waves can travel, the analysis also provides the dispersion curves of higher modes (Park et al. 1999; Louie 2001). Higher modes have low-energy content and are usually neglected in final estimation of wave velocity. Only the fundamental mode of propagation is considered, which corresponds to the dispersion curve with the lowest velocity (Fig. 5c).

Dispersion curves can be picked manually (Tokimatsu et al. 1992; Foti et al. 2014) and inverted using the relationship $z = \lambda/2.5$ (Foti et al. 2014; Castellaro 2016), where $\lambda$is the wavelength, to obtain the depth profile of Rayleigh velocity (V_r). Figure 6a shows an example dispersion curve and the corresponding inversion profile. The graduated color bar shows the probability density distribution of the normalized cross-correlation function, while the blue squares indicate the most probable velocity values for each frequency. The dotted lines in Fig. 6b are the error bars associated with the velocity profile, here defined as the 0.8 probability limits around the dispersion curve.

The small-strain shear modulus (G_o) can be readily obtained from Rayleigh velocity using the general elastic theory:

$$G_o = \rho \cdot V_s^2 \tag{1}$$

where ρ is material density and V_s is the shear-wave velocity, that for a homogeneous Poisson's half-space is proportional to Rayleigh velocity (Achenbach 2012):

$$V_s \approx 1.1 \cdot V_r \tag{2}$$

In our case, the density of the material varies considerably among the landslides. Laboratory tests conducted on clay samples taken in the four earthflows show bulk density ranging from 1400 kg/m^3 (at a water content close to the liquid limit) to 1800 kg/m^3 (at the plastic limit). For the three, the rockslides bulk density varies from 1800 to 1900 kg/m^3 in the loose debris to 2100–2300 kg/m^3 in the fractured rock mass. Despite such a large variability, sensitivity analysis showed that G_o is not very sensitive to ρ. We, therefore, assumed two constant values of bulk density for earthflows ($\rho = 1600 kg/m^3$) and rockslides ($\rho = 1900 kg/m^3$).

The main source of uncertainty in the method is the identification of the dispersion curve. Bad geophones coupling, electronic noise, and complex site conditions are the common factors responsible for a difficult identification of the fundamental mode, especially in the low-frequency range (Ben-Menahem and Singh 1981). For this reason, the quality of the MASW and ReMi measurements was preliminarily checked in the field with a notebook after recording the signal. We retained only the dispersion curves where the fundamental mode was clearly defined between 5 Hz

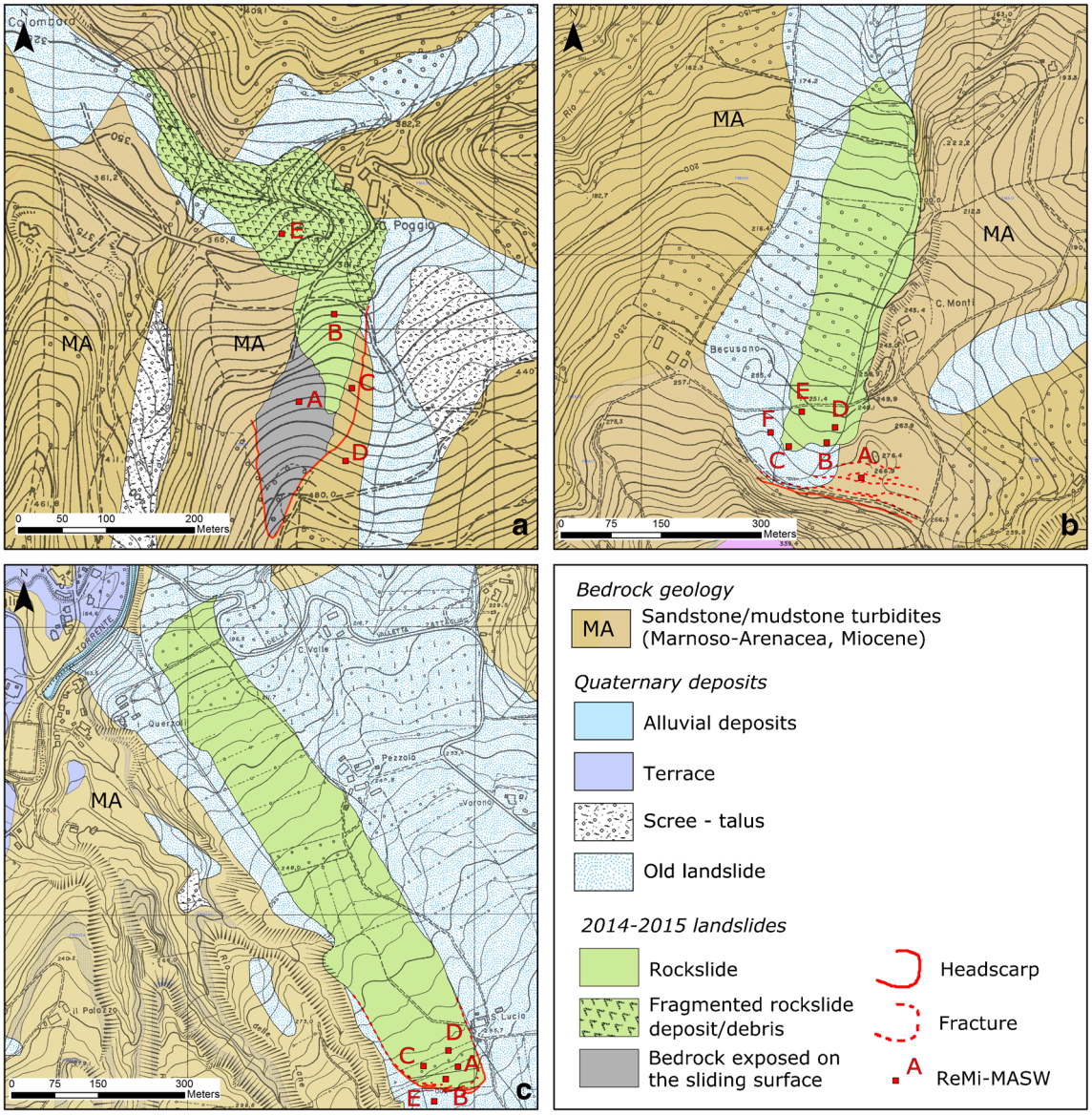

Fig. 4 Schematic geological maps of the three rockslides. (**a**) Sintria; (**b**) Beucsano; (**c**) Zattaglia

and 50 Hz and well distinguishable from the higher modes. The typical error on Rayleigh velocity at shallow depth (less than 5 m) was about 10–15% of the central value.

From February 2014 to August 2017, we acquired 176 MASW-ReMi profiles, 142 of which is on earthflows and 34 on rockslides. Each seismic profile consisted of an array of six vertical polarized geophones at 4.5 Hz, spaced 2 m for earthflows (total length of the seismic line 10 m) and 5 m for rockslides (total length of the seismic line is 25 m). As suggested by Louie (2001), we used a single geophone sensor for each channel. The first 5 min of each acquisition was performed in the passive mode acquiring the ambient noise (ReMi), and the last minute was in the active mode, using the jump of an operator about 5 m far from the first geophone as an active source (MASW). The maximum investigation depth was almost 12 m for both earthflows and rockslides. All the measurements were performed with the Soilspy Rosina array (Moho s.r.l) and data were processed using the Grilla software (MoHo s.r.l.).

ReMi-MASW surveys were conducted at different locations both within the landslides and on the stable surrounding slopes (Figs. 3 and 4). The surveys outside the landslides were done for validation, given that Rayleigh velocities on stable slopes should not vary with time. We attempted to carry out the seismic investigations in the middle of landslides, where the thickness of the deposit is greater and the velocity (or the deformation associated to the movement) is higher, to ensure that Rayleigh velocity was not affected by the bedrock and to characterize the active part of the landslides. Unfortunately, especially shortly after the mobilization, most earthflows were not accessible because of the soft, muddy ground or for the presence of trenches and open fractures. In these cases, seismic investigations were carried out as far as possible from the landslide boundary.

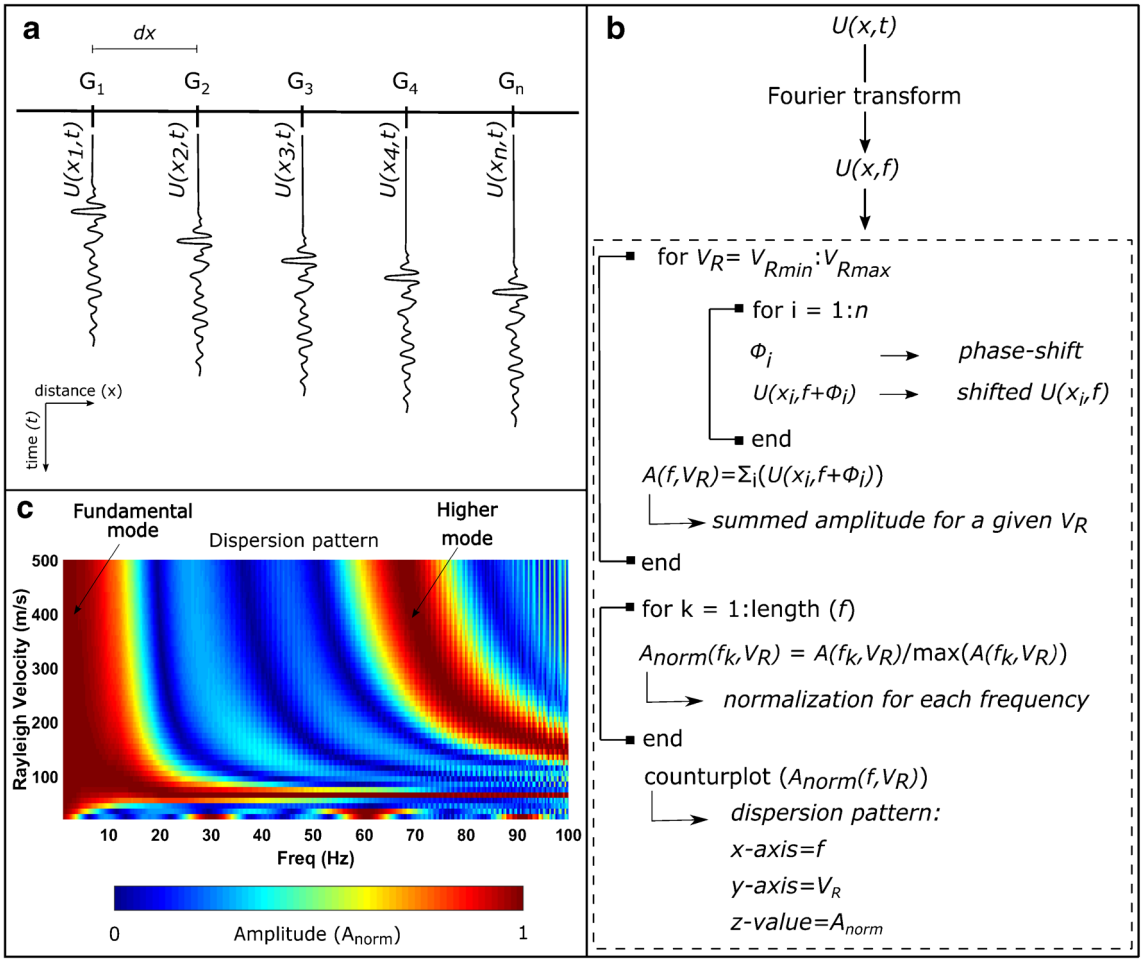

Fig. 5 Conceptual example of a MASW/ReMi survey. (**a**) schematic geophone array (G1-Gn); (**b**) flowchart of the solving algorithm (Park et al. 1998); (**c**) frequency-velocity plot showing the experimental propagation velocity distribution of a surface wave at a specific frequency. x=distance; t=time; f=frequency;$U(x, t)$=recorded signal in time domain; $U(f, t)$=recorded signal in frequency domain; V_R=tentative value of Rayleigh wave velocity that iterates between two arbitrary values (min and max); ϕ=phase wave velocity; $A(f, V_R)$=stack of the shifted signal; $A_{norm}(f, V_R)$=stack of the normalized shifted signal

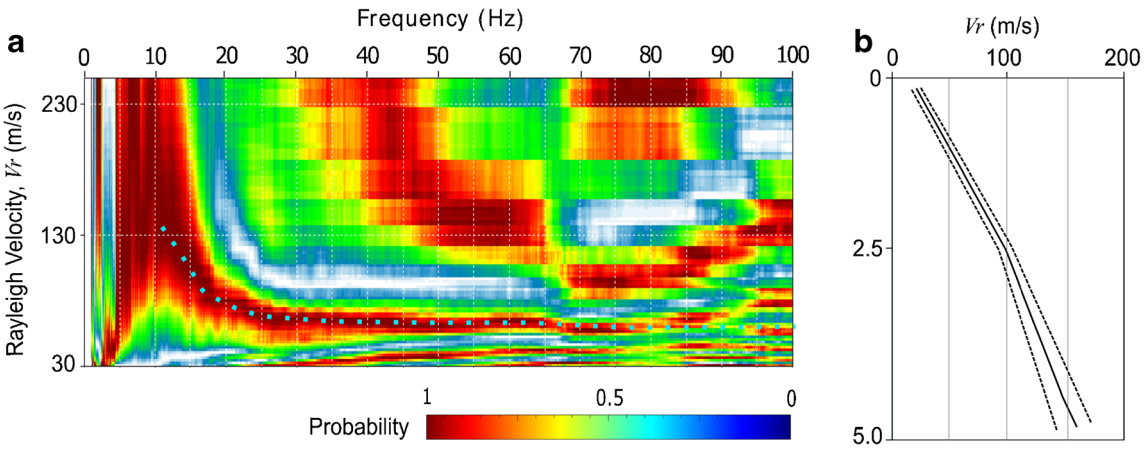

Fig. 6 Sample result of a MASW/ReMi survey (Montevecchio landslide, section C). (**a**) frequency-velocity plot showing the velocity distribution of surface waves at a specific frequency. The graduated color bar shows the probability density distribution of the normalized cross-correlation function; the blue dots indicate the most probable velocity values for each frequency. (**b**) Rayleigh-wave velocity profile obtained by the dispersion curve

Table 2 Summary table showing the values of Rayleigh velocity measured at a depth of 2 m by the MASW-ReMi surveys. The numbers in brackets indicate different reactivation events of the same landslide (see Table 1). Capital letters indicate the measurement sections (see Figs. 3 and 4 for location). The seismic surveys carried out outside the landslides are highlighted with gray background

Landslide	Time after earthflow mobilization t_m (day)	Rayleigh velocity at 2.0 m, V_r (m/s)							
		A	B	C	D	E	F	G	H
Boceto (BOCE)	12	163	136	75	/	/	/	/	/
	269	181	159	139	/	/	/	/	/
	1128	/	170	170	/	/	/	/	/
Montevecchio (1) (MNTV1)	10	79	85	80	51	184	127	126	/
	38	116	95	89	67	123	171	124	/
	93	136	95	90	75	201	129	128	/
	123	/	103	95	74	/	/	/	/
	271	/	104	105	75	/	/	/	90
	297	/	/	87		/	/	/	/
Montevecchio (2) (MNTV2)	14	/	/	66	64	/	/	/	/
	27	/	/	64	/	/	/	/	/
	51	/	98	100	88	/	/	/	/
	58	117	92	80	/	187	120	115	/
	64	/	/	83	/	/	/	/	/
	71	108	103	95	65	/	125	118	/
	83	100	80	83	78	/	/	/	/
Montevecchio (3) (MNTV3)	14	83	/	80	80	/	/	/	/
	25	/	74	74	70	/	/	/	/
	45	94	94	73	70	/	/	/	/
	52	/	83	73	/	/	/	/	/
	72	97	80	90	80	/	/	/	/
	94	/	/	94	/	/	/	/	/
	102	104	95	/	98	/	/	/	/
	680	/	/	/	97	194	/	/	/
Puzzola (PUZZ)	11	/	121	127	104	136	149	194	156
	67	/	116	/	119	136	171	190	176
	168	/	130	134	130	146	143	177	161
	353	/	142	148	138	/	/	/	183
	458	/	124	/	118	/	/	/	/
	1135	/	160	152	160	/	/	/	/
Silla (1) (SILL1)	8	254	195	151	104	207	186	236	/
	65	/	200	181	153	209	220	/	/
	168	214	187	140	191	209	169	234	/
	350	/	177	135	196	/	/	/	/
Silla (2) (SILL2)	29	/	75	89	75	/	93	/	/
	180	/	144	144	/	/	/	/	/
	765	263	152	164	/	/	/	/	/
Becusano (BECU)	2	177	103	99	94	92	168	/	/
	295	176	104	100	98	92	170	/	/
Sintria (SINT)	32	/	176	133	/	116	/	/	/
	101	527	145	125	/	152	132	/	/
	1298	528	150	125	/	152	/	/	/
Zattaglia (ZATT)	18	112	105	119	127	147	/	/	/
	937	125	109	124	135	148	/	/	/

Results

Table 2 summarizes the results of the geophysical surveys carried out in the seven landslides. Each row reports the value of Rayleigh velocity measured at a depth of 2 m (chosen as reference depth to compare the different landslides) at a certain time t_m, defined as the number of days elapsed from the mobilization of the landslide. The term "mobilization" is used here to denote the stage of rapid motion when the landslide attains its peak velocity (meters per hour for earthflows; meters per minute or per second for rockslides) and large displacements occur. The paroxysmal phase of movement generally lasts 1–2 days for earthflows and few seconds or minutes for rockslides. In the case of multiple reactivations, the time reported in Table 2 refers to the last mobilization event before the survey.

The first surveys were conducted just a few days after the mobilization. The results of these measurements are shown in Figs. 7 and 8. Each plot compares the profiles of Rayleigh velocity obtained in the different sections, highlighting the

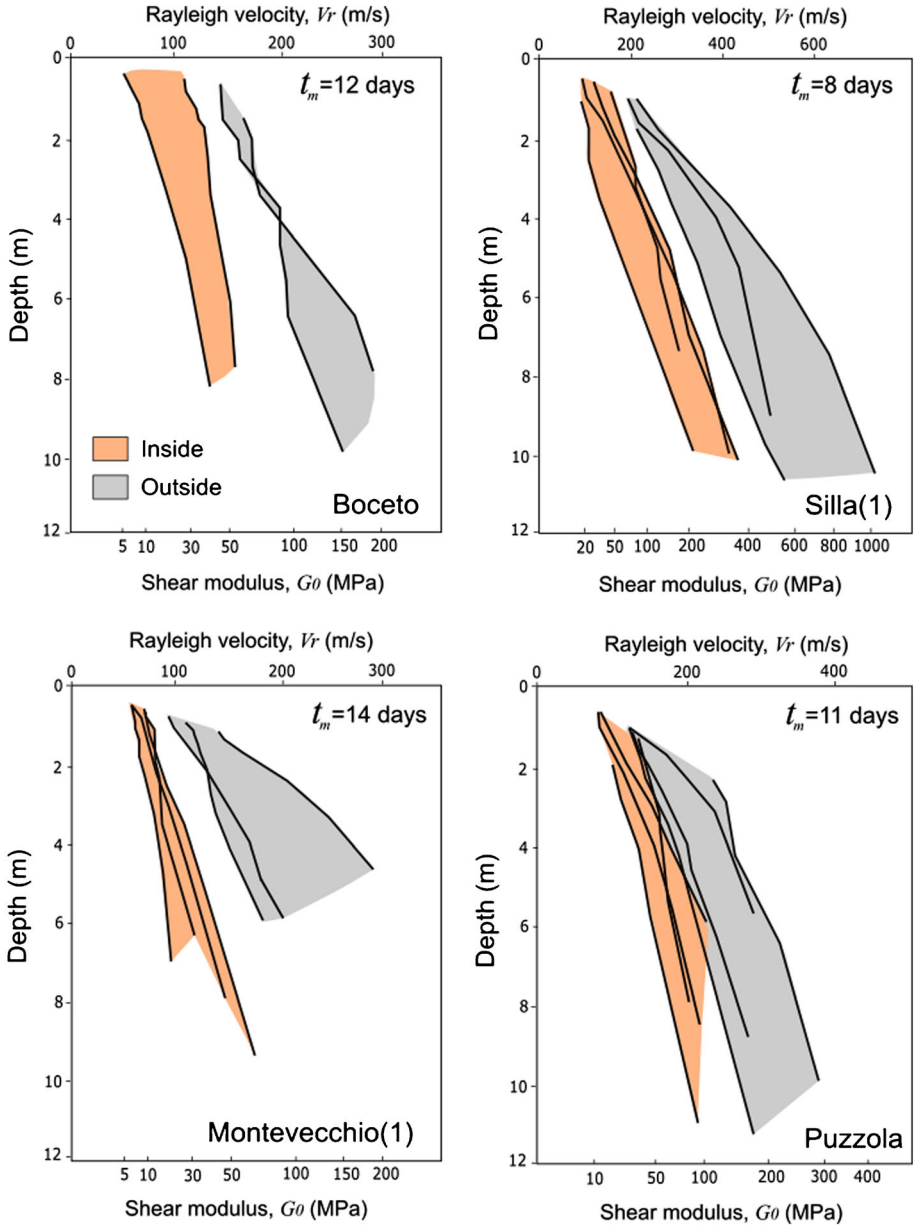

Fig. 7 Vertical profiles of Rayleigh velocity (V_r) and small-strain shear modulus (G_0) measured inside and outside the earthflows soon after the mobilization. t_m indicates the time elapsed from the mobilization event. Note that the shear modulus axis in non-linear

difference in seismic velocity inside and outside the landslides. The lower x-axis shows the equivalent values of shear modulus G_o computed by Eqs. (1) and (2). In general, the shear stiffness measured inside the landslides is much lower than that measured outside. However, the magnitude of the difference, as well as the absolute values of shear modulus, differ from case to case and well agree with the field conditions described in the "Case Studies" section.

The lower values of shear stiffness (5–15 MPa) were measured at Boceto and Montevecchio landslides (Fig. 7) that moved downslope like a thick slurry. In these earthflows, the mobilization was accompanied by a significant softening of the material with an apparent increase of the water content (see Case studies section). The soil turned into a clay slurry and became so soft to not support a person's weight; sometimes, we placed a wooden plank on the ground to avoid sinking into the mud. The very low values of G_o confirm these evidences. At Silla, although the material is essentially the same, the movement occurred as a series of multiple slides without a complete fluidization. This explains the higher values of shear stiffness measured soon after the mobilization (30–60 MPa, Fig. 7). The Puzzola landslide turned into a rapid flow of fully liquefied material. However, liquefied areas were not accessible, so we carried out the seismic profiles in the upper part of the initial slide (see Case studies section). For this reason, there is a relatively small difference (20%) between the shear modulus inside and outside the landslide (Fig. 7).

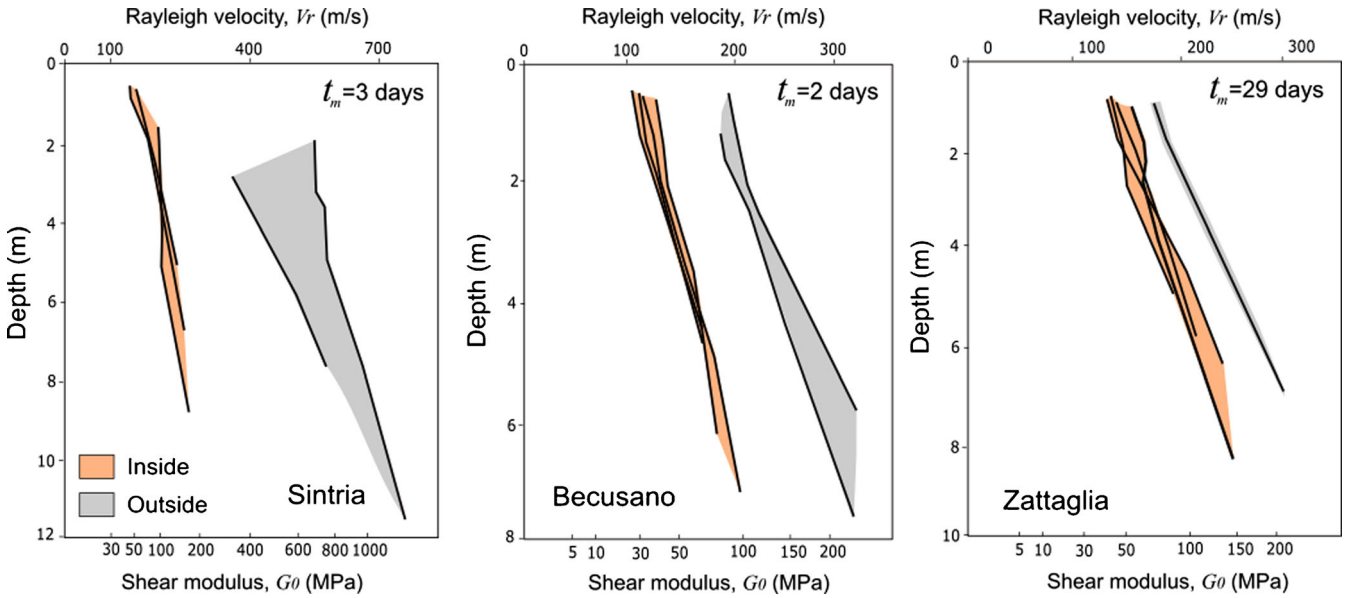

Fig. 8 Vertical profiles of Rayleigh velocity (V_r) and small-strain shear modulus (G_0) measured inside and outside the rockslides soon after the mobilization. t_m indicates the time elapsed from the mobilization event. Note that the shear modulus axis in non-linear

The deposit of the Sintria rockslide (Fig. 8) shows a dramatic drop in stiffness (about 80%) compared to the source material. In this case, the effect of the movement is particularly strong because the landslide is a first-time failure of a previously unsheared flysch rock (see Case studies section). The fresh bedrock exposed on the slip surface has a seismic velocity higher than 400–500 m/s, while the fragmented displaced material has $V_r < 150$–200 m/s. This corresponds to a decrease of shear modulus from about 450 MPa to 70 MPa. At Becusano, the difference in shear stiffness between the landslide and the source material is less (about 50%, Fig. 8) because the movement affected a partly weathered bedrock and the slope did not collapse. An even smaller difference (about 15–20%, Fig. 8) is found at Zattaglia, which is part of a dormant rockslide complex that in February 2015 moved downslope only a few meters.

The measurements carried out in the months after the mobilization revealed a different trend for rockslides and earthflows. In rockslides (as expected), the shear stiffness remained essentially constant with time (Table 2). In fact, the rockslide deposits consist of a highly fractured rock mass or non-plastic coarse debris for which no change in porosity or moisture content is expected after failure. Instead, 18 out of the 22 seismic profiles carried out in the earthflows (82% of the cases) show an increase in shear stiffness over time t_m (Fig. 9). In this case, G_o is at minimum a few days after the mobilization, rapidly increases in the first 2–3 weeks, and finally attains an asymptotic value after several months. The experimental points follow an approximate logarithmic trend that levels off to the shear stiffness of the undisturbed material. Unfortunately, each case is unique in terms of landslide thickness, residual movement, hydrological conditions, and the effect of consolidation works. It is therefore not possible to make a detailed assessment of the different trends. For example, the slow increase of G_o observed at Montevecchio after the second reactivation (March to May 2015, MNTV2 in Fig. 9) is due to the instability in the source area that provided constant sediment supply to the earthflow channel (Bertello et al. 2018).

Figure 10 combines the data of the four earthflows in a single chart. The general trend is clearly visible despite the large scatter. Soon after a surge (t_m=10–15 days), the shear modulus is very low, with most of the values falling between 5 and 15 MPa. Only in few cases (for example at Silla, sections B and C) G_o remains relatively high. As the earthflows slow down, the shear modulus increases by a factor of 4 to 5 and reaches a nearly constant value of 40–60 MPa within a couple of years. Based on the typical values of G_o for clay soils (Ortiz and Simo 1986) field measurements indicate that the earthflow material changes from "very soft" to "stiff" after mobilization. In the long-term, the shear stiffness measured inside the earthflows tends asymptotically to the values measured outside, which remain essentially constant thorough time (Fig. 11).

Discussion

The periodic surveys carried out in the four earthflows show that the shear stiffness of the displaced material changes with time after mobilization (Fig. 10). The shear modulus is the order of 5–15 MPa soon after the failure and increases up to 40–60 MPa in a couple of years, with most of the gain taking place in the first weeks. This remarkable increase in stiffness is even more striking if we consider that the first surveys were carried out a few days after the surge when the landslides velocity had already decreased from meters per hour to centimeters per day. During a surge (t_m=0), the shear modulus had to be even smaller, less than 1 MPa based on the initial slope of the curves of Fig. 10. As the shear modulus is zero in fluids, this is a strong point in favor of a fluid-like state of the moving mass.

The muddy lobes and the flow-like structures observed in the field (see Case studies section) confirm the idea that at least in

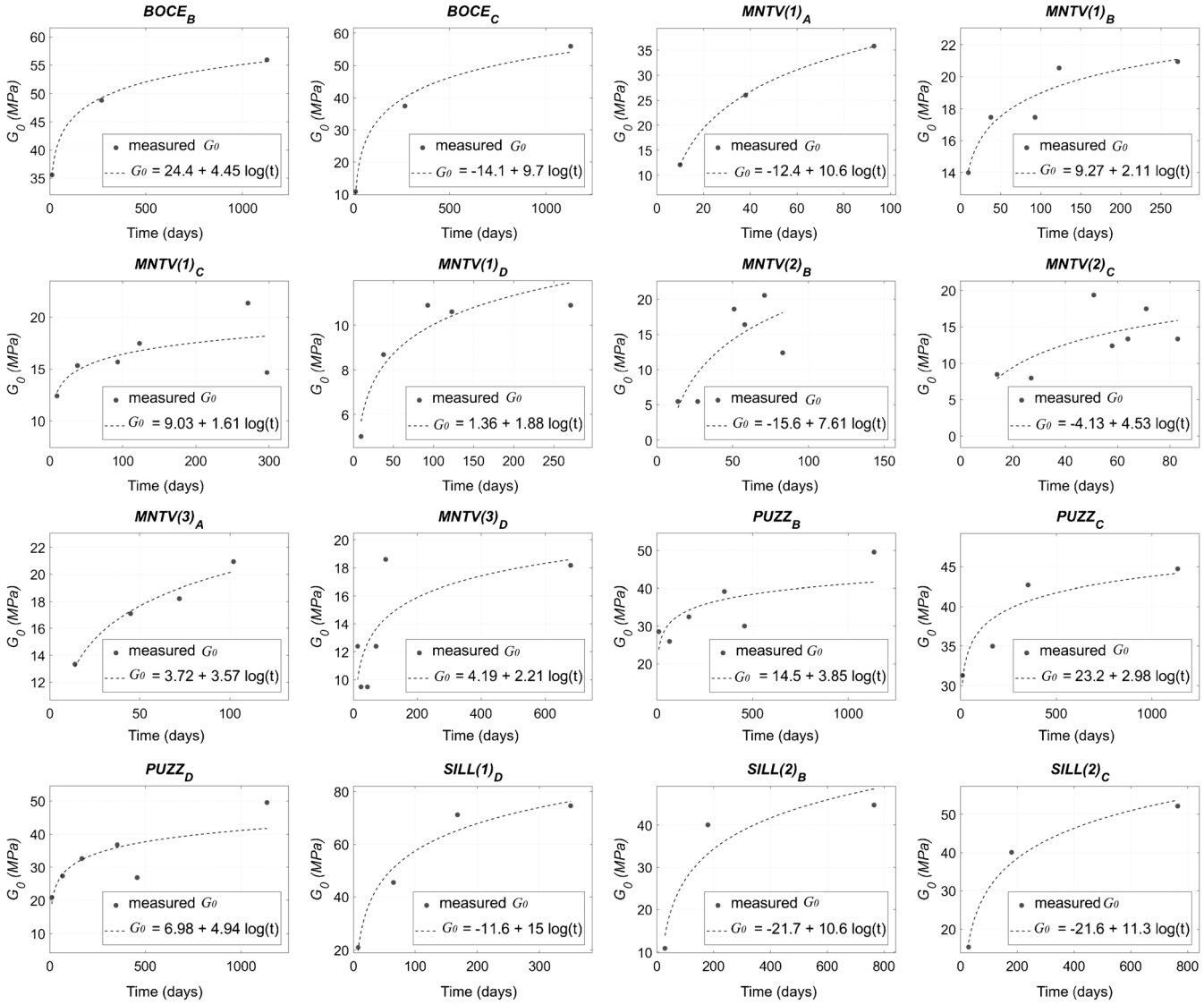

Fig. 9 Plots showing the variation with time of shear modulus measured at a depth of 2 m in the four earthflows. Time is reported as days elapsed from the mobilization event. Dashed curves show the logarithmic fit of the data points

three cases (Boceto, Montevecchio, and Puzzola) the mobilization was accompanied by the fluidization of the moving mass. Unfortunately, available data do not allow a more in-depth analysis of this process. What seems to be clear from our observations is that these earthflows can evolve into a viscous fluid through remolding and water entrainment, which causes an increase of soil porosity and moisture content (see also Bertello et al. 2018). The presence of fissures and cracks that characterizes these soils (Berti and Simoni 2010; Shao et al. 2016) certainly plays an important role in softening the material, allowing the water to soak into the ground and the clay on the fissure walls to swell.

The data also show that in the long term, the fluid material returns in a plastic state. The longtime over which this process develops, as well as the logarithmic trend of the stiffness increase, suggest that the clay is undergoing a consolidation process. The consolidation of a porous material involves a reduction in pores volume and the expulsion of water. In our case, it could mark the transition from a fluid-supported to a grain-supported soil structure. Since the void ratio e is directly related to shear stiffness (Kokusho et al. 1982; Lo Presti et al. 1997) we can use the one-dimensional consolidation theory (Terzaghi 1943) to verify this hypothesis. Bertello et al. (2018) carried out a similar analysis for the Montevecchio dataset.

The Terzaghi's theory describes the rate of consolidation of a homogeneous, saturated, compressible soil layer under a constant load (in our case the landslide mass under its own weight). The theory leads to a differential equation that predicts the excess pore water pressure (u) and the void ratio (e) at any point in time (t) and depth (z):

$$\frac{\partial u}{\partial t} = c_v \frac{\partial^2 u}{\partial z^2} \tag{3}$$

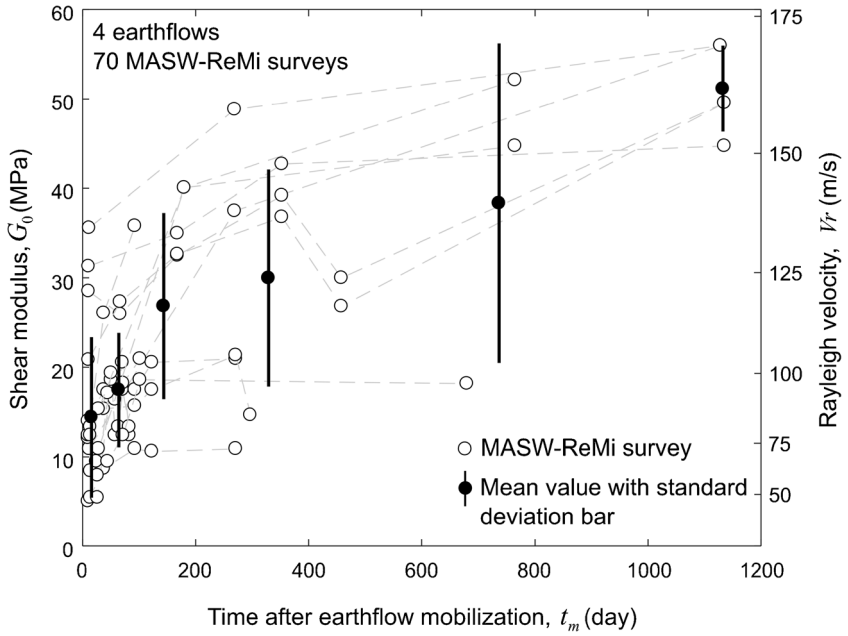

Fig. 10 Summary plot of the data shown in Fig. 9. The dashed lines connect the measurements carried out in the same section. Mean values of shear modulus and associated error bars (± 1 standard error around the mean) are computed for bins at t_m=0, 30, 100, 200, 500, 800, 1200 days. Right y-axis shows the raw values of Rayleigh velocity (note that the scale is non-linear)

where c_v is the coefficient of consolidation:

$$c_v = \frac{k}{\rho_w g}\frac{1+e_o}{a_v} \tag{4}$$

with ρ_w=water density, g=gravity constant, k=coefficient of permeability, e_o=initial void ratio, and a_v=coefficient of soil compressibility determined by oedometric test. The coefficient of consolidation c_v contains the material properties that govern the consolidation process.

Equation (3) can be solved using analytical or numerical techniques with proper boundary conditions. For our case, we assume an initial pore pressure distribution (u_o) constant with depth and complete drainage at the top of the landslide. The solution is obtained as a Fourier series in the following form:

$$U_z = 1 - \sum_{m=0}^{m=\infty} \frac{2}{M}\sin\left(\frac{Mz}{d}\right)e^{-M^2 T_v} \tag{5}$$

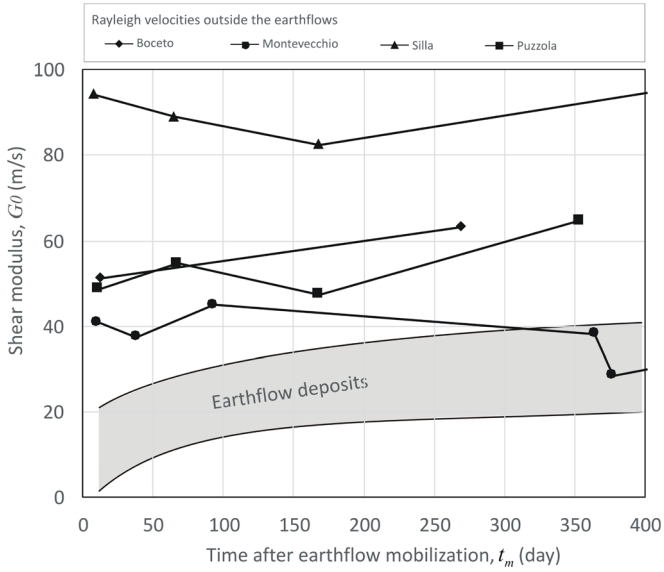

Fig. 11 Comparison of shear modulus measured outside the earthflows (black solid lines) with that measured inside (gray area "Earthflow deposits"). The upper and lower bounds of the gray area correspond to the errors bars shown in Fig. 10. All the data refer to a depth of 2 m

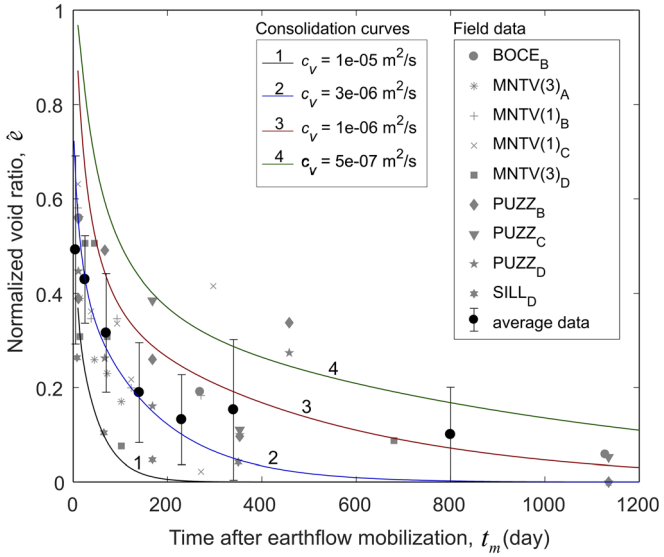

Fig. 12 Comparison between the normalized void ratio $\hat{e}$ predicted by the Terzaghi consolidation theory (consolidation curves) and that estimated from field data. Consolidation curves are calculated for different values of the coefficient of consolidation c_v. Field data are inferred from the small-strain shear modulus using the empirical formula of Santos and Correya (2000)

where $U_z = (u_o - u)/u_o$ is the degree of consolidation, d is the landslide thickness, $M = (2m + 1)\pi/2$, and $T_v = c_v t_m/d^2$ is a dimensionless time factor. U_z takes a value between 0 and 1 and can be expressed in terms of a normalized void ratio index $\hat{e}$:

$$\hat{e} = 1 - U_z = \frac{e - e_1}{e_o - e_1} \tag{6}$$

where e_o is the initial void ratio, e_1 the final void ratio, and e is the void ratio at an instant t_m during the consolidation process. $\hat{e}$ decays from 1 to 0 as the consolidation proceeds.

Figure 12 shows the curves of $\hat{e}$ versus t_m predicted by the consolidation theory. The curves are calculated using d=10 m (which is the representative thickness of our earthflows), $z = 2$ m (the reference depth of the geophysical measurements), and varying the coefficient of consolidation c_v over a wide range typical of clay soils (Holtz and Kovacs 1981). As can be seen, the consolidation equation predicts a rapid change of void ratio in the first weeks followed by a slow decline in the remaining period. The landslides reach the 60% degree of consolidation in a time between 10 days and 6 months depending on the coefficient of consolidation c_v. These results explain the nonlinear increase of seismic velocity and shear stiffness measured in the field (Fig. 10), given that both V_r and G_o are inversely correlated to e.

Unfortunately, a direct comparison between computed and measured values of the void ratio is not possible due to the lack of field measurements. For a qualitative comparison, we can infer the void ratio of the earthflow material from the measured values of a small-strain shear modulus using the empirical relationship proposed by Santos and Correia (2000):

$$e = \left(\frac{4000 p^{0.5}}{G_o}\right)^{0.77} \tag{7}$$

where p is the mean effective stress at a depth of 2 m. The values must be normalized to unity to be comparable with (6). We used the following formula:

$$\hat{e} = \frac{e - e_{min}}{e_{max} - e_{min}} \tag{8}$$

where e_{max} is the initial void ratio (before the consolidation starts) and e_{min} is the final void ratio after a long time. e_{max} and e_{min} were estimated as the void ratio predicted by the regression equations in Fig. 9 respectively 1 day and 4 years after the mobilization. The results are shown in Fig. 12. Each point represents the normalized void ratio at a certain time, estimated from the measured values of G_o. As can be seen, the data points well agree with the theoretical curves, indicating that the observed increase of shear stiffness is likely due to the consolidation of the earthflow material after the mobilization. Of course, there is a large uncertainty in this comparison, mainly related to the validity of the empirical Formula (7) in our complex field conditions and to the effect of fissures and cracks on the measured values of seismic velocity. Nonetheless, the data provide sufficient information that during rapid motion earthflows undergo a strong increase of soil porosity, and since in a saturated soil porosity is equal to soil moisture, this confirms the hypothesis that the material is a fluid-like state.

Conclusion

The following conclusions can be drawn from this study:

- Soon after the mobilization, the shear modulus of the earthflow material is 40–50% lower than that measured outside the landslide areas, though the surrounding slopes are made of weathered clay soils and dormant landslide deposits; this proves that the movement is accompanied by strong internal deformations

- In three cases (Boceto, Montevecchio, and Puzzola earthflows), the shear modulus after mobilization is extremely low, in the order of few MPa; such low values, besides the fact that the first surveys were carried out when the earthflows were already decelerating, suggest that during the stage of a rapid motion (when the earthflow moves at a speed of several meters/h) the material is in a fluid-like state
- The shear stiffness progressively increases as the earthflows slow down and the soil consolidates; in the long term, the displaced material recovers its original state, indicating that the changes induced by the mobilization are temporary and reversible
- As expected, the shear stiffness of the rockslide deposits is much lower than the source rock (up to 80%) and does not increase with time; in this case, the displaced material consists of non-plastic debris or highly fractured rock mass, therefore, no change of porosity and water content occurs

These results well agree with those obtained by Bertello et al. (2018), which analyzed the variation of the surface-wave velocity of the Montevecchio earthflow both after and before the three reactivations using the data recorded by a continuous monitoring system. In both cases, earthflows entrained a significant amount of water that softened the material driving the transition from a solid to a fluid-like state. The physical interpretation of this process is beyond the scope of this paper and beyond the available data set. Nonetheless, we believe that this is an important issue that should be considered and properly investigated in future studies on earthflows.

Acknowledgments

This work was supported by the Civil Protection Agency of the Emilia-Romagna Region under the framework agreement "Special activities on support to the forecast and emergency planning of Civil Protection with respect to hydrogeological risk" (ASPER-RER, 2011–2015 and 2016-2021). The authors would also like to acknowledge the Editor and the anonymous reviewers for their constructive comments and suggestions. All the data used in this paper are listed in the references or are included in the figures and tables.

References

Aaron J, Hungr O (2016) Dynamic simulation of the motion of partially coherent landslides. Eng Geol 205:1–11

Achenbach JD (2012) Wave propagation in elastic solids. Elsevier, Amsterdam

Addo KO, Robertson PK (1992) Shear-wave velocity measurement of soils using Rayleigh waves. Can Geotech J 29:558–568

Aki K, Richards PG (1980) Quantitative seismology, theory and methods. Freeman, San Francisco

Ashwood W, Hungr O (2016) Estimating total resisting force in flexible barrier impacted by a granular avalanche using physical and numerical modeling. Can Geotech J 53(10):1700–1717

Baum RL, Savage WZ, Wasowski J (2003) Mechanics of Earth flows. Proceedings international workshop on occurrence and mechanisms of flows in natural slopes and earthfills, Sorrento Italy, May 15–16

Ben-Menahem A, Singh SJ (1981) Seismic waves and sources. Springer-Verlag, New York

Bertello L, Berti M, Castellaro S, Squarzoni G (2018) Dynamics of an active earthflow inferred from surface-wave monitoring. J Geophys Res Earth Surf 123(8):1811–1834

Berti M, Simoni A (2010) Field evidence of pore pressure diffusion in clayey soils prone to landsliding. J Geophys Res 115(F3):1–20

Bertolini G, Guida M, Pizziolo M (2005) Landslides in Emilia-Romagna region (Italy): strategies for hazard assessment and risk management. Landslides 2(4):302–312

Brunsden D (1984) Mudslides. In: Brunsden D, Prior DB (eds) Slope instability. Wiley, Chichester, pp 363–410

Carrière SR, Jongmans D, Chambon G, Bièvre G, Lanson B, Bertello L, Berti M, Jaboyedoff M, Malet JP, Chambers JE (2018) Rheological properties of clayey soils originating from flow-like landslides. Landslides 15:1615–1630. https://doi.org/10.1007/s10346-018-0972-6

Castellaro S (2016) Soil and structure damping from single station measurements. Soil Dyn Earthq Eng 90:480–493

Choi CE, Au-Yeung SCH, Ng CWW (2015) Flume investigation of landslide granular debris and water runup mechanisms. Geotech Lett 5(1):28–32

Coe JA, Ellis WL, Godt JW, Savage WZ, Savage JE, Michael JA, Kibler KD, Powers PS, Lidke DJ, Debray S (2003) Seasonal movement of the Slumgullion landslide determined from global positioning system surveys and field instrumentation, July 1998 – march 2002. Eng Geol 68:67–101

Cruden DM, Varnes DJ (1996) Landslide types and processes. In: Turner K, Schuster RL (eds) Special report, transportation research board. National Academy Press, Washington DC, p 36–75

Fleming RW, Johnson RB, Schuster RL (1988) The reactivation of the Manti landslide. In: The Manti, Utah, landslide, US Geological Survey Professional Paper 1311: 1–22

Foti S, Lai GC, Rix GJ, Strobbia C (2014) Surface wave methods for near-surface site characterization. CRC Press, Boca Raton

Guerriero L, Bertello L, Cardozo N, Berti M, Grelle G, Revellino P (2017) Unsteady sediment discharge in earth flows: a case study from the mount Pizzuto earth flow, southern Italy. Geomorphology 295:260–284

Holtz RD, Kovacs WD (1981) An introduction to geotechnical engineering. Prentice-hall civil engineering and engineering mechanics. Prentice-Hall, Englewood Cliffs

Hungr O, Evans SG, Bovis MJ, Hutchinson JN (2001) A review of the classification of the flow type. Environ Eng Geosci 7:221–238

Hungr O, McDougall S, Bovis M (2005) Entrainment of material by debris flows. In: Hungr O (ed) Debris-flow hazards and related phenomena. Springer, Berlin, pp 135–158

Hungr O, Leroueil S, Picarelli L (2014) The Varnes classification of landslide types, an update. Landslides 11:167–194

Hutchinson JN (1988) General report: morphological and geotechnical parameters of landslides in relation to geology and hydrogeology. Fifth International Symposium on Landslides, AA Balkema, Rotterdam 1: 3–36

Jongmans D, Baillet L, Larose E, Bottelin P, Mainsant G, Chambon G, Jaboyedoff M (2015) Application of ambient vibration techniques for monitoring the triggering of rapid landslides. Eng Geol Soc Territory 2:371–374

Keefer DK, Johnson AM (1983) Earthflows: morphology, mobilization and movement. US Geological Survey Professional Paper 1264

Kokusho T, Yoshida Y, Esashi Y (1982) Dynamic properties of soft clay for a wide strain range. Jpn Soc Soil Mech Found 22:1–18

Lambe TW, Whitman RV (1969) Soil mechanics. Wiley, New York

Lo Presti DCF, Jamiolkowski M, Pallara O, Cavallaro A, Pedroni S (1997) Shear modulus and damping of soils. Géotechnique 47(3):603–617

Louie JN (2001) Faster, better: shear-wave velocity to 100 meters depth from refraction microtremor arrays. Bull Seismol Soc Am 91(2):347–364

Mackey BH, Roering JJ (2011) Sediment yield, spatial characteristics, and the long-term evolution of active earthflows determined from airborne LiDAR and historical aerial photographs, Eel River, California. Geol Soc Am Bull 123(7–8):1560–1576

Mainsant G, Larose E, Bronnima C, Jongmans D, Michoud C, Jaboyedoff M (2012a) Ambient seismic noise monitoring of a clay landslide: toward failure prediction. Geophys Res Lett 117:1–12

Mainsant G, Jongmans D, Chambon G, Larose E, Baillet L (2012b) Shear-wave velocity as an indicator for rheological changes in clay materials: lessons from laboratory experiments. Geophys Res Lett 39(19):1–5

Mainsant G, Chambon G, Jongmans D, Larose E, Baillet L (2015) Shear-wave-velocity drop prior to clayey mass movement in laboratory flume experiment. Eng Geol 192:26–32

Malet JP, Laigle D, Remaitre A, Maquaire O (2005) Triggering conditions and mobility of debris flows associated to complex earthflows. Geomorphology 66:215–235

Mulargia F, Castellaro S (2013) A seismic passive imaging step beyond SPAC and ReMi. Geophysics 78:63–72

Ng CWW, Choi CE, Koo RCH, Kwan JSH (2017) Dry granular flow interaction with dual-barrier systems. Géotechnique 68(5):386–399

Ortiz M, Simo JS (1986) An analysis of a new class of integration algorithms for elastoplastic constitutive relation. Int J Numer Methods Eng 23(3):353–366

Park CB, Miller RD, Xia J (1998) Imaging dispersion curves of surface waves on multichannel record. 68th Ann. Internat. Mtg., Soc. Expl. Geophys., Expanded Abstracts, 1377–1380

Park C, Miller R, Xia J (1999) Multi-channel analysis of surface waves. Geophysics 64(3):800–808

Pastor M, Manzanal D, Fernandez Merodo JA, Mira P, Blanc T, Drempetic V, Pastor MJ, Haddad B, Sanchez M (2010) From solids to fluidized soils: diffuse failure mechanisms in geostructures with applications to fast catastrophic landslides. Granul Matter 12(3):211–228

Picarelli L, Urcioli L, Ramondini G, Comegna L (2005) Main features of mudslides in tectonised highly fissured clays shales. Landslides 2(1):15–30

Reynolds JM (1997) An introduction to applied and environmental geophysics. Wiley, Chichester

Ronchetti F, Borgatti L, Cervi F, Lucente CC, Veneziano M, Corsini A (2007) The Valoria landslide reactivation in 2005-2006 (Northern Apennines, Italy). Landslides 4(2):189–195

Santos JA, Correia G (2000) Shear modulus of soils under cyclic loading at small and medium strain level. Proceedings 12th World Conference on Earthquake Engineering, Auckland, New Zealand, paper n.0530

Schulz WH, Mackenna JP, Kibler JD, Biavati G (2009) Relations between hydrology and velocity of a continuously moving landslide – evidence of pore pressure feedback regulating landslide motion? Landslides 6:181–190

Schulz WH, Smith JB, Wang G, Jiang Y, Roering JJ (2018) Clayey landslide initiation and acceleration strongly modulated by soil swelling. Geophys Res Lett 45:1888–1896

Shao W, Bogaard T, Bakker M, Berti M (2016) The influence of preferential flow on pressure propagation and landslide triggering of the Rocca Pitigliana landslide. J Hydrol 543:360–372

Simoni A, Berti M (2007) Transient hydrological response of weathered clay shales and its implication for slope instability. Proc 1st north American landslide conference, Vail, Colorado, AEG Special Publication No 23: 886–898

Simoni A, Ponza A, Picotti V, Berti M, Dinelli E (2013) Earthflow sediment production and Holocene sediment record in a large apenninic catchment. Geomorphology 188:42–53

Terzaghi K (1943) Theoretical soil mechanic. Wiley, New York

Tokimatsu K, Tamura S, Kojima H (1992) Effects of multiple modes on Rayleigh wave dispersion characteristics. J Geotech Eng 118:1529–1543

Van Asch TWJ, Malet JP (2009) Flow-type failures in fine-grained soils: an important aspect in landslide hazard analysis. Nat Hazards Earth Syst Sci 9(5):1703–1711

Van Asch TWJ, Van Beek LPH, Bogaard T (2007) Problems in predicting the mobility of slow-moving landslides. Eng Geol 91:46–55

M. Berti (✉) · L. Bertello · G. Squarzoni
Dipartimento di Scienze Biologiche, Geologiche e Ambientali,
Università degli Studi di Bologna,
Via Zamboni 67, 40127, Bologna, Italy
Email: matteo.berti@unibo.it

5. METHODOLOGICAL ASPECTS ABOUT EARTHFLOWS BEHAVIOR INTERPRETATION

Iverson model

Describing landslide behavior by using numerical and analytical models is a common practice in the scientific literature (Desai, 1995; Brunsden, 1999; Ancey, 2007). Analytical techniques have been largely developed during the last century to treat the mechanics of landslide motion (e.g. Savage and Chleborad, 1982; Keefer and Johnson, 1983). Starting from the late 90s, numerical modeling has been applied to earthflows by various authors using different approaches to better understand the landslide evolution process (e.g., Picarelli et al. 1995; Angeli et al. 1996; van Asch et al. 2007).

However, Iverson (1985, 1986a,1986b) was the only one who proposed a physically based mathematical theory that can explain the main aspects of unsteady, nonuniform landslide motion. The theory is founded on physical conservation laws and a postulated constitutive model for the behavior of landslide material. The proposed constitutive equation represents soil as a viscoplastic material with yield strength dependent on effective confining pressure and viscosity dependent on deformation rate. This type of rheological model incorporates summed plastic and viscous components and may be depicted by a nonlinear dashpot-slider system (Figure 5.1).

The rate-dependent viscous flow is simulated by Iverson (1985,1986a) using nonlinear power-low constitutive equations, conservation of linear momentum equation and conservation of mass equation. The constitutive equations describe viscoplastic rheological behavior with friction-dependent plastic yielding and rate-dependent viscous flow. The equations are written in order to accommodate a wide range of special cases including linear viscoplastic behavior and perfectly plastic frictional slip. The conservation of momentum and conservation of mass equations are the same as proposed in the traditional physics of continuum (e.g. Bird et al., 1960, Malavern, 1969).

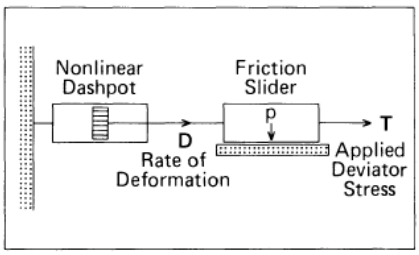

Figure 5.1. Dashpot-slider system (Iverson, 1985): the friction slider is a rigid block maintaining the deviator stress T if the yield stress is not exceeded. A critical combination of deviator stress and effective pressure p is required for yielding: if the yield stress is exceeded the motion occurs and the dashpot provides viscous resistance. Dashpot viscosity depends on the rate of deformation D.

As a first step, Iverson (1986a) derived equations for velocity and stress fields within the deforming part of a model landslide and simplified them by selecting the x-direction as the only one direction of the sediment flux. Then, he introduced the concept of steady-state of landslide motion: "if only a slow, steady, creep-like sediment passed through the head and toe of the landslide, the only external forces affecting motion of the landslide would be those due to gravity" (Iverson, 1986a). In such a case the equations reduce to analytical form and can be integrated to yield an expression for steady-state sediment flux.

The idealized datum state does not prevail exactly on any landslide but constraints can be acceptable if adequate time and deformation scales are considered: if large enough, departures from average annual behavior might be regarded as noise and not real departures from datum state; if the landslide behavior is studied in more specific terms even short fluctuations can be considered as significant departures from datum state.

The datum state motion can be mathematically analyzed: given the right assumptions the equations of motion can be used to derive expressions for velocity profile and sediment flux. The Iverson final equations describe the forces balance as summarize in the schematic diagram below (Figure 5.2 - a).

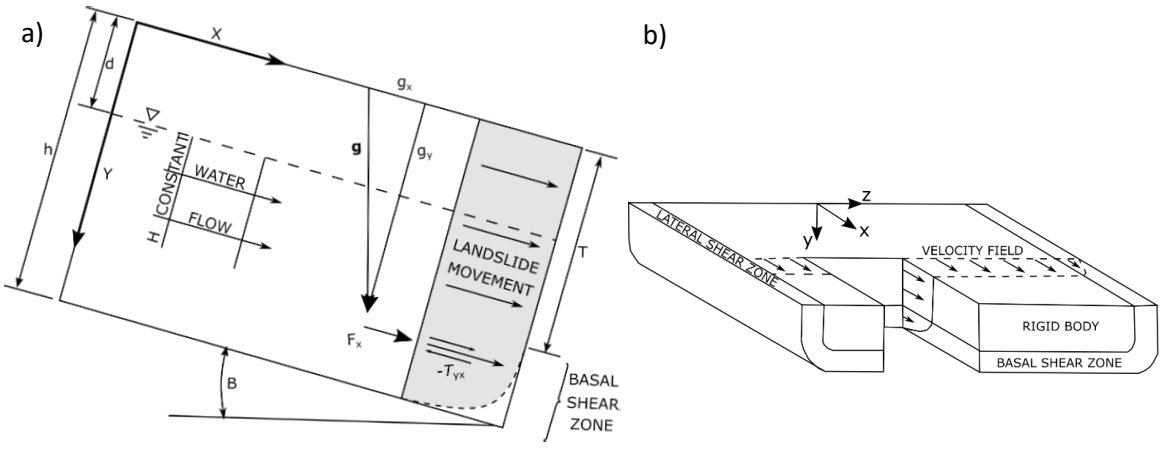

Figure 5.2: Landslide conceptual model in the Iverson theory (modified from Iverson, 1986a). a) Schematic diagram for steady-state deformation in a landslide cross-section in the x-y plane: F_x *drives the landslide motion and is given by the sum of the x-component of the buoyant soil weight and the ground-water seepage force;* h *is the total thickness of the landslide,* d *is the water table depth,* T *is the thickness of the plug,* T_{yx} *is the shear stress that arises from the drag of the deforming soil, and g is the gravity acceleration. b) Schematic y-z view showing the steady-state velocity field in a landslide with an ideal geometry: a rigid body moves downslope along basal and lateral shear-deformation zones.*

In the Iverson model the shear zone includes both the bottom of the landslide and the lateral boundaries (Figure 5.2 - b). The deformation occurs only into the shear zone, in which the velocity field variation develops. In the remaining part the velocity is constant and the landslide mass can be considered like a rigid body or a plug. For the same type of soil behavior (that can range from linear viscoplastic to perfectly plastic), velocity profiles vary depending on slope angle B, mechanical properties (cohesion c' and friction angle φ'), physical properties (saturated and unsaturated density of soils ρ_s and ρ_u, density of water ρ_w) and water table depth d. The thickness T of the rigid portion of the landslide (i.e. the plug) can vary from 0 to the landslide depth h depending on the cohesion value of the soil and the position of the water table. If either the cohesion or the water table depth is equal to 0, the entire mass behaves like fluid and the rigid portion vanishes.

Applying hypothetical values to the model highlights the influence of the parameters determining the velocity profiles. For example, if we consider a landslide characterized by h = 8 m, B = 15°, φ' = 18°, ρ_s = 1.8 x 10^3 kg/m^3, ρ_u = 1.7 x 10^3 kg/m^3 and set d = 0, we can see how a small cohesion contribution can affect the velocity profile. Attributing c' = 4 kPa, we obtain a plug 2 meters thick and a large shear zone (6 meters thick); attributing c' = 16 kPa the plug becomes thicker (= 7.7 meters) and the shear zone thinner (= 0.3 meters) that means that the mass basically slide along a shear slip surface (Figure 5.3-a). If we set c' = 0 in the same model and vary water table depth, we observe that d = 1 m is required for a 2 meters thick plug and a shear zone 6 meters large; d = 5 m produces instead a plug thicker than 7 m and a shear zone thinner than 1 meter (Figure 5.3-b). No-plug condition is reached when c' = 0 kPa and d = 0 m, which means that all the mass is fluidized (Figure 5.3-a, b).

The velocity profiles can be used for parameters estimation and the interpretation of the phenomenon. That is possible in dormant and suspended periods (Cruden and Varnes, 1996) during which gathering data is not such a difficult challenge. Following different authors (e.g. Picarelli, 2000), in the post-failure stage (i.e., dormant or suspended stage in the Cruden and Varnes classification) extremely slow movements can occur even for tens or hundreds years. In these conditions the soil behavior can be derived by inclinometer data fitting: a linear viscous behavior is characterized by different velocity-depth profiles if compared with a nonlinear viscous behavior (Iverson, 1985; Iverson, 1986a).

However, there are cases in which recovering field data is more difficult. An earthflow moving with velocities higher than some millimeters per month cannot be monitored by using inclinometer probes. In such conditions measuring depth-velocity profiles is almost impossible. From the Iverson model, it's clear that if both the cohesion and the water-table depth are equal to zero the entire mass behaves as a viscous fluid. Since theoretically the landslide occurring is characterized by zero cohesion (Skempton, 1985), a possible plug presence is due only to the position of the water table. It is reasonable to presume that the landslides occurring is affected by the presence of a water table near to the ground surface, as it's typical for the earthflows in the Emilia-Romagna region (Bertolini and Pellegrini, 2001). Considering c' = 0 kPa and d = 0 m excludes the existence of a plug during the activation/reactivation stage. In this case, the other parameters that affect the velocity distribution are the friction angle and the slope angle. Nevertheless, varying these parameters within a realistic range shows that the velocity of the landslide at the ground level does not change too much (Figure 5.3-c, d); for a landslide characterized by h = 8 m, c' = 0 kPa, d = 0 m, ρ_s = 1.8 x 10^3 kg/m^3, ρ_u = 1.7 x 10^3 kg/m^3 the velocity is about 1÷5x10^{-4} m/s that is 10÷40 m/d. The inferred values are consistent with the typical magnitude of active earthflows (Cruden and Varnes, 1996), with the typical values of Emilia-Romagna region (Bertolini and Pellegrini, 2001) and with the velocity values that in some cases we were able to measure (Paper 1 – Chapter 3).

The equation describing the motion and flux of a landslide during the steady state can be exploited to derive a model for the perturbated state. Even in this case, if the correct assumptions are taken into account, it's possible to develop a wholly analytical theory. The approach requires that "perturbations or departures from datum-state conditions have negligible effect on the form of the dynamic force balance that governs landslide motion. For spatially uniform perturbations this requirement is automatically satisfied. For nonuniform perturbations the requirement means that sediment-flux perturbations must be sufficiently small that the attendant perturbations in slope angle, landslide thickness and water table depth are at least an order of magnitude smaller than their datum-state values" (Iverson, 1986b). Once again, the proposed simplifications have different impacts depending on the size of the problem; if we consider large earthflows as the ones that affect our region the considerations above are not so far from the reality.

Starting from the steady-state sediment flux theory, Iverson (1986b) derived an inhomogeneous advective-diffusive equation that describes the one-dimensional kinematic behavior of perturbations in landslide flow. The advection term represents a downslope transfer of perturbations as kinematic waves. The diffusion term represents a transfer of sediment-flux perturbations from their source to points throughout the body of the landslide. Disturbances in volumetric sediment flux will propagate downslope in an advective way and at the same time diffuse outward from their source. However, diffusive effects decay away from the perturbation source, and the magnitude is a function of time. Following Iverson (1986b), for most earthflows, perturbations can travel downslope as sort of kinematic waves moving 5 to 50 times faster than the speed at which the sediment itself moves, depending on soil types and landslide properties.

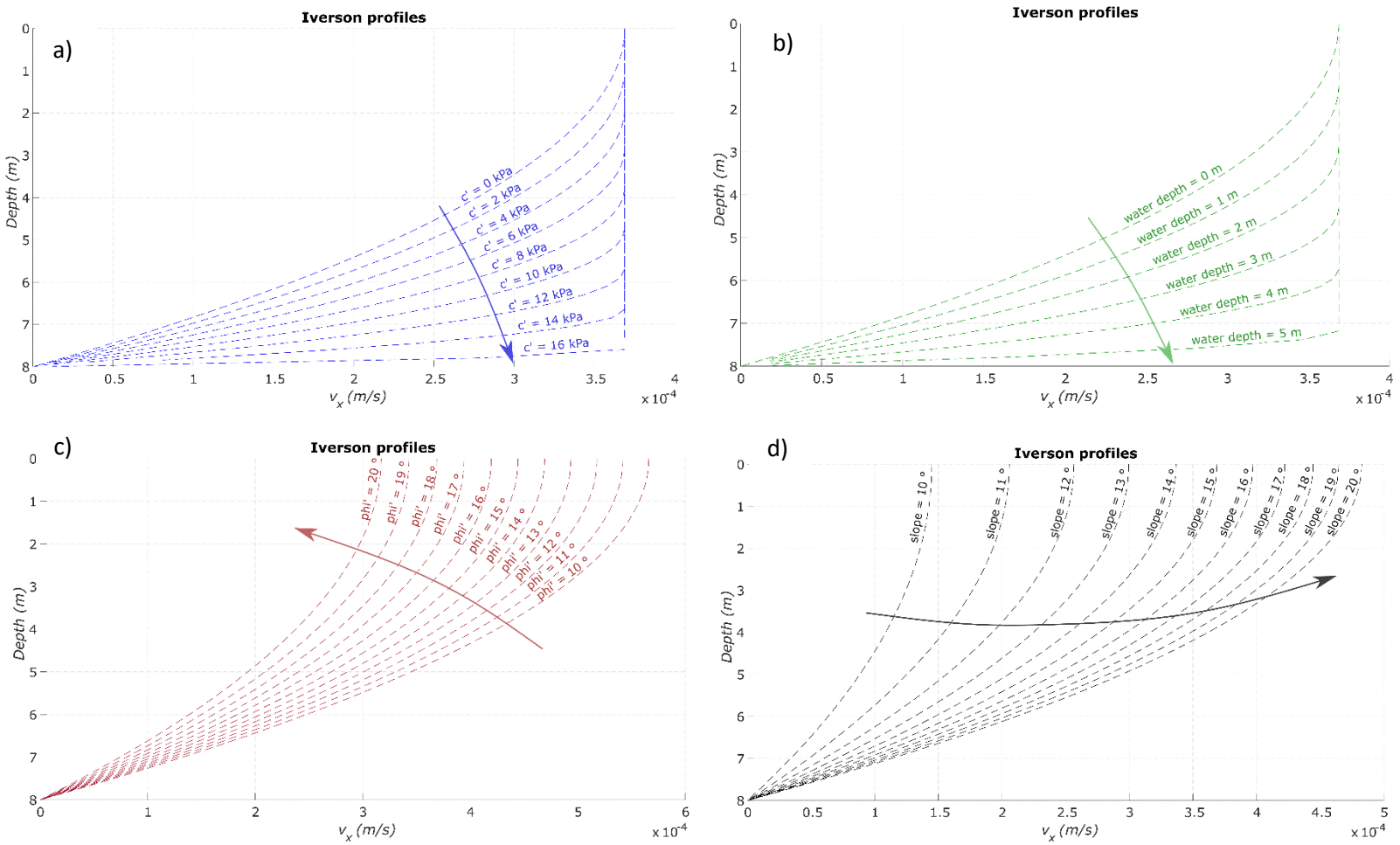

Figure 5.3: Velocity-depth profiles computed from the Iverson equations (Iverson, 1986a); the arrows highlight the increasing direction of the varying parameter. In all the cases ρ_s = 1.8 x 10^3 kg/m^3, ρ_u = 1.7 x 10^3 kg/m^3, n=1. The other parameters are: a) slope angle = 15°, friction angle = 18°, thickness = 8 m, water table depth = 0 m; b) slope angle = 15°, friction angle = 18°, thickness = 8 m, cohesion = 0 kPa; c) slope angle = 15°, thickness = 8 m, water table depth = 0 m, cohesion = 0 kPa; d) friction angle = 18°, thickness = 8 m, water table depth = 0 m, cohesion = 0 kPa.

The kinematic theory can be used to study how a perturbation occurring in the headscarp zone propagates downslope (Iverson, 1986b; Zhang et al., 1991). If the diffusive term prevails the landslide response is fast and the perturbation propagates rapidly downslope, even decaying soon after the impulse ceases. The theoretical extreme case is a soil deformation confined to a discrete thin slip surface: the entire mass would respond at once as expected for a perfectly plastic material. If the advective term prevails, the landslide response is slow and wave-like: that is what happens in highly viscous material. Applying the equations derived for the case of an impulse propagating from the headscarp to the toe, it's possible to compute the distribution of the perturbation in the landslide for different time steps. If the ratio between advective and diffusive terms changes, the propagation changes (Figure 5.4). Since the weight of the two terms is related to the soil behavior, the propagation process varies with landslide properties variation. The distribution of the perturbation depends mainly to the same parameters from which the sediment-flux in the datum state depends (Figure 5.5).

The kinematic model can be used to infer the propagation rate of a perturbation along the landslide. If we consider as "activated point" the distance at which the perturbating wave arrives for the first time and as "activating time" the time at which the perturbation reaches that point, we can compute the propagation rate of the landslide (Figure 5.6). Even if the type of perturbation is unknown, how it propagates is known. If the theory can be applied properly useful information can be provided to predict when a point along the slope will start to move. In this case, the parameters that mostly affect the "activating time" are cohesion and water-table depth: even if the shape of the propagation wave changes varying both the slope and the friction angles, the variation is smaller than for cohesion and water-table depth variation and, especially, the "activating time" for each "activated point" is almost the same (Figure 5.5-b,c). Hence, even in this case if the cohesion and the water-table depth don't vary too much from a perturbation event to another, the propagation rate is always quite the same. Since in active landslides the cohesion is theoretically equal to 0 (Skempton, 1985) and in this part of Apennines earthflows occur at d = 0 (Bertolini and Pellegrini, 2001), the theoretical kinematic behavior of the investigated landslide can be inferred.

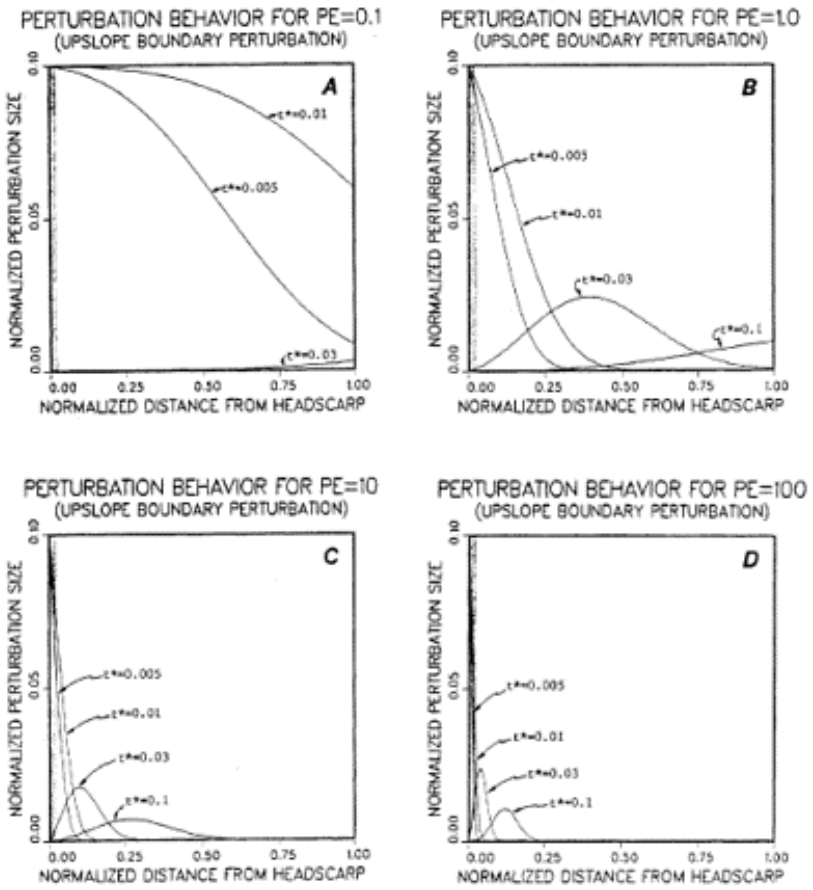

Figure 5.4: From Iverson (1986b): landslide response to an impulsive perturbation occurring in the headscarp area. On the y-axes the normalized perturbation, defined as the ratio between the volumetric sediment flux of the perturbation and the volumetric sediment flux of the datum state. On the x-axes the normalized distance from the headscarp x/L, in which x is the distance from the headscarp and L is the total length of the landslide. Each curve represents a different time step, as indicated by the labels. Pe *is the Peclet number: it represents the importance of advective transfer relative to diffusive transfer of sediment-flux perturbations and depends on landslide length, friction angle, slope angle water table depth, cohesion and other physical parameters. From a) to d) the* Pe *values changes while the duration of the perturbation does not. Iverson (1986b) shows how the propagation of the perturbation process varies by varying the ratio between advective and diffusive terms.*

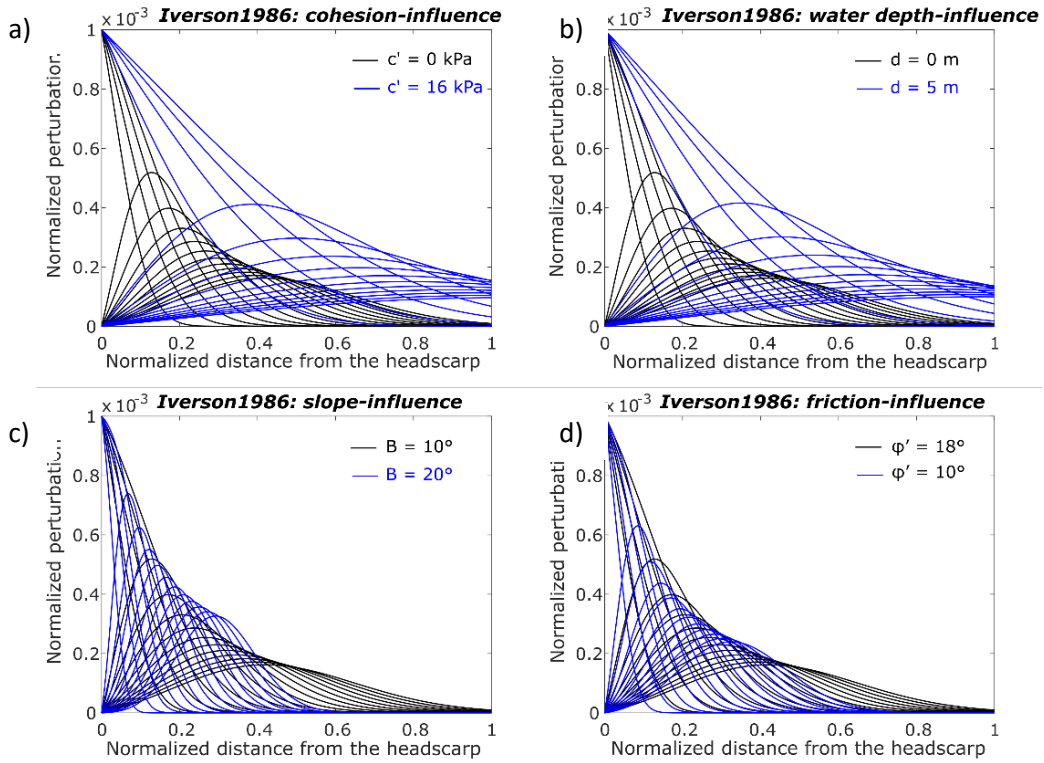

Figure 5.5: Iverson perturbation behavior for difference values of cohesion, water table depth, slope angle and friction angle. Each curve represents a different time step, as shown in Figure 5.4. In all the cases ρ_s = 1.8 x 10^3 kg/m^3, ρ_u = 1.7 x 10^3 kg/m^3, n=1, landslide length L = 800 m. The other parameters are: a) slope angle = 15°, friction angle = 18°, thickness = 8 m, water table depth = 0 m; b) slope angle = 15°, friction angle = 18°, thickness = 8 m, cohesion = 0 kPa; c) friction angle = 18°, thickness = 8 m, water table depth = 0 m, cohesion = 0 kPa; d) slope angle = 15°, thickness = 8 m, water table depth = 0 m, cohesion = 0 kPa.

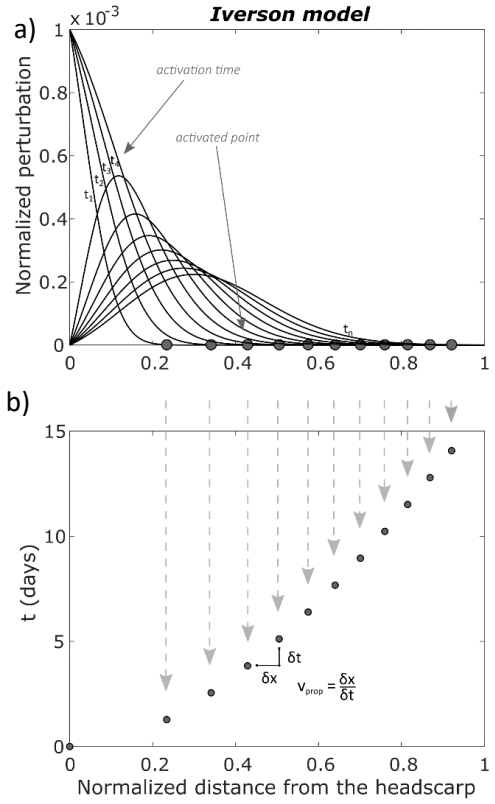

Figure 5.6: Propagation of perturbation process. a) A sketch of the Iverson curves (Iverson, 1986b) for an established normalized perturbation: each curve represents a different time step, as indicated by the labels. The "activation time" for each point is the time at which the perturbation reaches that specific point ("activated point"). b) A sketch of the derived distance-time plot: the "activation point" position is plotted against the "activation" time; the obtained curve can be used to infer the propagation rate of the perturbation.

Assessing the Iverson model application

Iverson theory is a physically based theory that can be used to explain both the dormant (i.e., post-failure slow motion) and active/reactivated stages of a large earthflow. The cohesion and the water table depth are the most influent parameters and they affect the fluid-like behavior of the landslide. The rigid-like behavior is reached for $c' \neq 0$ or $d \neq 0$. The flow-like behavior is related to $c' = 0$ and $d = 0$. The latter is the condition that is likely for the investigated earthflow. Cohesion equal to zero is typical for landslide occurring (Skempton, 1985) and a water depth level close to the ground surface is common during earthflow activation (Bertello et al., 2018, Berti et al., 2018; see Chap. 3, 4). Hence, following the Iverson laws, during the stages of "rapid surging" the entire earthflow mass should behave like a viscous flow. During the post-failure stage, an increase of water table depth leads the material to a sort of semi-rigid-like behavior.

The aim here is not to provide a specific model for a fluidization process; the goal is only providing a general overview of the problem in order to find a proper way to describe the observed process.

The postulates of the Iverson theory seem to explain the field measurements that have been presented in Paper 1 and Paper 2 (Chap. 3, 4). Far from the rapid surging the soil stiffness increases: the seismic surveys highlight that the stiffness of the earthflow (for a representative depth of 2 meters) is higher during the post-failure stage rather than just after the failure occurs. In the papers, this behavior is explained by a hypothetical fluidization process that tends to be reversed in the period following the proper failure. Unfortunately, our dataset cannot directly prove the theoretical laws derived by Iverson (1985, 1986a, 1986b) although the general behavior is consistent.

Besides the stiffness-related information provided in the papers presented above, other types of information have been gathered: (i) qualitative information about horizontal velocity distribution and (ii) data concerning the propagation velocity of perturbations. Both support the validity of the Iverson laws.

i) Time-lapse camera data show a nonuniform velocity of the earthflows at the ground surface. During the earthflow reactivation, the central part of the mass moves faster than the portions near to the boundaries. Since the cameras were placed in positions that affected the perspective of the recorded images and the image quality is not enough to perform proper video analysis, it has been not possible to recover quantitative data. Still, some information can be inferred. In Figure 5.7 there is an example derived from the May-2015 reactivation of Montevecchio earthflow (Forlì-Cesena province, Italy). This dataset includes a large number of images like the ones showed in the figure and has been processed using PIVlab (Thielicke, 2014; Thielicke and Stamhuis, 2014). PIVlab is a time-resolved particle image velocimetry (PIV) software that applies a cross-correlation algorithm to small sub-images to derive the most probable particle displacements. The measured displacements have been differentially scaled in order to consider the perspective effect. The targets used to the scaling process are affected by the low quality of the images so that a proper scaling is difficult to be obtained. In this sense, the result can be treated only in a qualitative way.

Figure 5.8 shows an example of velocity distribution derived from the frames analysis. The velocity distribution on the landslide surface is represented by different colors (Figure 5.8-a). The surface earthflow velocities throw sections have been averaged; a simple analytical solution for high viscosity flow in a rectangular channel (Cunningham, 1972) has been derived too by varying hypothetic viscosity values. The evidence that arises is that the velocity distribution is similar to the one of a high-viscous flow (Figure 5.8-b). In general, that means that the Iverson model is able to reproduce these types of earthflows by assuming a complete fluidization of the moving mass.

Figure 5.7: Examples of frames obtained from the time-lapse camera surveys.

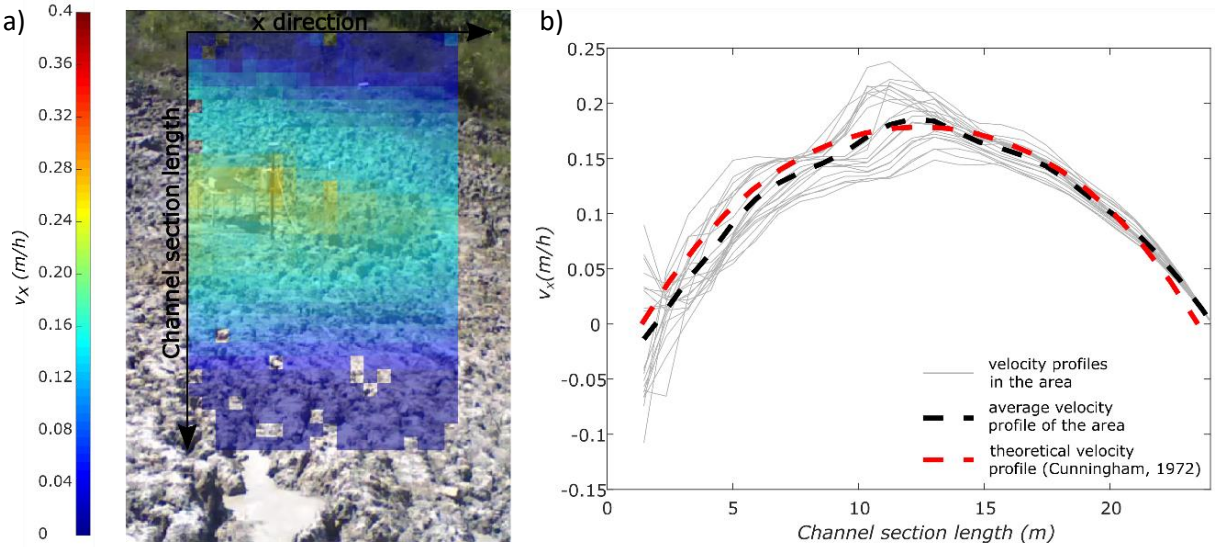

Figure 5.8: Example of velocity distribution derived from the May 2015 reactivation of the Montevecchio earthflow (Forlì-Cesena province, Italy). On the left the areal distribution of the velocity on the landslide surface. On the right the velocity along the cross-sections that can be derived from the image: each section corresponds to a column the colored frame; the black dashed line represents the average of all the profiles, the red one represents the theoretical profile derived for a high viscous flow (viscosity of about 10^6 kPa s) in a square-channel with slope equal to 10°.

ii) Data concerning the propagation of perturbations have been explored considering the reactivations of Valoria earthflow (Modena province, Italy). The landslide reactivated on November 2009 and in October 2010. Displacements had been continuously monitored during the period before and after the reactivations by using a robotic total station. Several targets had been tracked so that it has been possible to investigate the dynamic of reactivation: the displacement data have been used to understand if some propagation of perturbations process exists. Data for this analysis have been provided by Alessandro Corsini of the University of Modena.

During the reactivations the targets which started to accelerate first were located near to the headscarp. After a few days, the targets placed in the middle part of the earthflow started to accelerate too, and gradually the surge involved the targets below until it reached the toe. The same behavior has been observed during the two reactivations. The different portions of the landslide achieved maximum velocities of about some meters per day. If we computed the distance that a single portion can cover traveling at such velocities, it's clear the material belonging to one portion cannot reach the portion below until several months; the acceleration of the portion along the slope happens in a shorter period. Hence, we need to consider two different velocities: the flow velocity and the propagation rate of the "acceleration information". The former is the proper velocity of the flow (meters per day, at most), the latter is the rate that can be computed by considering the time interval between two consequent targets acceleration and the distance between them (Figure 5.9). The propagation rate of the "acceleration information" is faster than the flow rate (Figure 5.10).

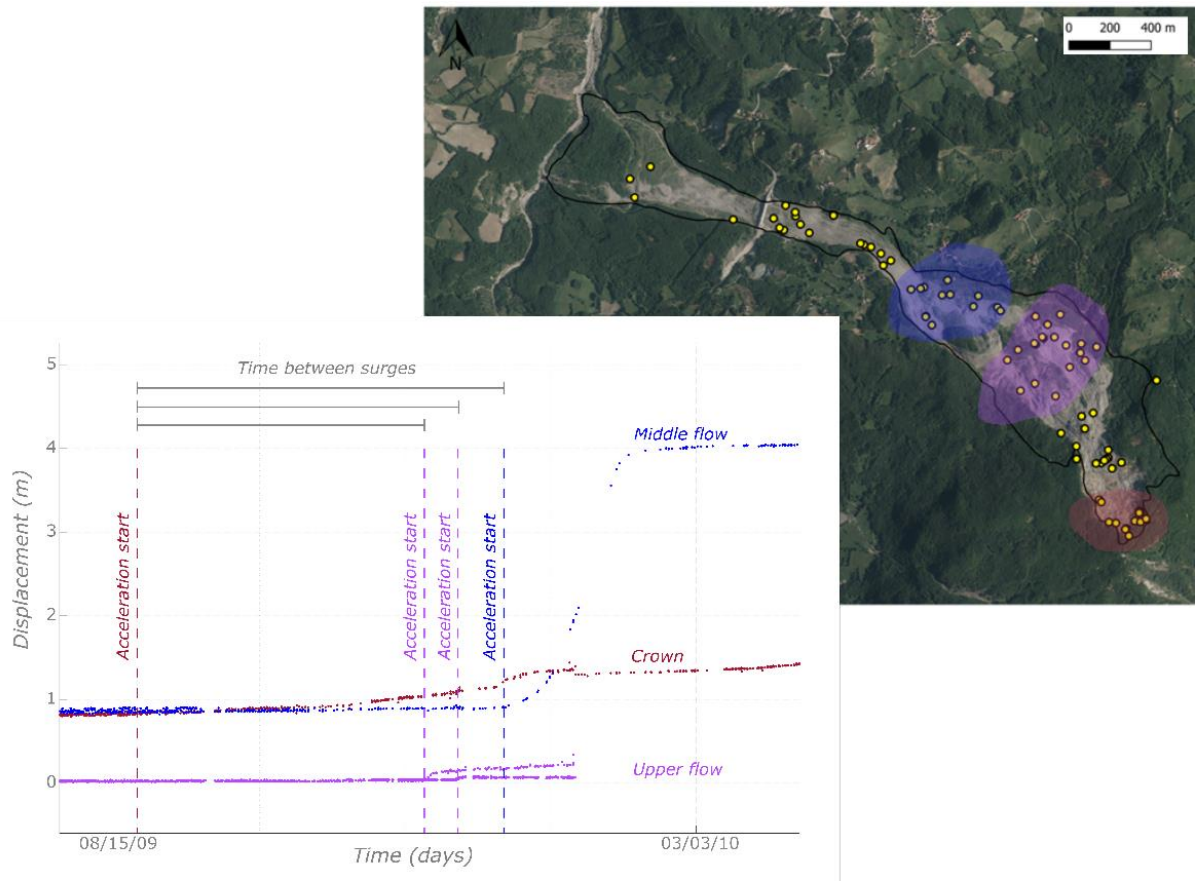

Figure 5.9: Propagation of the "acceleration information" scheme. On the top right the orthophoto of the Valoria earthflow (Reggio-Emilia province, Italy), the landslide boundary and the positions of the targets; three areas are highlighted with the same colors of the diagram on the right: red for the crown area, purple for the upper flow, blue for the middle flow. On the bottom left an example of the displacement series for the November 2009 reactivation: the different colors indicate the different portions of the landslide to which the monitored targets belong. Here only a limited number of target displacements are shown, for exemplification purposes. The beginning of the acceleration for each target is marked by the dashed lines. The time between surges is the "activation time". The distance of the targets from the target which starts to accelerate first is the "activated point".

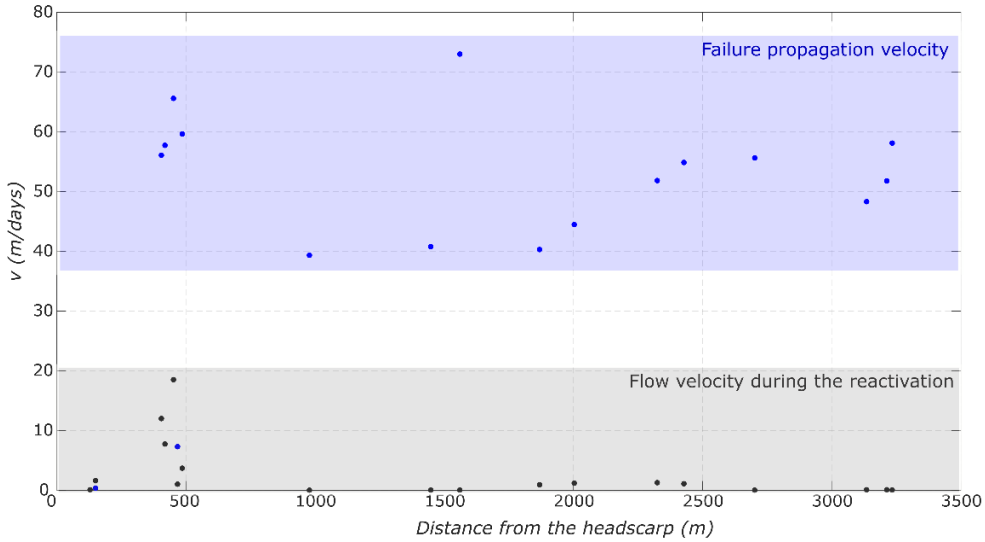

Figure 5.10: Velocity plot along the landslide profile. The greyish colors indicate the flow rate; the blueish colors indicate the propagation rate of the "acceleration information" (i.e. the propagation rate of the perturbation). This is an example referred to the October 2010 reactivation.

Using the same terminology as above, the time interval between the acceleration of consequent targets is the "activation time" and the targets are the "activated points". Hence, peaking the acceleration starts for each target (see Appendix A) we can investigate the propagation of perturbations process. Here the perturbation is the acceleration of the targets and the first perturbation occurring is the first measured acceleration. The target distance from the headscarp can be plotted against the time in which the target starts to accelerate: $t = 0$ is the time of the first measured acceleration. The result is an "activated point" – "activation time" plot like the one derived from the Iverson theory (Figure 5.11). This chart shows how the perturbation propagates downslope reaching the different portions of the slope. Referring to the November 2009 reactivation, 16 days are necessary for propagating of the perturbation to the toe. In the October 2010 reactivation, the propagation process is slower and perturbation reaches the toe in about 60 days. The differences can be related to many factors as changing in mechanical and viscous properties of the materials.

The obtained data can be fitted by using the Iverson model (Iverson 1986b). The modeling curves are derived as described in the previous sub-section. A range of realistic assumed values of density, cohesion, friction angle, slope angle and landslide thickness, has been tested for fitting purposes. We know that both the cohesion and water table depth should be equal to zero in such reactivation events (see above sub-section), but we need to account for a contribution of one of them, even very low, to fit the data properly. That means that soon after the reactivation not all the mass is fluidized. The fitting results are shown in Figure 5.12.

Again, it should be emphasized that proper landslide behavior modeling is beyond our intention. We want to highlight how the knowledge of some parameters plays a key role in the earthflow process understanding. If we are able to measure the parameters, Iverson theory can easily be used to explain entirely the earthflow evolution, both in reactivation stages and in the dormant ones.

The analyses above show that a full comprehension of earthflow dynamic is possible if a comprenshive set of suitable data can be gathered during a reactivation event. Of course this is extremely difficult to achieve because the onset of a reactivation is essentially unpredictable. Therefore, the main problem is a technical one: since we don't know when and where a new landslide process can take place we cannot document the process.

The need for a complete dataset arises. We tried to answer to that requirement by exploiting techniques capable to provide displacements data over very large regions so that a powerful monitoring method can be applied to know in advance something about the landslide-prone areas. Remote sensing is a quite spread approach for displacements surveys and can be applied over large regions without too high expenses. The main advantage relays on the ability to detect the position of ground points without installing specific devices in the areas of interest. Thus, it can be used over wide areas providing data immediately available. In particular, the InSAR technique has been widely tested for displacement monitoring in large areas (e.g. Colesanti et al., 2003; Hilley et al., 2004; Wasowski and Bovenga, 2014; Handwerger et al., 2015; Bayer et al., 2018). Several InSAR (synthetic aperture radar interferometry) algorithms for landslide detection have been proposed in literature (e.g. Ferretti et al., 2001; Berardino et al., 2002; Hooper et al., 2004; Hooper, 2008; Ferretti et al., 2011). The main limitation of these techniques is related to the displacements rates they are able to detect (Colesanti and Wasowski, 2006; Wasowski and Bovenga, 2014). We chose to apply conventional two-pass interferometry to Sentinel 1A/B radar data and follow the approach proposed by Handwerger and colleagues (Handwerger et al., 2015)

to investigate two earthflows of our region. The results of this test have been reported and commented in the next Chapter (Paper 3).

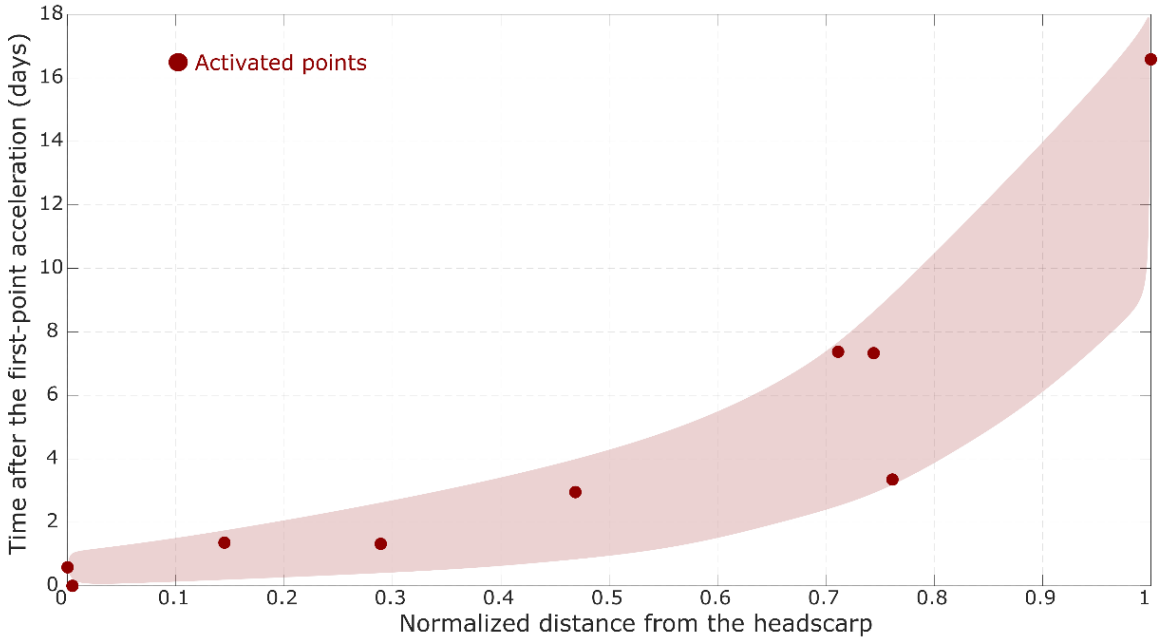

Figure 5.11: "Activated points"-"activation time" plot for the October 2010 reactivation: the "activated points" are the positions of the targets, here normalized by the total distance between the first and the last moving targets; on the y-axis the time after the acceleration of the first moving targets (i.e. "activation time").

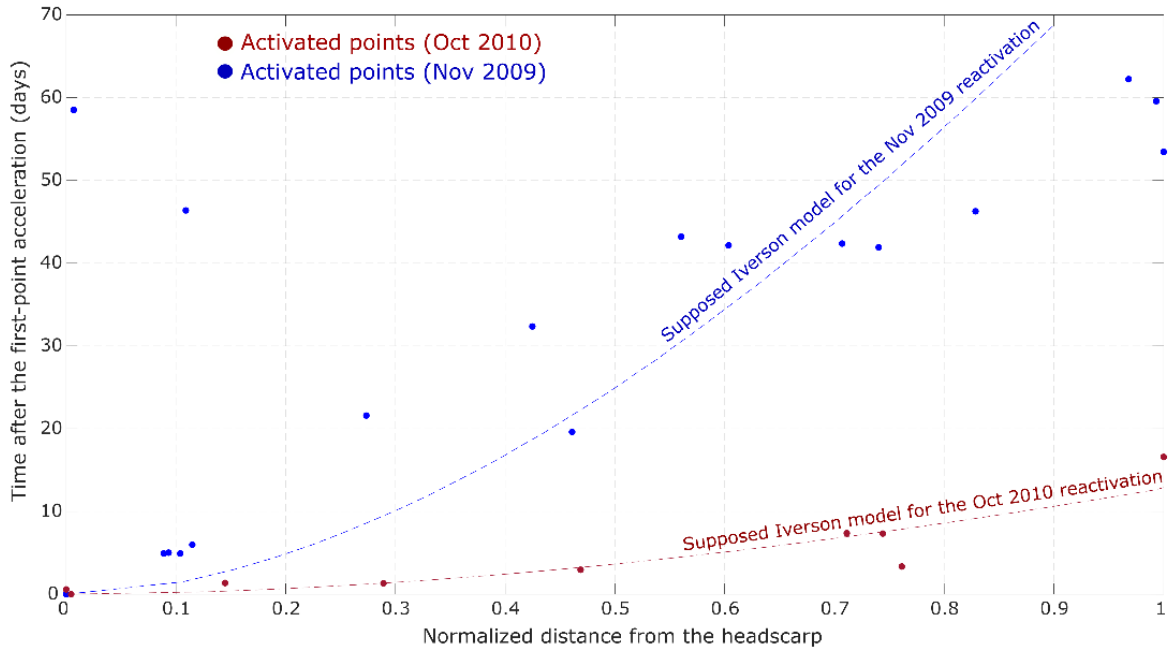

Figure 5.12: The "activation points"-"activation time" plot for the two reactivation events and derived fitting curves: the curves are obtained from the Iverson model (Iverson 1986b) by using the flow rate measured on the earthflow surface and assuming realistic values of the soil properties.

References

Ancey, C. (2007). Plasticity and geophysical flows: a review. *Journal of non-Newtonian fluid mechanics*, *142*(1-3), 4-35.

Angeli, M. G., Gasparetto, P., Menotti, R. M., Pasuto, A., & Silvano, S. (1996). A visco-plastic model for slope analysis applied to a mudslide in Cortina d'Ampezzo, Italy. *Quarterly Journal of Engineering Geology and Hydrogeology*, *29*(3), 233-240.

Bayer, B., Simoni, A., Mulas, M., Corsini, A., Schmidt, D. (2018). Deformation responses of slow moving landslides to seasonal rainfall in the northern apennines, measured by insar. *Geomorphology 308*, 293-306.

Bertello, L., Berti, M., Castellaro, S., & Squarzoni, G. (2018). Dynamics of an active earthflow inferred from surface wave monitoring. *Journal of Geophysical Research: Earth Surface*, *123*(8), 1811-1834.

Berti, M., Bertello, L., & Squarzoni, G. (2019). Surface-wave velocity measurements of shear stiffness of moving earthflows. *Landslides*, *16*(3), 469-484.

Bertolini, G., & Pellegrini, M. (2001). The landslides of the Emilia Apennines (Northern Italy) with reference to those which resumed activity in the 1994–1999 period and required civil protection interventions. *Quad. Geol. Appl*, *8*(1), 27-74.

Bird, R. B., Stewart, W. E., & Lightfoot, E. N. (1960). Transport Phenomena. New York. John willey & sons, 780 p.

Brunsden, D. (1999). Some geomorphological considerations for the future development of landslide models. *Geomorphology*, *30*(1-2), 13-24.

Cruden, D. M., & Varnes, D. J. (1996). Landslides: investigation and mitigation. Chapter 3-Landslide types and processes. *Transportation research board special report*, (247).

Colesanti, C., Ferretti, A., Prati, C., Rocca, F. (2003). Monitoring landslides and tectonic motions with the permanent scatterers technique. Engineering geology 68 (1-2), 3-14.

Desai, C. S., Samtani, N. C., & Vulliet, L. (1995). Constitutive modeling and analysis of creeping slopes. *Journal of geotechnical engineering*, *121*(1), 43-56.

Ferretti, A., Prati, C., & Rocca, F. (2001). Permanent scatterers in SAR interferometry. *IEEE Transactions on geoscience and remote sensing*, *39*(1), 8-20.

Ferretti, A., Fumagalli, A., Novali, F., Prati, C., Rocca, F., & Rucci, A. (2011). A new algorithm for processing interferometric data-stacks: SqueeSAR. *IEEE Transactions on Geoscience and Remote Sensing*, *49*(9), 3460-3470.

Handwerger, A. L., Roering, J. J., Schmidt, D. A., Rempel, A. W. (2015). Kinematics of earthflows in the northern california coast ranges using satellite interferometry. Geomorphology 246, 321-333.

Hilley, G. E., Burgmann, R., Ferretti, A., Novali, F., Rocca, F. (2004). Dynamics of slow-moving landslides from permanent scatterer analysis. Science 304 (5679), 1952-1955.

Hooper, A., Zebker, H., Segall, P., & Kampes, B. (2004). A new method for measuring deformation on volcanoes and other natural terrains using InSAR persistent scatterers. *Geophysical research letters*, *31*(23).

Hooper, A. (2008). A multi-temporal InSAR method incorporating both persistent scatterer and small baseline approaches. *Geophysical Research Letters*, *35*(16).

Iverson, R. M. (1985). A constitutive equation for mass-movement behavior. *The Journal of Geology*, *93*(2), 143-160.

Iverson, R. M. (1986a). Unsteady, nonuniform landslide motion: 1. Theoretical dynamics and the steady datum state. *The Journal of Geology*, *94*(1), 1-15.

Iverson, R. M. (1986b). Unsteady, nonuniform landslide motion: 2. Linearized theory and the kinematics of transient response. *The Journal of Geology*, *94*(3), 349-364.

Keefer, D. K., & Johnson, A. M. (1983). Earth flows; morphology, mobilization, and movement. *U.S. Geol. Surv. Prof. Pap*, 1264-56 pp.

Malvern, L. E. (1969). *Introduction to the Mechanics of a Continuous Medium.* Englewood Cliffs, N.J.,Prentice-Hall, 713 p.

Picarelli, L., Russo, C., & Urciuoli, G. (1995). Modelling earthflow movement based on experiences. In *11 European Conference on Soil Mechanics and Foundation Engineering* (Vol. 6, pp. 157-162). Danish Geotechnical Society.

Picarelli, L. (2000). Mechanisms and rates of slope movements in fine grained soils. In *ISRM International Symposium*. International Society for Rock Mechanics and Rock Engineering.

Savage, W. Z., & Chleborad, A. F. (1982). A model for creeping flow in landslides. *Bulletin of the Association of Engineering Geologists*, *19*(4), 333-338.

Skempton, A. W. (1985). Residual strength of clays in landslides, folded strata and the laboratory. *Geotechnique*, *35*(1), 3-18.

Thielicke, W. (2014). *The flapping flight of birds: Analysis and application*. University of Groningen.

Thielicke, W., & Stamhuis, E. (2014). PIVlab–towards user-friendly, affordable and accurate digital particle image velocimetry in MATLAB. *Journal of Open Research Software*, *2*(1).

Van Asch, T. W., Van Beek, L. P. H., & Bogaard, T. A. (2007). Problems in predicting the mobility of slow-moving landslides. *Engineering geology*, *91*(1), 46-55.

Wasowski, J., Bovenga, F. (2014). Investigating landslides and unstable slopes with satellite multi temporal interferometry: Current issues and future perspectives. Engineering Geology 174, 103-138.

Zhang, X., Phillips, C., & Pearce, A. (1991). Surface movement in an earthflow complex, Raukumara Peninsula, New Zealand. *Geomorphology*, *4*(3-4), 261-272.

6. PAPER 3

Pre and post failure behaviour of landslides in the Northern Apennines revealed by space-borne synthetic aperture radar interferometry (InSAR)*

Squarzoni G., Bayer B., Franceschini S., Berti M., Simoni A.

*Submitted to **Geomorphology**

Pre and post failure behaviour of landslides in the Northern Apennines revealed by space-borne synthetic aperture radar interferometry (InSAR)

Squarzoni, Gabriela[a], Bayer, Benedikt[b], Franceschini, Silvia[b], Berti, Matteo[a], Simoni, Alessandro[a,*]

[a] *Via Zamboni 67, Bologna, University of Bologna*
[b] *Viale Fanin 48, Bologna, Fragile srl*

Abstract

Landslides are common landscape features in the Northern Apennine mountain chain and cause frequently damages to manmade structures and infrastructure. Most landslides in the area can be classified as earthflows, where the clay-shales form the substrate, whereas complex landslides with flow and sliding components are common on the slopes where fine-grained turbidites form the substrate. Most of these landslides move periodically with contained velocities and only after particular rainfall events some of them accelerate abruptly. Space-borne synthetic aperture radar interferometry (InSAR) provides a particularly convenient way for studying the periods before and after failures. In this paper, we present InSAR-results derived from the Sentinel 1 satellite constellation for two landslide cases in the Northern Apennines. The first case is a complex landslide that is hosted on a pelitic flysch formation, while the second case is an earthflow located in chaotic clay shales. Both cases failed catastrophically and threatened or damaged important infrastructures. In case of the complex landslide, we report spatially variations of the deformation field between repeated periods of acceleration. The data illustrate that the deformation initiated in the upper part of the slope and expanded over the whole landslide body afterward. In case of the earthflow, we describe both spatial and temporal kinematics during the period before a catastrophic failure in March 2018. We discuss the temporal deformation signal together with rainfall and snowmelt data from a nearby meteorological station. Deformation and precipitation data highlight that high total precipitation can be considered the trigger of the failure.

Keywords: `InSAR`, `landslides`, `earthflows`, `failure`, `rainfall`, `snowmelt`

1. Introduction

Landslides are common morphological features throughout the whole Northern Apennines chain. Most slope deformations occur on old landslide bodies that failed in the past (Bertolini et al., 2004). In many cases, the reactivation of old deposits causes the regression of the main scarp and the physical degradation of the material which may move downwards as an earthflow. In other cases, the reactivation is more complex and different types of landslides can occur (Bertolini and Pellegrini, 2001). Since the typical velocity of most of these landslides can span from centimeters per year to meters per hour depending on the stage of their life (Cruden and Varnes, 1996), it becomes important to properly monitoring the displacements of the involved masses in order to assess the possibility of sudden accelerations.

A powerful technique for the displacements monitoring of large areas is the synthetic aperture radar interferometry (InSAR) that provides the possibility to measure the deformations of the landslide deposits during the slow-motion stage (i.e., before the rapid acceleration). InSAR was applied in a landslide-prone area already in the mid-1990s (Fruneau et al., 1996), but only starting from the 2000s it became a well-known technique for landslide monitoring. The development of multi-temporal methods (e.g. Ferretti et al., 2001; Berardino et al., 2002; Hooper et al., 2004; Hooper, 2008) helped in many cases to obtain useful InSAR derived displacement information on landslides. Those techniques have been developed to overcome some of the limitations that conventional two-pass interferometry had shown until that time (Colesanti and Wasowski, 2006; Wasowski and Bovenga, 2014). Since then, different InSAR techniques have been used to retrieve spatial and temporal deformations of landslide-prone slopes in soft rocks (Colesanti et al., 2003; Hilley et al., 2004; Wasowski and Bovenga, 2014; Handwerger et al., 2015; Bayer et al., 2017, 2018).

The two most common multi-temporal techniques are the Persistent Scatterer interferometry (PS-InSAR, Ferretti et al., 2001) and Small Baseline techniques (SBAS, Berardino et al., 2002, Schmidt and Bürgmann, 2003): the former is based on the stable SAR response of specific targets (i.e. stable scatters), computed by using single-master interferograms series; the latter is often optimized to derive spatially distributed information of multi-master interferograms series. Other techniques combine the advantages of both techniques (Hooper, 2008).

*Corresponding author
Email address: alessandro.simoni@unibo.it (Simoni, Alessandro)
URL: www.fragilesrl.it (Bayer, Benedikt), www.fragilesrl.it (Franceschini, Silvia)

PS-InSAR and small baseline techniques are widely used for landslide studies (Bianchini et al., 2013; Tofani et al., 2013; Wasowski and Bovenga, 2014; Raspini et al., 2019), but in mountainous areas the quality of measurements is often affected by decorrelation due to the environmental setting and in particular the presence of snow during the winter months and vegetation in the rest of the year. In such contexts, stable scatters detection is constrained to man-made structures which are characterized by high coherence values. Thus, decorrelation issues are still challenging in scarce-urbanized areas.

In the past, only L-band data delivered spatially quasi-continuous data in settings similar to the northern Apennines. However, the few reported examples resolve mainly the seasonal kinematics of slow-moving landslides in California (Roering et al., 2009; Handwerger et al., 2013). The launch of the new Sentinel 1 satellite constellation, which is characterized by a high acquisition frequency of up to six days, is suited to reduce decorrelation in the derived interferograms (Intrieri et al., 2018; Carlà et al., 2018) and permits to obtain promising results with higher temporal resolution (Handwerger et al., 2019).

In this paper, we investigate the behavior of two landslides using InSAR analysis. Due to the fact that our landslides are located in rural areas with scarce urbanization, we use standard InSAR and explore its potential in capturing the changeable displacement rates and spatial patterns of deformation. During the time span of our investigation, both landslides experienced catastrophic failures (here defined as stage A of the morphological classification reported in Picarelli et al. (2005); failure in the following).

We show that the technique is capable of detecting spatially quasi-continuous deformation maps, also in areas that are characterized by the absence of good quality reflectors. Our data indicate that, in both cases, the failure was preceded by detectable deformation. InSAR results document the pre-failure and post-failure stages of the movement both in terms of its spatial pattern and temporal evolution. In one of the two cases, we could derive actual displacement time-series that were compared to the precipitation regime to identify the triggering condition.

2. Geological and geographical background

The northern Apennine mountain chain is a pile of thrust and nappe units, transported towards the Padan-Adriatic-Ionian-Hyblean foreland starting from Late Oligocene times. In the Northern

Apennines, the most common lithologies are chaotic clay shales and flysch deposits (Royden et al., 1987; Castellarin, 1992; Patacca et al., 1993; Marroni and Treves, 1998).

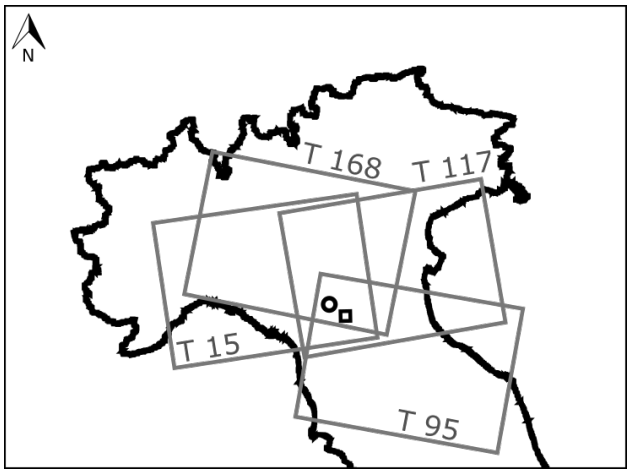

Figure 1: Location of the investigated landslide and setting of the satellite Tracks over the area. The square indicates the Marano landslide; the indicates the Ca Lita landslide.

The northern Apennines are affected by a high landslide density and over the region of Emila Romagna Bertolini and Pellegrini (2001) reported more than 32000 landslide bodies. In the classification scheme of Cruden and Varnes (1996), most of them can be described as complex landslides, associating roto-transitional slides with earthflows. Typical velocities are millimeters to centimeters per year during the dormant phase (which may last years to hundreds of years) and may increase up to meters per hour during the failure. The failure stages typically occur after periods of heavy rainfall. The average annual rainfall at elevations similar to those of the two case studies is around 1200 mm, but the pluviometric regime is not uniform and 75% of the total rainfalls occurs in two rainfall seasons one of which occurs during fall and one during spring (Bertolini and Pellegrini, 2001; Berti and Simoni, 2012; Berti et al., 2012). The investigated cases are located in the Northern Apennines of Italy and both of them are covered by four Sentinel satellite orbits, two of which imaged the area in ascending geometry, while the other two swaths cover in descending geometry (Fig 1). The landslides reached the failure in the period covered by Sentinel 1 flights. Marano reactivated in March 2018 and Ca Lita in March 2016 and November 2017.

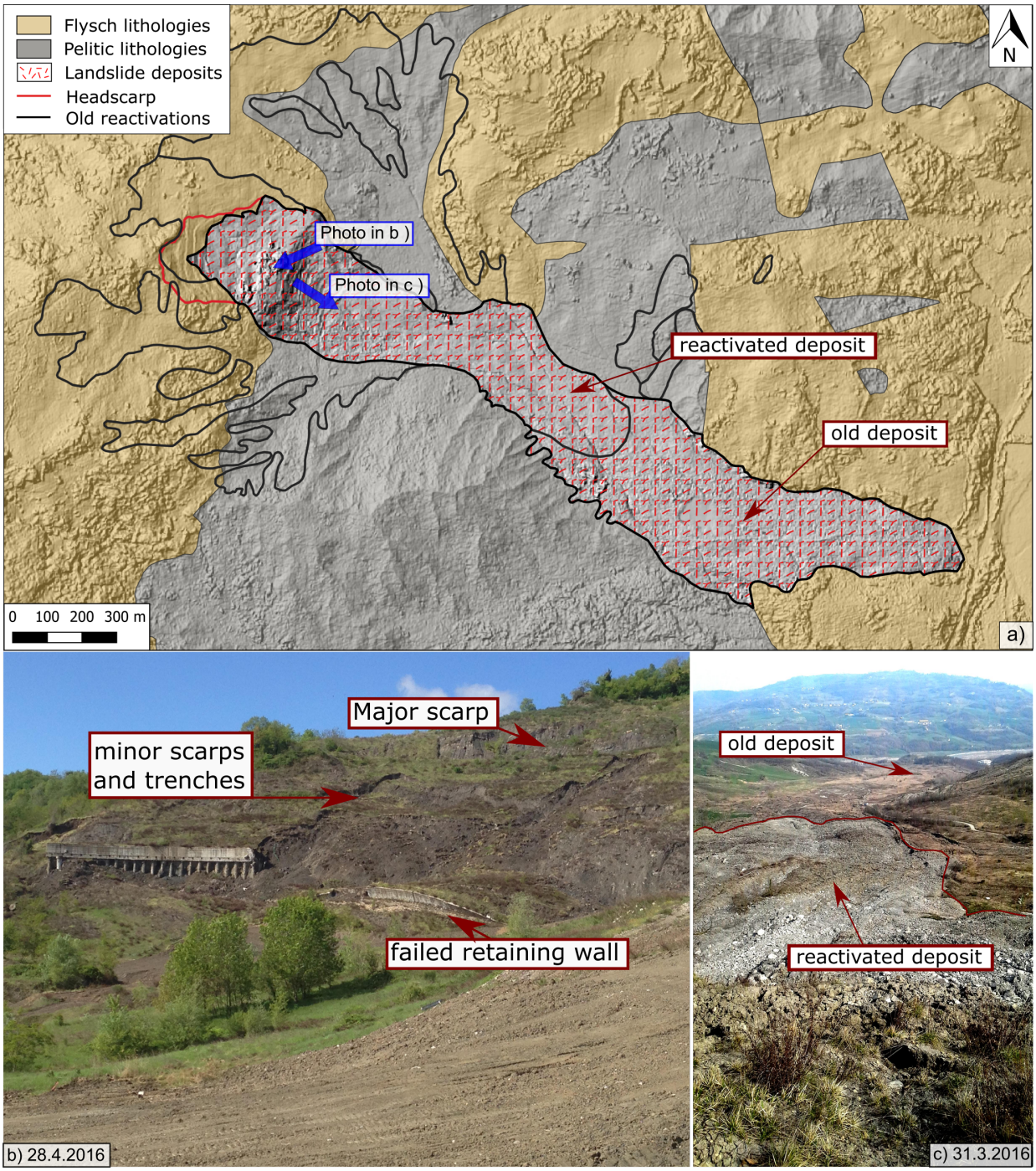

Figure 2: a) Map of the Ca Lita landslide with positions of the photos that were taken after the reactivation during March 2016. They show c) the rotational sliding in the upper part that caused the failure of the mitagation measurements (photo courtesy of Al Handwerger) and b) the flow like propagartion in the lower part of the slope.

2.1. The Ca Lita landslide

The Ca Lita landslide (Fig. 1, 2 a) develops along a hillslope composed of flysch and clay-shales belonging to the Ligurian Units (Papani et al., 2002). It is located between 230 and 640 m a.s.l. in the Reggio Emilia province (Italy); the total length is 2.7 km, with a mean slope angle of 15 degrees and a total estimated volume of 40 Mm^3. The landslide can be classified as a reactivated complex landslide (Cruden and Varnes, 1996), in which a rotational rock slide in the head zones (in the Monghidoro Flysch Formation) evolves into an earthflow in the lower main body (in the Rio Cargnone Clayshales). It reactivated several times in the last century (Borgatti et al., 2006; Corsini et al., 2006; Cervi et al., 2012).

One catastrophic failure occurred in early spring 2004 after an intense rainy and snowy period. During this reactivation, it reached peak velocities of about 10 m per day at the toe and only of few decimeters per day in the upper part (Borgatti et al., 2006; Corsini et al., 2006). After the reactivation, mitigation structures as drainage systems and retaining walls were built in order to stabilize the landslide. Since then, no further deep-seated movements have occurred (Cervi et al., 2012) until march 14th, 2016. During this reactivation the flysch rocks belonging to the upper part failed and deformed in a roto-translational movement causing the failure of a retaining wall (Fig. 2 b) and the mobilization of the landslide deposit in the lower part as a flow-like movement (Fig. 2 c). The photos show that the deformation varied from several meters in the upper part up to hundreds of meters in the lower part. The landslide mass slowed down towards the end of March 2016.

In the middle of November 2017, it accelerated again: the upper earthflow deposits partially reactivated and moved downslope. The first movements occurred in correspondence in the upper part of the earthflow deposit with estimated displacements of several meters. The intensity of the displacements gradually decreased in the lower portion. The earthflow velocity never reached zero value: on February 20th, 2018 it has been affected by another small acceleration and in March 2018 changing geomorphological features like trenches, exposed material, and surface water ponds demonstrated that it kept moving (Servizio Geologico Sismico e dei Suoli della Regione Emilia-Romagna, 2019).

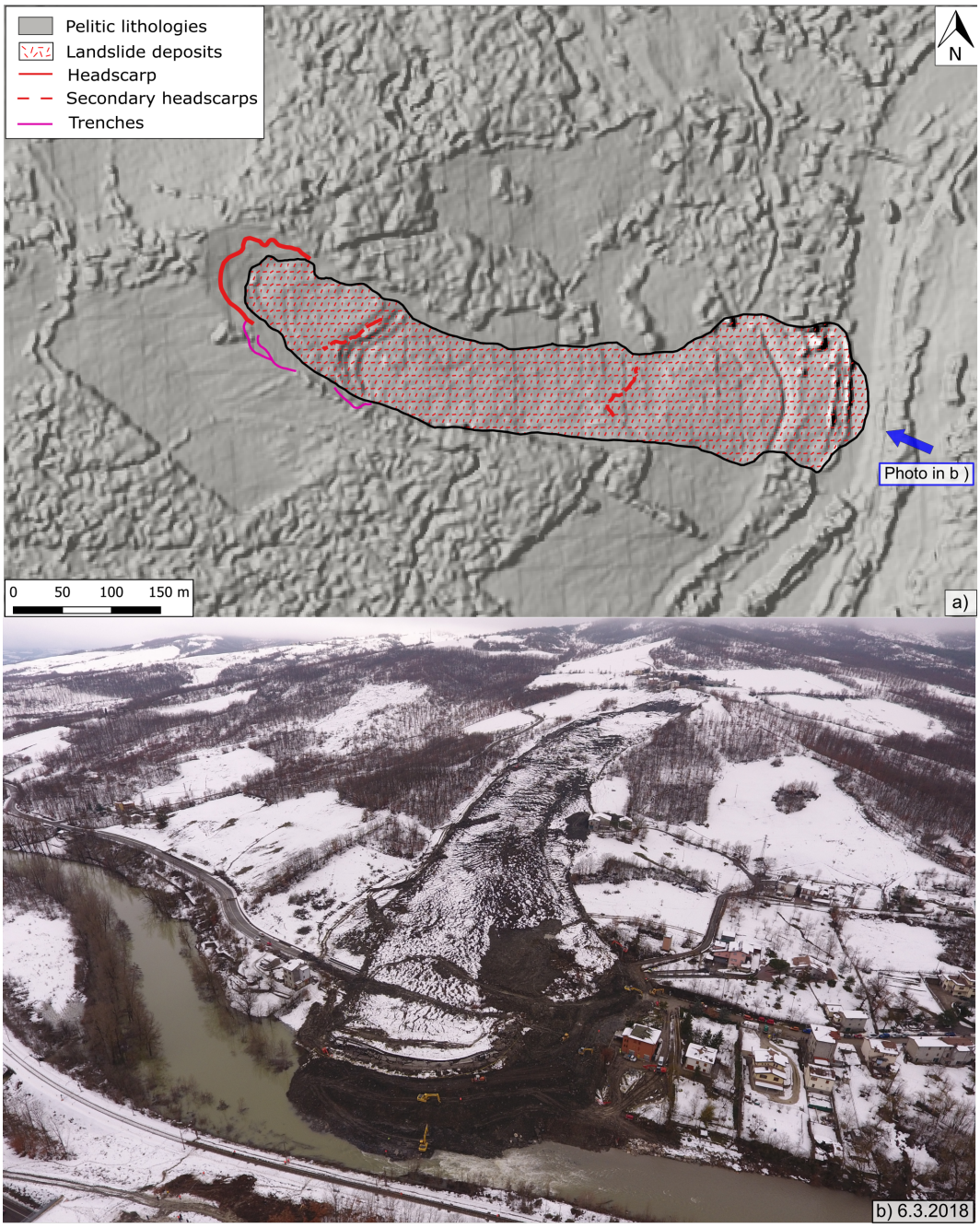

Figure 3: a) Map of the Marano earthflow with the deposits and the main morphological features related to the last reactivation being highlighted. b) Foto taken by a drone on the 6th of March 2018 (photo courtesy of Davide Marchioni).

2.2. The Marano earthflow

The Marano landslide (Fig. 1, 3) is located in the Bologna province (Italy) between 260 and 400 m a.s.l.; it is 700 m long and 100 m large for an estimated total volume of about 0.5 Mm^3. The

landslide is a reactivated earthflow (Cruden and Varnes, 1996) that involve clay-shale lithologies belonging to the Palombini Shale Formation (Panini et al., 2002). During the last century, it reactivated twice: February 1996 and March 2018.

The 1996 event occurred after a period of intense rainfalls and snowfalls. The first motion had been recorded on February 1st in the upper portion of the slope and rapidly propagated downslope; after 6 days of rapid movement, it slowed down. The slope failure interested different infrastructures like roads, methane pipelines, phone and electricity lines (Servizio Geologico Sismico e dei Suoli della Regione Emilia-Romagna, 2019). In the following period, mitigation strategies were adopted including drainage systems in the earthflow deposits and gabions in the lower part of the landslide to preserve the road below.

For more than 20 years no signs of deformation were observed on the rebuilt road, in the gabions or the earthflow area. However, on March 1st, 2018 the landslide accelerated after a period of snowmelt and rainfall. The mitigation structures were destroyed and the deposits reached the Reno river which is well visible in Fig 3 b. The Marano landslide moved with velocities of several meters per day for at least ten days, then decelerated. In the following days, employees worked at the earthflow toe and removed a large amount of material that was occluding the Reno river threatening also the railways on the opposite bank.

3. Material and methods

Space-borne synthetic aperture radar interferometry (InSAR) is a remote sensing technique that exploits the phase difference between two radar images that were acquired over a given track of the earth surface by a satellite. Part of the phase difference is caused by the deformation of the targets inside a pixel with respect to the sensor (Massonnet and Feigl, 1998; Rosen et al., 2000; Bürgmann et al., 2000).

Since the interferometric phase is not entirely caused by deformations, some terms need to be removed in order to measure only the amount of phase due to the displacements. If deformation measurement is the goal, the main sources of the undesired signal are the differential phase due to topography, atmosphere and orbital errors (Tarayre and Massonnet, 1996; Zebker et al., 1997; Fattahi and Amelung, 2015). In addition to that, the decorrelation occurs if the time span between the acquisition becomes long or if the perpendicular baseline between two acquisitions is large

(Zebker and Villasenor, 1992).

Multitemporal techniques like persistent scatterers interferometry (Ferretti et al., 2001; Hooper et al., 2004), evolutions of it (Ferretti et al., 2011), small baseline techniques (Berardino et al., 2002; Schmidt and Bürgmann, 2003) or hybrid approaches (Hooper, 2008) were frequently used in the past to infer spatiotemporal information of slope deformations both on the scale of single slopes (Wasowski and Bovenga, 2014), as well as on larger scales. Near to the study area, small baseline techniques proved useful to obtain assess tunneling induced deformation (Bayer et al., 2017), but also the relationship between seasonal creep of landslides due to variations of precipitation (Bayer et al., 2018). All of the aforementioned works used techniques that focussed on extracting highly coherent pixels mostly on manmade structures, like houses or exposed rock-outcrops. In the study area, however, most active landslides have a moderate vegetation cover, rarely have exposed landslide material and only slow-moving deep-seated landslides have man-made structures on them.

Similar geomorphological and geological conditions exist in Northern California, where until now only long-wavelength data from ALOS permitted to reveal relationships between earthflow deformation and the precipitation regime (Handwerger et al., 2013, 2015; Bennett et al., 2016), and in combination with offset tracking techniques also the slow down of earthflows due to extreme drought conditions. Most recently however Handwerger et al. (2019) have shown that also the C-band data acquired by Sentinel 1 can be successfully used to obtain high-quality interferograms on landslide types similar to the ones described in this paper.

We performed interferometric processing of synthetic aperture radar images acquired by Copernicus Sentinel 1 A/B satellites by using GMTSAR (Sandwell et al., 2011) and unwrapped the complex interferograms with the Statistical-Cost, Network-Flow Algorithm (SNAPHU; Chen and Zebker, 2001). The Sentinel images are C-band images (5.6 cm radar wavelength) acquired with a minimum interval of acquisition of 6 days (12 days for each satellite, with a 6 days interval between Sentinel 1A and Sentinel 1B). We studied the period between January 2015 and January 2019 by analyzing 2 descending orbits (south-moving satellites, looking west) and 2 ascending orbits (north-moving satellites, looking east) for a total of 4 datasets for each landslide: Track 168, Track 95, Track 15 and Track 117 (Fig. 1). We initially processed a total of 869 interferograms for the Marano landslide and 1419 interferograms for the Ca Lita landslide that were inspected visually

and only interferograms with a clear phase signal were considered for further processing.

The topographic phase was calculated and subtracted (e.g. Massonnet and Feigl, 1998; Bürgmann et al., 2000) by using an external digital surface model (2x2 m DSM, provided by the Emilia Romagna Region Services). Due to the small perpendicular baselines of Sentinel 1, the residual DEM error is small compared to the signal due to landslide motion and a correction scheme like the one proposed in (Fattahi and Amelung, 2015) proved not necessary. The atmospheric noise has been reduced by selecting a stable reference area close to the deforming region: we chose geomorphological (e.g. ridges) or anthropic (e.g. stable buildings) features located near to the landslides. Moreover, Gaussian and Goldstein filters (Goldstein and Werner, 1998) have been applied after the interferograms formation to reduce the noises and enhance the deformation signal.

In order to overcome decorrelation and unwrapping problems due to fast-displacement, we used a scalable model-approach similar to the one proposed by Handwerger et al. (2015, 2019). The model has been computed using the following scheme: (i) we formed the model by stacking a set of well correlated interferograms that do not contain unwrapping errors, (ii) we scaled the model to obtain maximum displacements multiple of a π cycle and (iii) subtracted it from the wrapped interferograms that displayed unwrapping errors; then (iv) we unwrapped the residual interferograms using SNAPHU and (v) added the model back to the unwrapped residual interferograms.

This approach helped to unwrap phase-ambiguities over the Marano landslide, while at the Ca Lita landslide it helped only in few cases. This is probably because the Marano earthflow deformed in a coherent slab, while the Ca Lita landslide has complex sliding features in the upper part with high relative displacements and flow like deformation in the lower part with high absolute displacements.

After this manual and iterative process of inspecting and improving interferograms, only those without severe phase unwrapping problems were used to produce stacks of interferograms that contain mean velocities and, in case of the Marano landslide, velocity time series.

4. Results

4.1. Spatial deformation patterns on the Ca Lita landslide

The kinematics of the Ca Lita earthflow are characterized by repeated variations of the displacement rates with values that exceed the detection limits of spaceborne radar interferometry.

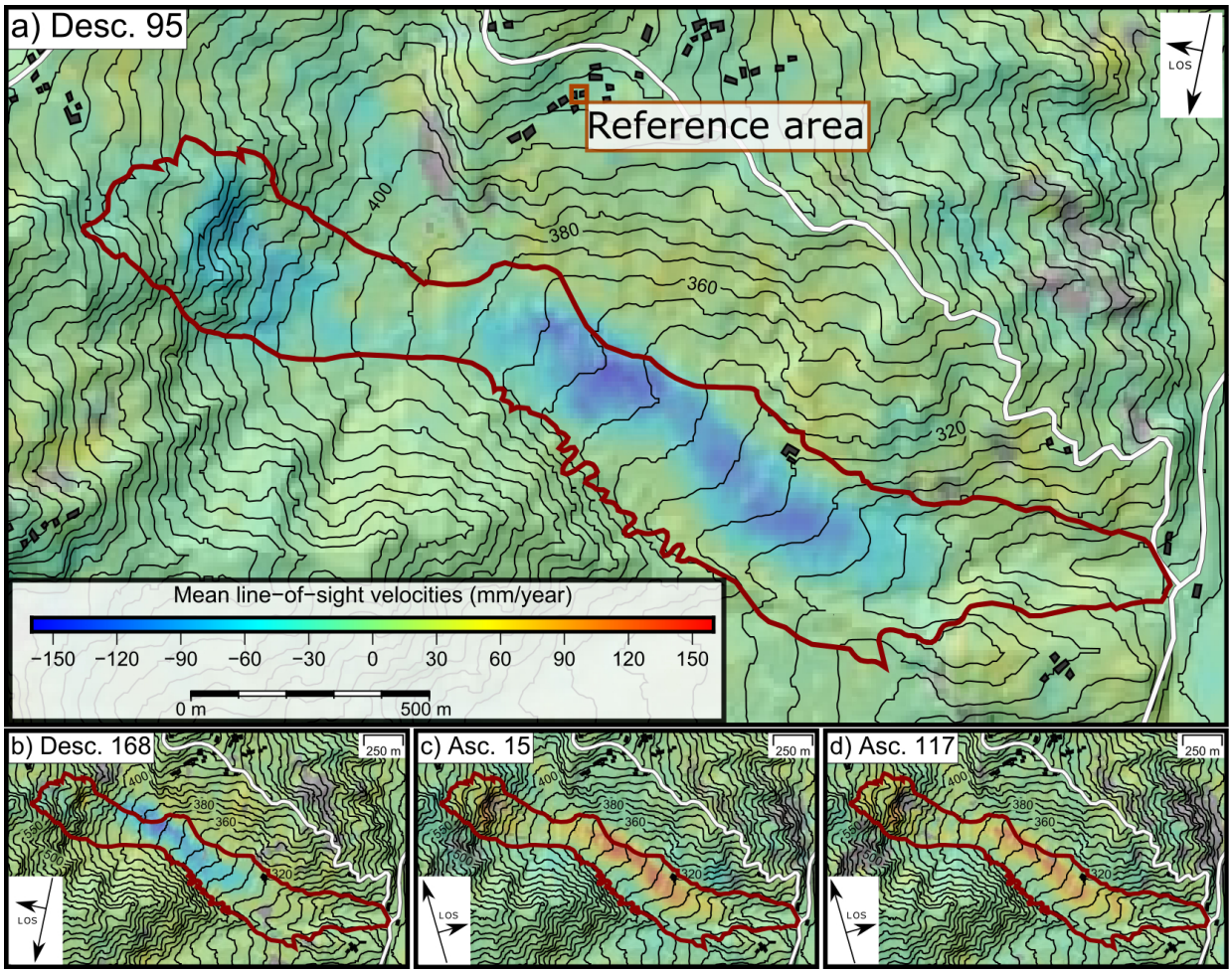

Figure 4: Ca Lita stacks of the entire interferograms series, concerning the period between January 2015 and January 2019: the numbers of the satellite Tracks are labeled at the top right of each image and the orbit directions are indicated at bottom right. Positive (red) values indicate motion away from the satellite along the line-of-sight and negative (blue) values indicate motion toward satellite along the line-of-sight. The numbers of interferograms that have been used to compute the stacks are: a) 286, b) 352, c) 372, d) 409.

Although at times it moves too fast to derive displacement or velocity time-series, a clear spatial deformation pattern roughly corresponding to the main landslide deposit can be detected in a large number of interferograms. Stacking series of interferograms corresponding to a given time-interval increases the signal-to-noise ratio and highlights deforming features. The analysis and comparison of successive interferometric stacks allow obtaining both spatial and temporal information about the landslide during phases of slow displacement rates. During the failure stages decorrelation and unwrapping problems due to fast-displacement can not be resolved, which is why the mean

velocities computed from the stacking process are locally underestimated. However, the spatial deformation signal is clear and can be used to document the evolution of the landslide movement just near the activation stages.

The stack of all manually-selected interferograms (from January 2015 to January 2019) highlights the long-shaped morphology of the Ca Lita earthflow, that corresponds to the landslide deposit of the prior reactivation (Borgatti et al., 2006; Corsini et al., 2006; Servizio Geologico Sismico e dei Suoli della Regione Emilia-Romagna, 2019). The interferometric signal is particularly clear in the descending orbit 95 (Fig.4 a), whose stack indicates a range decrease and hence a movement towards the satellite. This observation is confirmed by descending orbit 168 (Fig.4 b). while the ascending orbits (117 and Fig.4 c and d) both record range increases and hence movements away from the satellite. In all cases, we used a mean coherence threshold of 0.25 to mask out areas affected by low coherence. Due to the selection procedure of the interferograms, coherence is, however, higher than 0.25 in most interferograms, which is why very few areas are masked out.

The difference between the ascending and the descending geometries should be interpreted as a real deformation field that is oriented approximately down-slope. Maximum displacement rates are detected in the central part of the slope, where the type of movement transitions from sliding to flowing. The landslide toe is relatively stable (no interaction with the national road was reported) as well as the area above the crown where houses are located exhibit no deformation.

In order to document the temporal evolution of the Ca Lita landslide, we combined interferograms in bimonthly stacks. We found that such frequency was suitable to resolve the different deformation phases of this landslide. Fig. 8 reports the results derived from the descending orbit 168. The failure of March 2016 is not clearly documented by radar interferometry due to persisting snow cover in the area, which impeded to form coherent interferograms during this period. After failure the Ca Lita landslide exhibit enduring deformation: in the summer period the displacement signal that is oriented towards the satellite is less evident and is located mainly the central portion of the deposits (Fig.5 - a, b). In late fall of 2016 (Fig.5 b) and early 2017 (Fig.5 c) almost all the landslide deposit is actively deforming.

At the beginning of 2017, the displacements range decreases are mainly located in the central part of the slope where flow-like deformation is dominant and where the slope decreases (Fig.5 c). In the upper part, small range increases were registered by the interferograms that span this

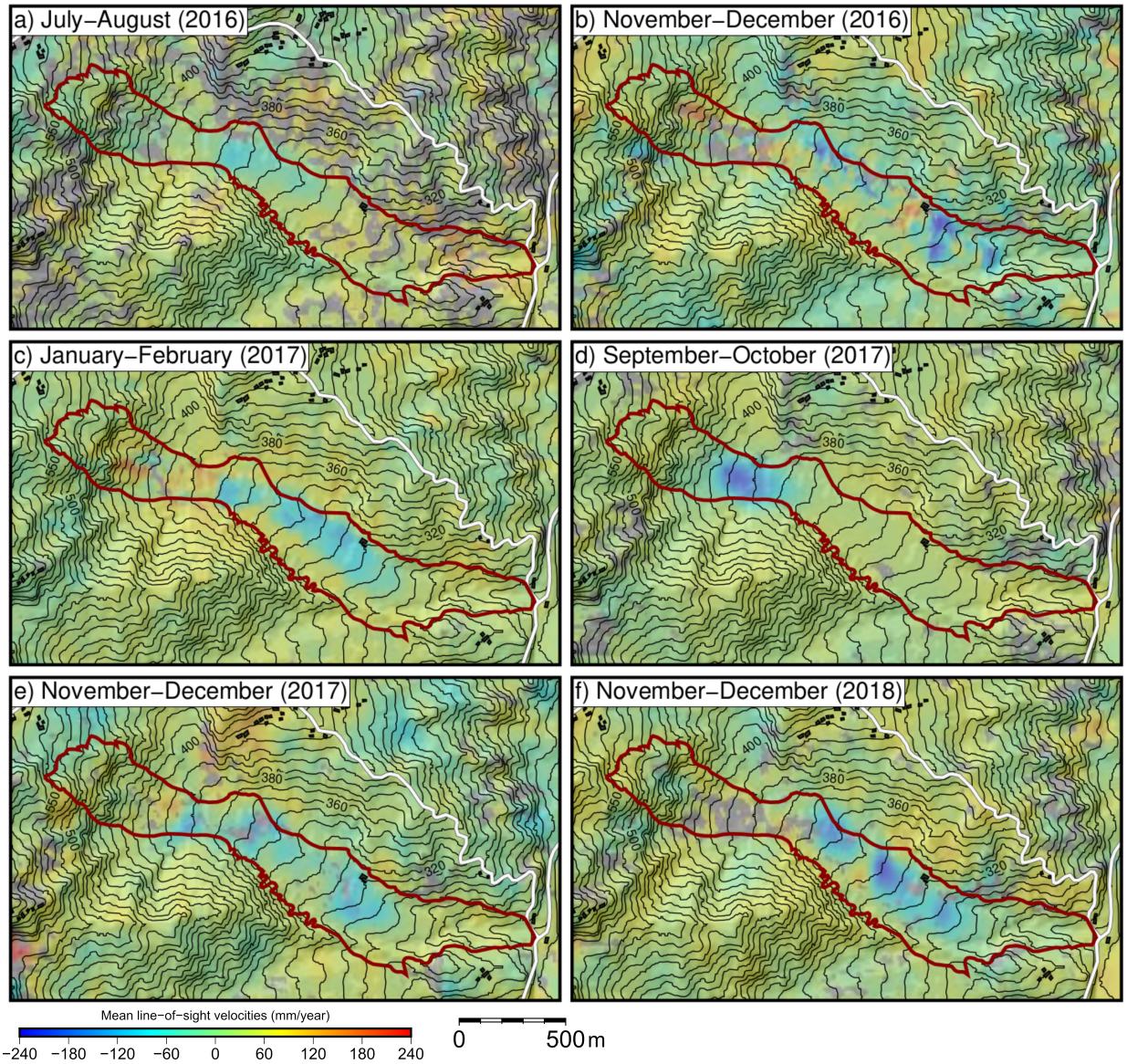

Figure 5: Two-months stacks for Track 168: a) July - August: 7 interferograms used for the stacking, b) November - December 2016: 10 interferograms used for the stacking, c) January - February 2017: 9 interferograms used for the stacking, d) September - October 2017: 8 interferograms used for the stacking, e) November - December 2017: 10 interferograms used for the stacking, f) November - December 2018: 10 interferograms used for the stacking. Three stages of movement can be observed: from a) to c) the deformation involves a very large portion of the deposits; in d) only the upper part in interested by displacements; from e) to f) the whole mass is involved again. Positive (red) values indicate motion away from the satellite along the line-of-sight and negative (blue) values indicate motion toward satellite along the line-of-sight; 0.2 coherence mask has been applied for results displaying

period. During the summer months the slope was relatively stable with LOS (Line-Of-Sight) displacement rates lower than 100 mm/month, but during September-October 2017 deformation is intense (> 150 mm/year) and localized in the upper part of the landslide (Fig.5 d) where the slope is relatively steep and sliding transition into flow-like type of movement. Following the failure of November 2017, the whole landslide body except for the toe continued to move (Fig.5 e) though displacement rates appear generally lower. In the following, the landslide activity is clearly visible in the interferograms throughout the duration of our analysis. The LOS velocities are locally sustained (> 150 mm/year), especially during the rainy season e.g., Nov.-Dec. 2018 stack in Fig.5 f).

4.2. Pre-failure kinematics of the Marano earthflow

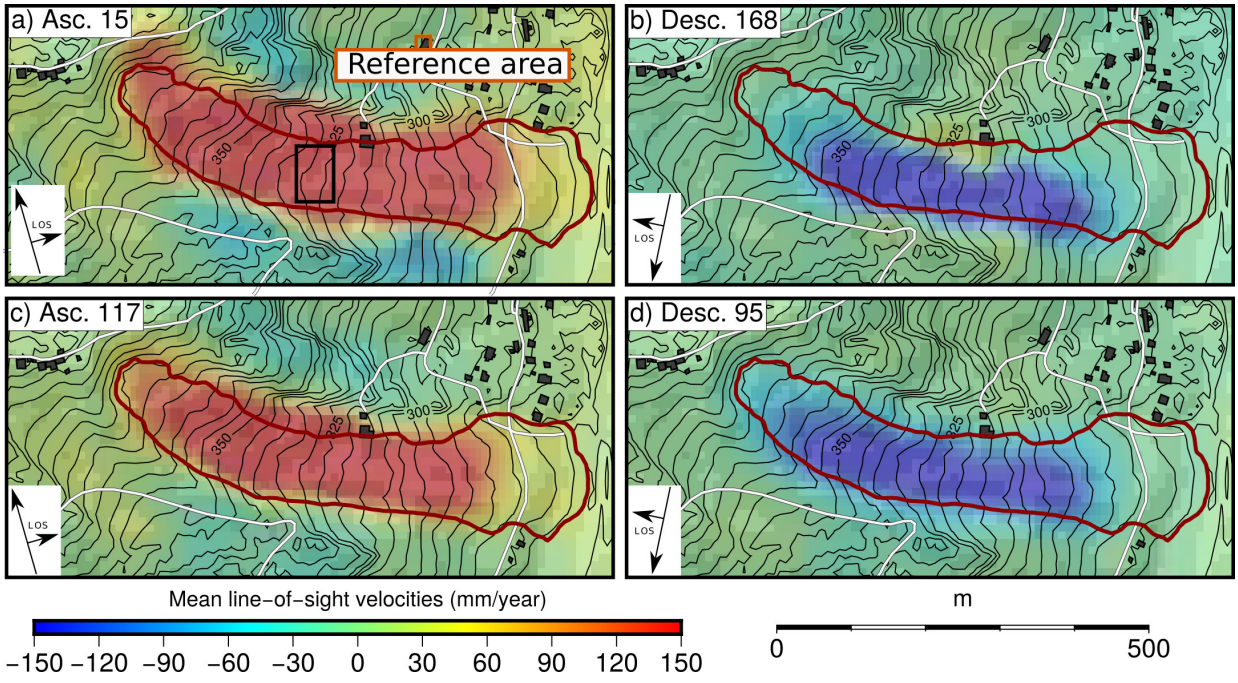

Figure 6: Marano stacks of the entire interferograms series, concerning the period between January 2015 and January 2019 derive from a) the ascending orbit 15 using 161 interferograms (the black box indicates the pixels that were used for the timeseries in figure 7, b) the descending orbit 168 using 218 interferograms c) the ascending orbit 117 using 209 interferograms and d) the descending orbit 95 with 281 interferograms. Warm colours indicate a movement away from the satellite along the line-of-sight, while cold colours indicate a movement towards the satellite.

The Marano earthflow reactivated catastrophically on March 1st, 2018 after 22 years of dormancy. The vast majority of selected interferograms (January 2015 to January 2019) detect ac-

tive deformation along the slope. The apparently dormant landslide has been interested in detectable deformation for at least two years before the catastrophic failure occurred. The stack of all manually-selected interferograms shows an extremely clear signal detected by all available orbits (Fig. 6). The reference area was chosen with respect to the houses of the locality Marano and the ascending orbits show an almost identical spatial signal that indicates a range increase and hence a movement away from the satellite with more than 150 mm/year along the line-of-sight. The descending orbits, on the other hand, show a movement towards the satellite again with more than 150 mm/year along the line-of-sight. This difference can be interpreted as a gravitational deformation oriented along the downslope direction.

Compared to the Ca Lita landslide, the interferometric signal on the Marano earthflow is less noisy, due to lower displacement rates, but also possibly because of the different kinematics. While the Ca Lita landslide is dominated by roto-translational sliding in the upper part and flow-like deformation in the central and lower parts (Borgatti et al., 2006; Corsini et al., 2006), the Marano landslide appears to move as a relative coherent block along slope-parallel slip surface/s. Such behavior allowed us to successfully unwrap the Marano interferograms and extract velocity information for the period between the beginning of Sentinel acquisition and the failure (Fig.7, a).

The velocity series are obtained by simply dividing the displacement of each interferogram divided by the period between the two acquisitions that were used to form the interferogram. We used a local regression analysis to fit the data and detect associated trends (line in Fig.7, a). Before the launch of Sentinel 1B the frequency of velocity information is lower because only 12 and 24 days interferograms are available and few are selected due to coherence issues. This is why the trend before august 2016 is less defined. However, the most remarkable result is probably represented by the fact that the regression lines of the four independent datasets depict similar and coherent trends. In order to interpret such trends, we compare them to the precipitation regime. The rainfall data have been provided by the Regional Agency for Prevention, Environment and Energy of Emilia-Romagna (Arpae) and the snowfalls data have been recorded at the Porretta station, respectively four and eight kilometers far from the earthflow and at a comparable elevation. For each hydrological year (starting in October) we calculated weekly rainfall values and cumulated precipitations (including both rainfall and snowmelt; Fig.7 b).

During 2016 (October 2015 - September 2016) the only peak in velocity was resolved during

March, following a period of intense rainfalls: about 300 mm of rains occurred in the previous 60 days. In the following year intense snowmelt and rainfall cause the LOS displacement rates to exceed 100 mm/year in December 2016. In this case both ascending datasets and descending dataset 95 capture the velocity peaking. During spring 2017 two peaks of high velocities were registered, the first one occurred in March, while the second in May. The peaks are well registered by the ascending dataset 117 and the descending dataset 95, while the other two orbits do retrieve high displacement rates during spring but do not resolve two distinct peaks. Again, the velocity peaks follow two periods of precipitations with the first one being amplified by snowmelt.

During the dry summer of 2017 landslide velocities drop to almost null values along the line-of-sight, but with the onset of hydrological year 2017-2018, the landslide acceleration started almost synchronous with the first heavy precipitation of November 2017. The velocity continues to increase systematically until the failure of March 2018. Both the peak velocities as well as the slope of the velocity increases are higher compared to the previous years. Another difference between the period that precedes the failure and the years 2015-2017 is the fact that the snowmelt significantly contributes to increase the equivalent precipitation. In fact, the interferograms that directly precede or span the failure are heavily decorrelated all over the Reno catchment due to the presence of snow (3, b).

Once coherence is recovered (June 2018), the landslide is dormant and velocities are lower than they were during the years 2015-2017.

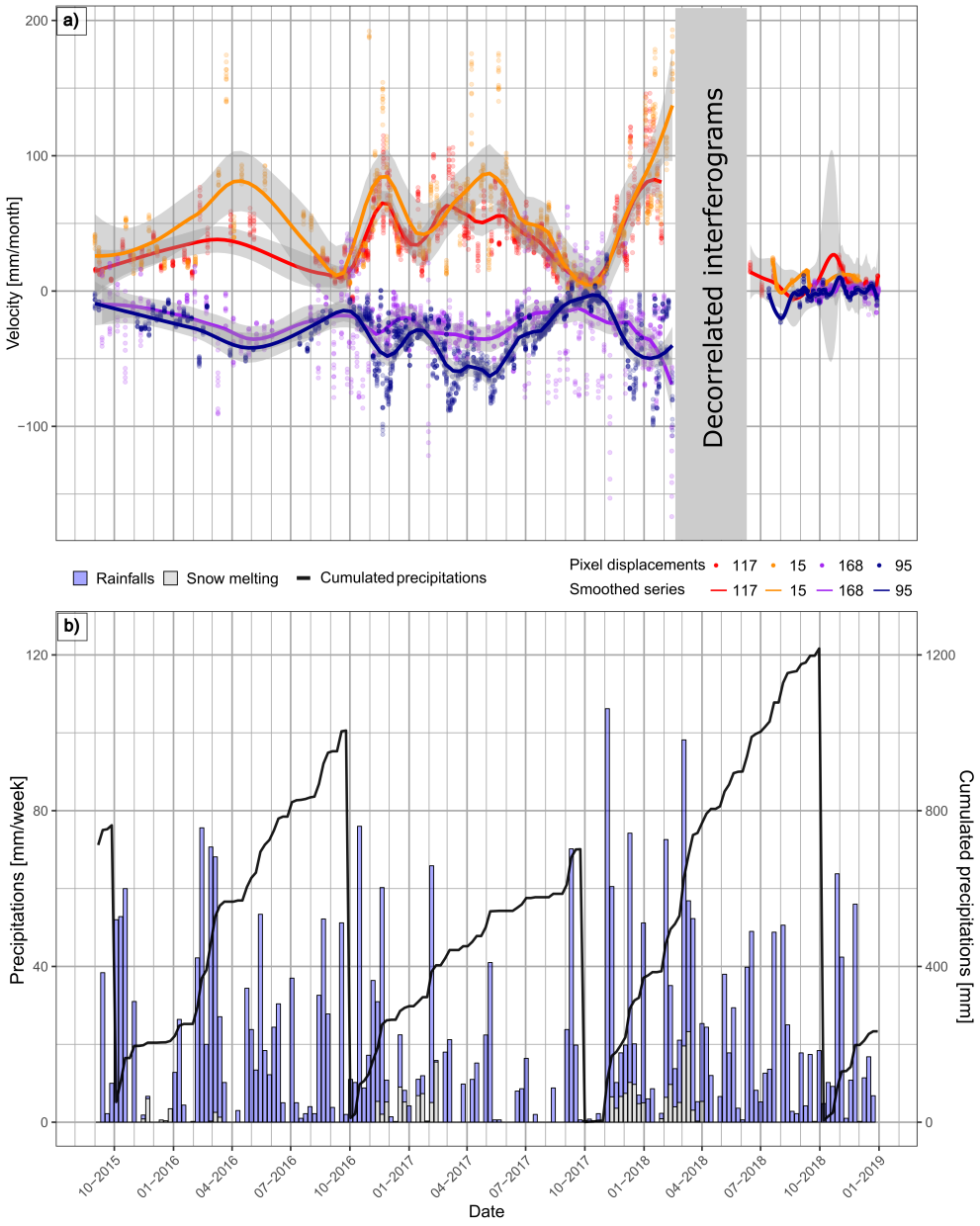

Figure 7: a) Velocity time series for each track at the Marano earthflow (positive values for ascending Tracks, negative values fo descending Tracks). The dot symbols represent the pixels belonging to the investigated area (see Fig.6); the lines are derived by applying a local regression smoothing using the implementation of the ggplot package that takes into account a neighbourhood of 20 % w.r.t. to complete series. The gray bands are the 95 percent confidence interval of the smoothing operation. The gray box highlights the time period in which interferograms are completely decorrelated either due to the presence of snow or due to high displacement rates during the failure. b) Weekly data of rainfall and snowmelt (left y-axes) are plotted together with the cumulated precipitation that contains rainfall and snow-melt(right y-axes): the series has been set to zero at the beginning of each hydrological year.

5. Discussion and conclusions

Interferometric analysis has been successfully applied to two slow-moving landslides that were subject to generalized failures during the period of our investigations. Both landslides are characterized by the scarce presence of man-made structures or rock-outcrops that could represent stable scatterers in multi-temporal InSAR analysis. We used standard two-pass interferometry (Handwerger et al., 2013, 2019) to detect deformation signals useful to document the evolution of the landslides in the 2015-2019 interval. The InSAR data allow appreciating the spatial pattern of deformation at successive time intervals that can be used to interpret the geometry and the kinematics of the landslide. In both cases, the deformation signal corresponds well to the areas that have been mapped by the regional landslide inventory as active landslide deposits. In the case of the Ca Lita landslide, the deformation maps evidence inhomogeneous deformation fields throughout the landslide deposit that can be used to interpret the kinematics of the phenomena. The InSAR data show that the pre-failure deformation at Ca Lita in 2017 was dominated by displacements localized in the upper part of the slope. This is consistent with the behavior described for previous reactivation of this landslide (Borgatti et al., 2006; Corsini et al., 2006). Fast displacements are spatially detected but obtaining quantitative results is associated with larger uncertainties due to the presence of residual noise and unresolvable phase jumps. Though not numerically accurate during the most active phases of landslide movement, interferograms, and stacked interferograms contain useful information to: i) identify movement against surrounding stable slopes; ii) document the spatial evolution of the movement.

Despite the overall high quality of the interferograms formed from Sentinel 1 scenes, we would like to remark the semi-quantitative significance of the displacement data obtained from standard InSAR analysis. Residual noise due to topography and atmosphere can, in fact, have a minor influence on the numerical displacement values that are obtained (Massonnet and Feigl, 1998; Bürgmann et al., 2000). Bigger accuracy issues are caused by localized pixel-scale shear zones resulting in phase jumps (Hu et al., 2019) and, more generally, by displacement rates approaching the limits of the technique (Rosen et al., 2000; Bürgmann et al., 2000). In the case of the Ca Lita landslide, different types of movement can be encountered (i.e. sliding in the upper part and flow-like movement in the lower central and lower parts; Borgatti et al., 2006; Corsini et al., 2006), displacement rates were often sustained in between the two failure episodes (March 2016

- December 2017) and possibly associated to high spatial small-scale variability due to flow-like type of movement. Hence a velocity-time series similar to the one of the Marano case could not be produced. A conceptual sketch in Fig. 8 a) illustrates that deformation exceeding approximately 120 mm/month cause signals in interferograms that are not correct from a numerical point of view. This is because interferograms with higher displacement rates cause interferograms similar to those in Fig. 8 b) that show multiple phase jumps in the landslide area. The signal can be clearly attributed to deformation since coherence is high throughout the rest of the image. It is however impossible to correctly count the interferometric fringes that occur in this interferogram on the whole landslide body, but it might succeed in some parts of it. There are also interferograms that are at the limit of decorrelation and have one or two phase jumps (Fig. 8 c). These type interferograms can be unwrapped by forward modeling the deformation. Because the Ca Lita landslide has numerous open crevices and fissures that appear to be secondary slip surfaces along which high differential displacements occurred in a small area. It is hence possible that also in those interferograms that apparently were correctly unwrapped, more than one or two phase jump has been undersampled. Since similar problems did not occur on the Marano landslide, we would like to point out that this is highly dependent on the displacement rates and the kinematics of the landslide and those interferograms like the one in Fig. 5 still contain very useful information regarding the area in displacement during a given period of time.

From a geological point of view, the two analyzed landslide differ in several aspects. The bedrock at Ca Lita is composed of flysch rocks in the upper part and chaotic clay shales in the lower part of the slope, while the Marano earthflow is hosted only by chaotic clay shales. This difference in the bedrock material might contribute to the fact that at the Ca Lita landslide different kinematics coexist, while Marano is an earthflow like many others in the clay-shales rocks of the Reno Catchment where flow-like morphology is associated to dominant sliding (Simoni et al., 2013).

The Marano earthflow remained in a dormant state for 20 years before it reactivated in March 2018. No damages were reported along the national road crossing the landslide at the toe nor by the land owners upslope. However, InSAR data document active deformation for at least two years before the failure occurred. Marano earthflow inerferograms indicate the coherent displacement of the existing landslide deposits. Velocity variations are well documened by four velocity time series that we derive for each available satellite track. It has been possible to detect displacement rates

ranging from virtually null values to more than 100 mm/month. The velocity time series show repeated and coherent velocity peaking that can be related to intense rainfalls. The limited number of acceleration episodes (3 to 4) detected during our InSAR analysis do not allow statistically significant cross-correlation analysis. However, the relationship with the precipitation regime is evident and strengthened by late summer marked a decline in velocity observed during 2016 and 2017. The main triggering factor is the precipitation regime during autumn 2017-spring 2018. The total amount of precipitation was significantly higher: 500 mm in the period between October 2017 and the failure (March 1st, 2018) most of them (100 mm) in the 30 days preceding the failure (Fig. 7). During the winter months, the snow cover was repeatedly present along the slopes. Snow melting contributed to significantly increase the equivalent precipitation both during November and December 2017 and February 2018 when, during the months preceding the failure, we calculate 80 mm of snow melting that is added to 340 mm of rain. Also, the hydrological year of 2017/2018 was preceded by an unusually dry summer which may have favored the formation of fissures and cracks on the landslide body increasing permeability and hence the infiltration of water (Malet et al., 2005).

Results obtained on both cases show that InSAR can deliver almost continuous deformation maps on landslides of the Northern Apennines that are characterized by moderate vegetation and high displacement rates ranging from extremely slow to about 100 mm/month. When the velocities approach the upper limit and/or the landslide shows highly variable (pixel-scale) spatial deformation pattern, phase jumps cannot be further solved. At lower values, velocities can be considered reliable though inherent uncertainties associated to residual (topographic, atmospheric) noise remain. Regardless of their numerical accuracy, InSAR-derived deformation maps supply a number of information about the spatial pattern and the temporal evolution of the landslides. In our cases, the generalized failure of slow-moving, apparently dormant earthflows was preceded by clearly detectable deformation whose trend could be related to the seasonal and monthly-to-weekly precipitation. Our data are not enough to constrain such relationship but indicate that multi-year InSAR analysis is suitable to investigate the process. The high acquisition frequency of Sentinel 1 and the large spatial extension of SAR scenes open also new perspectives in using this approach for large scale analysis.

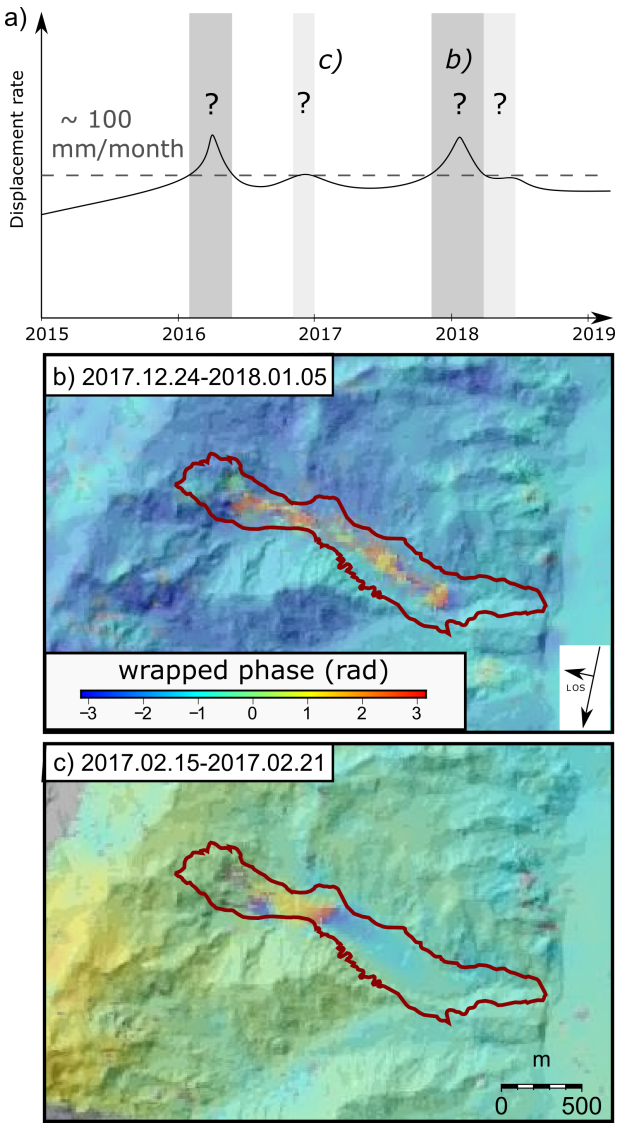

Figure 8: a) Conceptual sketch of the Ca Lita evolution. The dark gray boxes highlight periods in which several interferograms are decorrelated or display unwrapping problems because of fast displacement. The light gray boxes indicate periods in which displacement causes decorrelation in interferograms that span more than 12 days: the total number of decorrelated interferograms is slightly lower of that one referred to the dark gray boxes. The question marks in the gray boxes indicate the ambiguity of the displacement rate values if large decorrelation/unwrapping errors occur. In the other periods the velocity of the landslide is still often near to the upper limit and phase unwrapping may occurr. b) Example of wrapped interferogram with multiple phase jumps close to complete decorrelation ("fast-displacement decorrelation"). c) Example of wrapped interferogram (Track 168) with only one phase jump that can be solved in the unwrapping step. The labels on the top right indicate the temporal baselines of the two examples

Acknowledgments

We would like to thank Al Handwerger and Davide Marchioni for photos providing. Rainfall data were obtained from the Dexter download system of ARPA Emilia Romagna (http://www.smr.arpa.emr.it/dext3r/). We thank the European Space Agency for supplying Sentinel data.

References

Bayer, B., Simoni, A., Mulas, M., Corsini, A., Schmidt, D., 2018. Deformation responses of slow moving landslides to seasonal rainfall in the northern apennines, measured by insar. Geomorphology 308, 293–306.

Bayer, B., Simoni, A., Schmidt, D., Bertello, L., 2017. Using advanced insar techniques to monitor landslide deformations induced by tunneling in the northern apennines, italy. Engineering geology 226, 20–32.

Bennett, G.L., Roering, J.J., Mackey, B.H., Handwerger, A.L., Schmidt, D.A., Guillod, B.P., 2016. Historic drought puts the brakes on earthflows in northern california. Geophysical Research Letters 43, 5725–5731. doi:10.1002/2016GL068378.

Berardino, P., Fornaro, G., Lanari, R., Sansosti, E., 2002. A new algorithm for surface deformation monitoring based on small baseline differential sar interferograms. IEEE Transactions on Geoscience and Remote Sensing 40, 2375–2383.

Berti, M., Martina, M., Franceschini, S., Pignone, S., Simoni, A., Pizziolo, M., 2012. Probabilistic rainfall thresholds for landslide occurrence using a bayesian approach. Journal of Geophysical Research: Earth Surface 117.

Berti, M., Simoni, A., 2012. Observation and analysis of near-surface pore-pressure measurements in clay-shales slopes. Hydrological Processes 26, 2187–2205.

Bertolini, G., Casagli, N., Ermini, L., Malaguti, C., 2004. Radiocarbon data on lateglacial and holocene landslides in the northern apennines. Natural Hazards 31, 645–662.

Bertolini, G., Pellegrini, M., 2001. The landslides of the emilia apennines (northern italy) with reference to those which resumed activity in the 1994–1999 period and required civil protection interventions. Quad Geol Appl 8, 27–74.

Bianchini, S., Herrera, G., Mateos, R.M., Notti, D., Garcia, I., Mora, O., Moretti, S., 2013. Landslide activity maps generation by means of persistent scatterer interferometry. Remote Sensing 5, 6198–6222. doi:10.3390/rs5126198.

Borgatti, L., Corsini, A., Barbieri, M., Sartini, G., Truffelli, G., Caputo, G., Puglisi, C., 2006. Large reactivated landslides in weak rock masses: a case study from the northern apennines (italy). Landslides 3, 115.

Bürgmann, R., Rosen, P.A., Fielding, E.J., 2000. Synthetic aperture radar interferometry to measure earths surface topography and its deformation. Annual review of earth and planetary sciences 28, 169–209.

Carlà, T., Farina, P., Intrieri, E., Ketizmen, H., Casagli, N., 2018. Integration of ground-based radar and satellite insar data for the analysis of an unexpected slope failure in an open-pit mine. Engineering Geology 235, 39–52.

Castellarin, A., 1992. Strutturazione eo-e mesoalpina dell'appennino settentrionale attorno al" nodo ligure" .

Cervi, F., Ronchetti, F., Martinelli, G., Bogaard, T.A., Corsini, A., 2012. Origin and assessment of deep groundwater inflow in the ca' lita landslide using hydrochemistry and in situ monitoring. Hydrology and Earth

441 System Sciences 16, 4205–4221. URL: http://www.hydrol-earth-syst-sci.net/16/4205/2012/, doi:10.5194/
442 hess-16-4205-2012.
443 Chen, C.W., Zebker, H.A., 2001. Two-dimensional phase unwrapping with use of statistical models for cost functions
444 in nonlinear optimization. JOSA A 18, 338–351.
445 Colesanti, C., Ferretti, A., Prati, C., Rocca, F., 2003. Monitoring landslides and tectonic motions with the permanent
446 scatterers technique. Engineering geology 68, 3–14.
447 Colesanti, C., Wasowski, J., 2006. Investigating landslides with space-borne synthetic aperture radar (sar) interfer-
448 ometry. Engineering geology 88, 173–199.
449 Corsini, A., Borgatti, L., Caputo, G., De Simone, N., Sartini, G., Truffelli, G., 2006. Investigation and monitoring in
450 support of the structural mitigation of large slow moving landslides: an example from ca'lita (northern apennines,
451 reggio emilia, italy). Natural Hazards and Earth System Science 6, 55–61.
452 Cruden, D.M., Varnes, D.J., 1996. Landslides: investigation and mitigation. chapter 3-landslide types and processes.
453 Transportation research board special report .
454 Fattahi, H., Amelung, F., 2015. Insar bias and uncertainty due to the systematic and stochastic tropospheric delay.
455 Journal of Geophysical Research: Solid Earth 120, 8758–8773.
456 Ferretti, A., Fumagalli, A., Novali, F., Prati, C., Rocca, F., Rucci, A., 2011. A new algorithm for processing
457 interferometric data-stacks: Squeesar. IEEE Transactions on Geoscience and Remote Sensing 49, 3460–3470.
458 Ferretti, A., Prati, C., Rocca, F., 2001. Permanent scatterers in sar interferometry. IEEE Transactions on geoscience
459 and remote sensing 39, 8–20.
460 Fruneau, B., Achache, J., Delacourt, C., 1996. Observation and modelling of the saint-etienne-de-tinée landslide
461 using sar interferometry. Tectonophysics 265, 181–190.
462 Goldstein, R.M., Werner, C.L., 1998. Radar interferogram filtering for geophysical applications. Geophysical research
463 letters 25, 4035–4038.
464 Handwerger, A.L., Huang, M.H., Fielding, E.J., Booth, A.M., Bürgmann, R., 2019. A shift from drought to extreme
465 rainfall drives a stable landslide to catastrophic failure. Scientific reports 9, 1569.
466 Handwerger, A.L., Roering, J.J., Schmidt, D.A., 2013. Controls on the seasonal deformation of slow-moving land-
467 slides. Earth and Planetary Science Letters 377, 239–247.
468 Handwerger, A.L., Roering, J.J., Schmidt, D.A., Rempel, A.W., 2015. Kinematics of earthflows in the northern
469 california coast ranges using satellite interferometry. Geomorphology 246, 321–333.
470 Hilley, G.E., Bürgmann, R., Ferretti, A., Novali, F., Rocca, F., 2004. Dynamics of slow-moving landslides from
471 permanent scatterer analysis. Science 304, 1952–1955.
472 Hooper, A., 2008. A multi-temporal insar method incorporating both persistent scatterer and small baseline ap-
473 proaches. Geophysical Research Letters 35.
474 Hooper, A., Zebker, H., Segall, P., Kampes, B., 2004. A new method for measuring deformation on volcanoes and
475 other natural terrains using insar persistent scatterers. Geophysical research letters 31.
476 Hu, B., Chen, J., Zhang, X., 2019. Monitoring the land subsidence area in a coastal urban area with insar and gnss.
477 Sensors 19, 3181.
478 Intrieri, E., Raspini, F., Fumagalli, A., Lu, P., Del Conte, S., Farina, P., Allievi, J., Ferretti, A., Casagli, N., 2018.

The maoxian landslide as seen from space: detecting precursors of failure with sentinel-1 data. Landslides 15, 123–133.

Malet, J.P., van Asch, T.W.J., van Beek, R., Maquaire, O., 2005. Forecasting the behaviour of complex landslides with a spatially distributed hydrological model. Natural Hazards and Earth System Sciences 5, 71–85. URL: http://www.nat-hazards-earth-syst-sci.net/5/71/2005/, doi:10.5194/nhess-5-71-2005.

Marroni, M., Treves, B., 1998. Hidden terranes in the northern apennines, italy: a record of late cretaceous-oligocene transpressional tectonics. The Journal of geology 106, 149–162.

Massonnet, D., Feigl, K.L., 1998. Radar interferometry and its application to changes in the earth's surface. Reviews of geophysics 36, 441–500.

Panini, F., Bettelli, G., Bonazzi, U., Gasperi, G., Fioroni, F., Fregni, P., 2002. Note illustrative alla Carta Geologica dItalia a scala 1:50.000. Foglio N. 237, Sasso Marconi.

Papani, G., De Nardo, M., Bettelli, G., Rio, D., Tellini, C., Vernia, L., Fornaciari, E., Iaccarino, S., Martelli, L., Papani, L., et al., 2002. Note illustrative della carta geologica ditalia alla scala 1:50.000, foglio 218, castelnuovo ne monti. EL. CA. Firenze, Servizio Geologico dItaliaRegione Emilia Romagna .

Patacca, E., Sartori, R., Scandone, P., 1993. Tyrrhenian basin and apennines. kinematic evolution and related dynamic constraints, in: Recent Evolution and Seismicity of the Mediterranean Region. Springer, pp. 161–171.

Picarelli, L., Urciuoli, G., Ramondini, M., Comegna, L., 2005. Main features of mudslides in tectonised highly fissured clay shales. Landslides 2, 15–30.

Raspini, F., Bianchini, S., Ciampalini, A., Del Soldato, M., Montalti, R., Solari, L., Tofani, V., Casagli, N., 2019. Persistent scatterers continuous streaming for landslide monitoring and mapping: the case of the tuscany region (italy). Landslides 16, 2033–2044. URL: https://doi.org/10.1007/s10346-019-01249-w, doi:10.1007/s10346-019-01249-w.

Servizio Geologico Sismico e dei Suoli della Regione Emilia-Romagna, R.E.R., 2019. Archivio storico delle frane della regione emilia-romagna. URL: http://geo.regione.emilia-romagna.it/schede/fs/fs_dis.jsp?id=60575.

Roering, J.J., Stimely, L.L., Mackey, B.H., Schmidt, D.A., 2009. Using dinsar, airborne lidar, and archival air photos to quantify landsliding and sediment transport. Geophysical Research Letters 36.

Rosen, P.A., Hensley, S., Joughin, I.R., Li, F.K., Madsen, S.N., Rodriguez, E., Goldstein, R.M., 2000. Synthetic aperture radar interferometry. Proceedings of the IEEE 88, 333–382.

Royden, L., Patacca, E., Scandone, P., 1987. Segmentation and configuration of subducted lithosphere in italy: An important control on thrust-belt and foredeep-basin evolution. Geology 15, 714–717.

Sandwell, D., Mellors, R., Tong, X., Wei, M., Wessel, P., 2011. Open radar interferometry software for mapping surface deformation. Eos, Transactions American Geophysical Union 92, 234–234.

Schmidt, D.A., Bürgmann, R., 2003. Time-dependent land uplift and subsidence in the santa clara valley, california, from a large interferometric synthetic aperture radar data set. Journal of Geophysical Research: Solid Earth 108.

Simoni, A., Ponza, A., Picotti, V., Berti, M., Dinelli, E., 2013. Earthflow sediment production and holocene sediment record in a large apennine catchment. Geomorphology 188, 42–53.

Tarayre, H., Massonnet, D., 1996. Atmospheric propagation heterogeneities revealed by ers-1 interferometry. Geophysical Research Letters 23, 989–992.

517 Tofani, V., Raspini, F., Catani, F., Casagli, N., 2013. Persistent scatterer interferometry (psi) technique for landslide
518 characterization and monitoring. Remote Sensing 5, 1045–1065. doi:10.3390/rs5031045.
519 Wasowski, J., Bovenga, F., 2014. Investigating landslides and unstable slopes with satellite multi temporal interfer-
520 ometry: Current issues and future perspectives. Engineering Geology 174, 103–138.
521 Zebker, H.A., Rosen, P.A., Hensley, S., 1997. Atmospheric effects in interferometric synthetic aperture radar surface
522 deformation and topographic maps. Journal of geophysical research: solid earth 102, 7547–7563.
523 Zebker, H.A., Villasenor, J., 1992. Decorrelation in interferometric radar echoes. IEEE Transactions on geoscience
524 and remote sensing 30, 950–959.

7. CONCLUSIONS

In the published works, results from multiple Rayleigh wave surveys have been considered. Rayleigh wave velocity measurements provide a deep insight into the mechanic of the earthflows. The Rayleigh wave surveys can be carried out both using “active” (i.e. MASW technique) and “passive” (i.e. ReMi technique) methods. The analysis of the Rayleigh waves allows detecting stiffness properties of the soils, as appears from Paper 1 and 2. From the papers it appears that a fluidization process occurs during the rapid acceleration phase: the soil stiffness decreases probably due to the rainfall infiltration combined with the material remolding. In the time following the rapid surging the earthflow deposits become stiffer and the measured shear wave velocities increase.

Stiffness trends over time have been derived and compared with other available information. From the analysis of these trends, we can infer the following conclusions:

- During the rapid acceleration that characterizes the sudden reactivation stage, the stiffness of the material shows a significant drop in soil stiffness. The same drop doesn’t occur in the soils outside the failed mass.
- Some days after the abrupt surging the stiffness of the material involved in the earthflow reactivation starts to increase.
- It’s possible to observe how stiffness measured inside the earthflows tends asymptotically to the values measured outside.

Earthflow fluidization means a transition from a grain-supported to a fluid-supported soil structure. If we consider saturated soils as those we dealt with, the water content corresponds to the porosity: variations in porosity (or in void-ratio) can be used to infer a probable fluidization process. Thus, to assess whether stiffness variation is related to the hypothesized solid-to-fluid transition or not, we need to consider how the void-ratio varies over time.

Void-ratio is directly related to shear stiffness, but the field condition didn’t enable us to derive a full-validated relationship between soil stiffness and void-ratio: the several types of stiffness – void-ratio relations provided in the literature might not apply to our field conditions. However empirical equations (Santos and Correya, 2000) have been used to estimate void-ratio trends over time. The results can be interpreted only from a qualitative point of view, but they help to better understand the earthflows behavior. The obtained distributions have been fitted by consolidation curves provided by the Terzaghi consolidation theory (Terzaghi, 1943): the curves have been calibrated by using different realistic values of coefficients of consolidation. We derive that:

- Void-ratio is high just after the rapid surging and tends to decrease in the following period.
- The void-ratio trends over time can be fitted by consolidation curves that can be representative of clayey soils (Holtz and Kovacs 1981).
- If the void-ratio tends to decrease after the failure in the displaced mass, probably during the failure the reverse process occurs.

By the points stated above, during rapid motion earthflows undergo a strong increase of soil porosity that, for which concerns saturated soils, means an increase of water content. That conclusion is consistent with a fluid-like behavior occurring during the rapid surging.

However, void-ratio trends can be taken into account only in a qualitative way. The lack of field data during the reactivation stage didn't allow us to infer a proper function between soil stiffness and void-ratio.

So, following the aim of the current work, other ways have been investigated using different approaches, demonstrating that an integrated study could be more than necessary in our investigations.

First of all, other types of information confirm a likely fluid-like behavior during the rapid surging: for example, if we observe the velocity distributions in the earthflow surface, we can infer that the displacing mass didn't move like a rigid-body during the rapid surging. At the same time, data gathered far from the rapid acceleration show a stiffness increase. Thus, it reasonable to suggest that after a first period in which the mass fluidizes (i.e. the rapid surging stage), the deposits become stiffer and the deformation is probably bounded to narrower shear zones. The full behavior can be explained by the Iverson theory (Iverson, 1985; 1986a, 1986b), but, once again, the lack of data during the rapid acceleration stage is an obstacle to derive a realistic model.

The lack of information during the fast acceleration led us to think that we need a valid method to investigate earthflow before the rapid surging. In this sense conventional two-pass interferometry has proved to be a valid method: the application of that technique to two earthflows that move relatively fast even during the so-called dormant periods provides enough information about the deformation patterns in the periods before the sudden accelerations. In particular, results presented in Paper 3 show that it's possible to obtain continuous deformation maps of earthflows, even if they are characterized by moderate vegetation and relatively high displacement rates. A key role is played by the quality of raw data that allowed us to perform valid stacking processing and build a valid deformation model to improve the quality of the computed

interferograms. Thus, Sentinel data can be exploited in order to study the pre-failure stages and derive useful information about the deformation patters of the large earthflows located in this area.

Matching all the parts of this work provides an overview of the mechanics of active earthflows: fluid-like behavior happens during the fast acceleration (meters per day) because of soil remolding and water content increase; when the displacing mass slows down the materials become stiffer and during periods of slow motion (millimeters per month) the rigid-like behavior prevails. To really examine the problem field data are necessary: remote sensing techniques as conventional two-pass interferometry give a contribution in this sense.

The field data need remains a focal point. Future developments in studying earthflows behavior should be achieved if properties in reactivating soils are investigated. Measuring the proper water content of fast-moving materials can be the real challenge; also finding a field-relationship between soil stiffness and water content can improve the state of art about the reactivation issue. Exploiting InSAR data could provide the necessary information for starting field surveys: continuous monitoring of landslide-prone areas helps to overcome the problems relating to the detection of the correct place and time in which the rapid acceleration may occur; in such situation recovering field data during the reactivation stage should be easier. At the same time investigating directly the existing relationship between Rayleigh wave velocity and the water content could be a valid method to enhance more the data gathered by using seismic devices. In this sense laboratory tests can play an important role. Laboratory devices for shear wave measuring have been used since the late 1970s (Shirley and Hampton, 1978) but the relationship between Rayleigh wave velocities and soil water content is an issue still not very explored. Only in the last years some authors (Mainsant et al., 2012; Mainsant et al., 2015; Chen et al., 2018) started to investigate the topic showing how the water content affects the shear wave velocity response. Further investigation about that relationship can improve the interpretation of Rayleigh survey results.

References

Chen, Y., Irfan, M., Uchimura, T., Cheng, G., & Nie, W. (2018). Elastic wave velocity monitoring as an emerging technique for rainfall-induced landslide prediction. *Landslides*, *15*(6), 1155-1172.

Holtz, R. D., & Kovacs, W. D. (1973). An Introduction to Geotechnical Engineering., 1981. *Peck, RB, Hanson, WE and Foundation Engineering*.

Mainsant, G., Jongmans, D., Chambon, G., Larose, E., & Baillet, L. (2012). Shear-wave velocity as an indicator for rheological changes in clay materials: Lessons from laboratory experiments. *Geophysical research letters*, *39*(19).

Mainsant, G., Chambon, G., Jongmans, D., Larose, E., & Baillet, L. (2015). Shear-wave-velocity drop prior to clayey mass movement in laboratory flume experiments. *Engineering geology*, *192*, 26-32.

Santos, J. A., & Correia, A. G. (2000). Shear modulus of soils under cyclic loading at small and medium strain level. In *12th World Conference on Earthquake Engineering* (pp. 1-8).

Shirley, D. J., & Hampton, L. D. (1978). Shear-wave measurements in laboratory sediments. *The Journal of the Acoustical Society of America*, *63*(2), 607-613.

Terzaghi, K. (1943). Theoretical Soil Mechanics. JohnWiley & Sons. *New York*, 11-15.

A) APPENDIX: ACCELERATION POINT DETECTION

The displacement series of each target (Figure A.1) has been treated in order to detect the point at which the “acceleration information” (e.g. the perturbation; see Chap. 5) reaches the target itself.

The two activations have been identified and considered independently (Figure A.1). Some targets dislocated of about meters or tens of meters and other ones of only a few centimeters; some targets were still before the rapid surging, other ones had been kept moving slowly for months before the acceleration. Therefore, it has been necessary to establish a method that could be valid for all the situations. Hence, here, the point at which the “acceleration information” reaches the interested target is defined as the acceleration peak in a specific time window. Specifically, the time window has been selected as a 30-days period belonging to a larger period in which there is at least one point accelerating. In each window, for each target, the acceleration peaks have been detected: the highest peak is the “acceleration point”. If there is no acceleration peak significantly higher than others, or the displacement series is not continuous in the considered time window, the target is considered as a “not-accelerating target”. The time window has been rolled forward as long as “accelerating targets” have been detected in order to asses if the selection of the peaks was correct and there were not missed “accelerating targets”.

The algorithm has been developed following the scheme:

1) Time window definition: the two activation stages have been identified.
2) Displacement data interpolation: since the series have been recorded using different sample rate, the data have been interpolated hourly in order to apply the same processing to all the series.
3) Data smoothing: to exclude the artificial spikes that sometimes affect the series, the data belonging to the specific time window have been smoothed. Locally estimated scatterplot smoothing (LOESS filter) with windows large about the 10% of the data length has been applied to the series characterized by large displacements (less level of noise). Higher LOESS filter (windows width of about 40%) has been applied to the series characterized by low displacements (noisier).
4) Acceleration series: twice-differentiation has been performed to obtain the acceleration series for each target in the defined time window.
5) Maximum acceleration peak detection: the “acceleration point” for each series has been detected as instant at which the acceleration is max (Figure A.2)

6) Residual noisy series, not continuous ones and not-accelerating ones, have been discarded (Figure A.3)

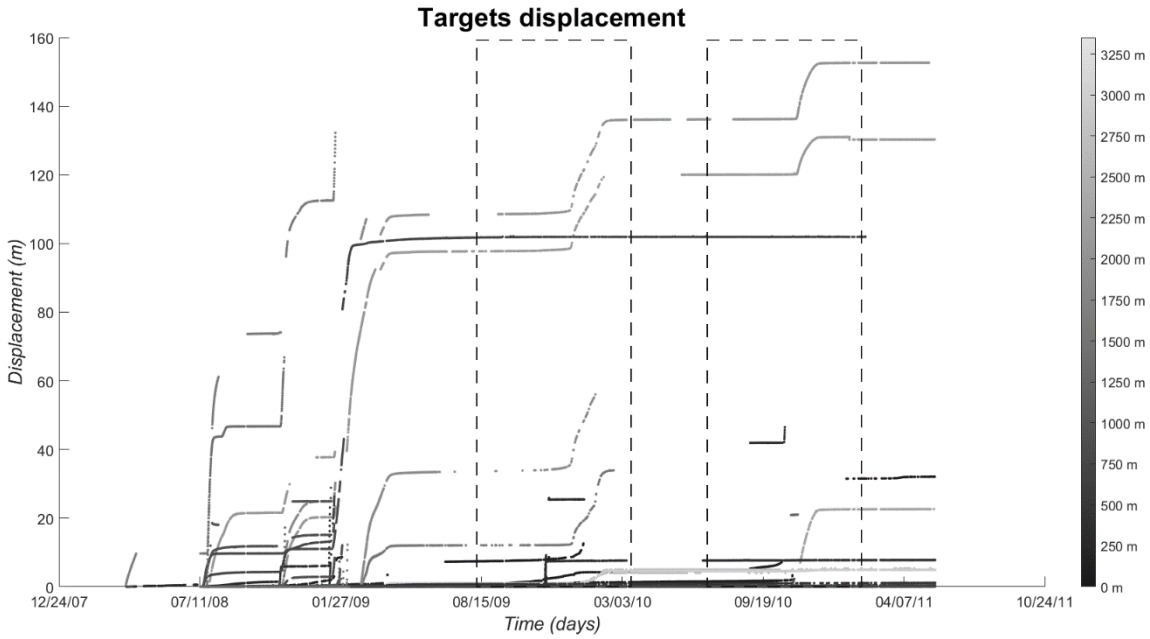

Figure A.1: Displacement series of all the targets. The dashed rectangles identify the two investigated reactivations. The gray scale represents the distance of the targets from the headscarp along the landslide profile. The displacement data of the targets which dislocated only few centimeters is not evident because of the y-axes scale.

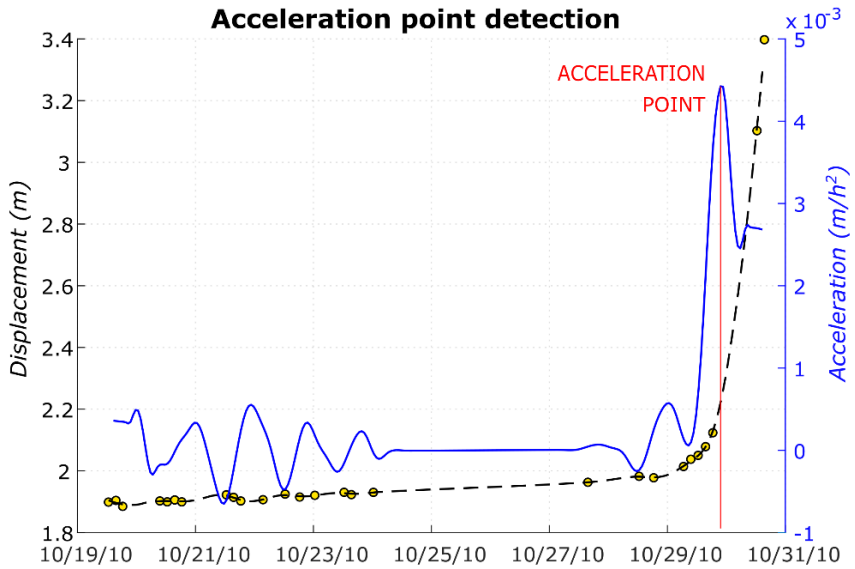

Figure A.2: Identification of the "acceleration point". The yellow dots represent the measured displacement data; the dashed black line is the resampled and smoothed displacement series; the blue line is the derived acceleration series; the acceleration point is marked by the red line.

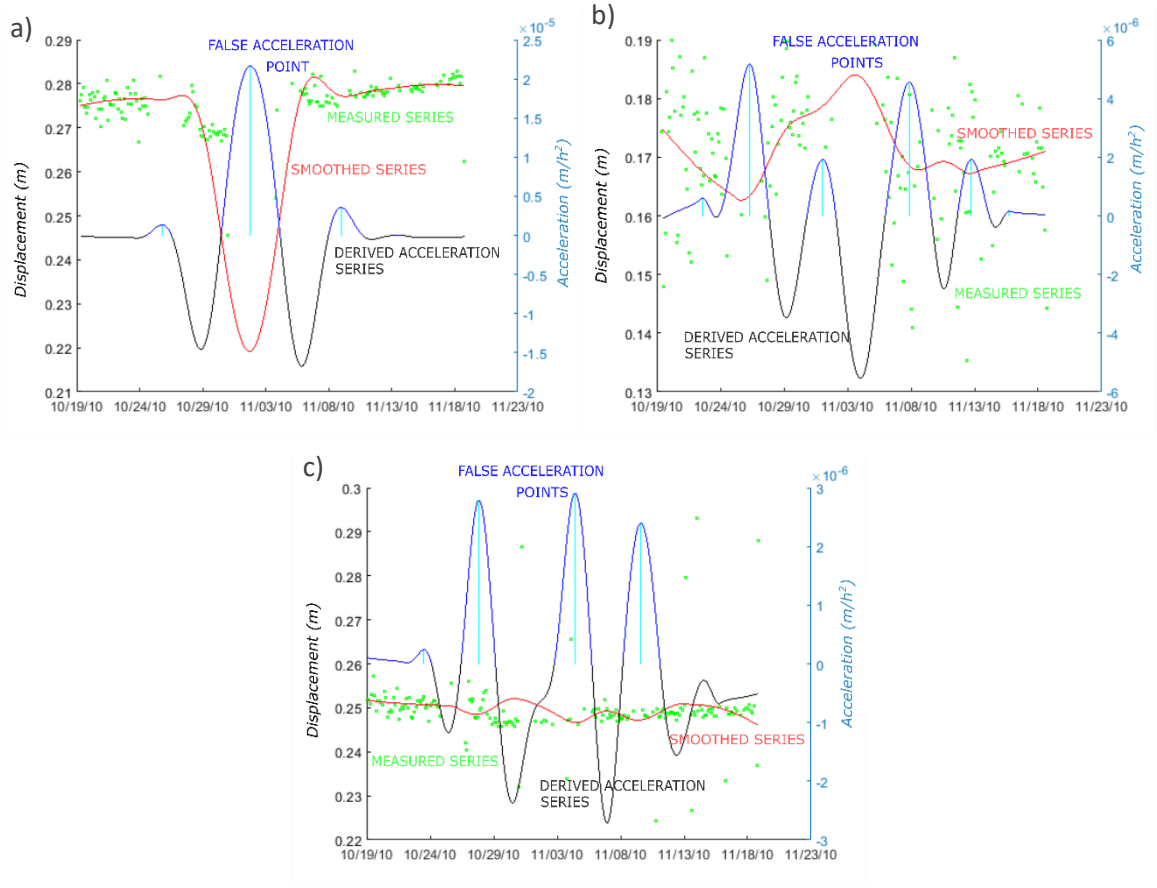

Figure A.3: Examples of series that have been discarded. a) discontinuous series: the acceleration peak derives from a bad smoothing computation of the displacement data; b) scattered series: the acceleration series is affected by the scattering properties of the series that are reflected in the smoothing curve; c) not-accelerating series: in a data not showing a real acceleration the presence of some artificial spikes affects the smoothing series and thus the acceleration series.

B) APPENDIX: FRAMES ANALYSIS

PIVlab is a time-resolved particle image velocimetry (PIV) software that can be used to compute the velocity distribution within particle image pairs. This method is typically applied calculating instantaneous velocities in fluids (Thielicke, 2014; Thielicke and Stamhuis, 2014).

It has been developed in the Matlab environment and can be used for different purposes. The user is allowed to select the region of interest, the proper scale of the image and the type of result visualizations he wants to get. The region of interest and the size of the grid in which the region of interest is split are defined by the user too. The software is configurated in multiple scripts that are called in the "command line" script. The part of the software that computes the displacements between consequent frames is built in the "piv_FFTmulti.m" script: it uses the cross-correlation method to compute the displacement for each element of the grid ("interrogation area"). The user can choose how to apply the cross-correlation method, whether in the spatial domain or the frequency domain. We selected the latter approach: the correlation matrix is computed in the frequency domain using a Fast Fourier Transform (FFT). FFT assumes that the input datasets (interrogation areas) are periodic, hence that they repeat themselves in all directions: if particle displacement is larger than half the size of the interrogation area, the intensity will appear on the opposite side of the area. In PIVlab this problem is overcome by running several passes of the analysis on the same dataset: the first pass uses large interrogation areas and can accept large particle displacements, in the following passes the area is reduced and displaced at the same time (Thielicke, 2014; Thielicke and Stamhuis, 2014). This method yields a high spatial resolution. The number of passes for the process iterating and the size of the reduced area are chosen by the user.

Here, one of the post-processing PIVlab scripts has been slightly modified to take into account the major component of the perspective effect: two different scaling objects are required and different scaling coefficient is computed for each pixel, using a linear relationship between the pixel size and the distance.

The analysis is carried out by performing the following steps:

1) Input definition:
- Image type (i.e. file extension) and source directory selection
- Definition of the region of interest (Figure B.1)
- Scale defining by clicking on the vertices of two size-known objects

- Selection of the number of passes and the size of the interrogation areas of each pass (Figure B.1)

2) Pre-processing (Figure B.2):

- Contrast limited adaptive histogram equalization (CLAHE; Pizer et al., 1987): the most frequent intensities of the image histogram are spread out to the full range of the data; it works on small sub-images so that regions with low exposure and regions with high exposure are optimized independently
- High-pass filter: it emphasizes the particle information in the image and suppresses any low-frequency information
- Intensity capping: bright spots within the area will contribute statistically more to the correlation signal, which may bias the result in non-uniform flows; hence, an upper limit of the greyscale intensity is imposed and all pixels that exceed the threshold are replaced by this upper limit

3) Processing:

- Fast Fourier Trasform: switch from spatial domain to frequency domain
- Cross-correlation: interrogation areas of identical size are cross-correlated and the resulting correlation matrix is used to detect the displacements

4) Post-processing:

- By using the size of the scaling objects, a scaling factor for each pixel is computed
- The scaling factors are used for obtaining scaled displacements

The result is a displacement distribution over the region of interest (Figure B.3).

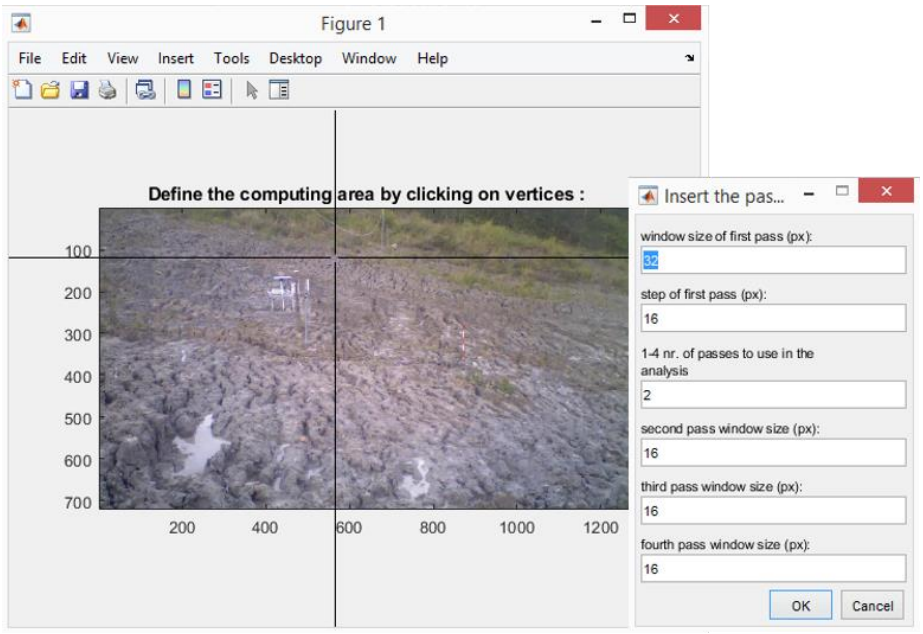

Figure B.1: Example of some input parameters definition.

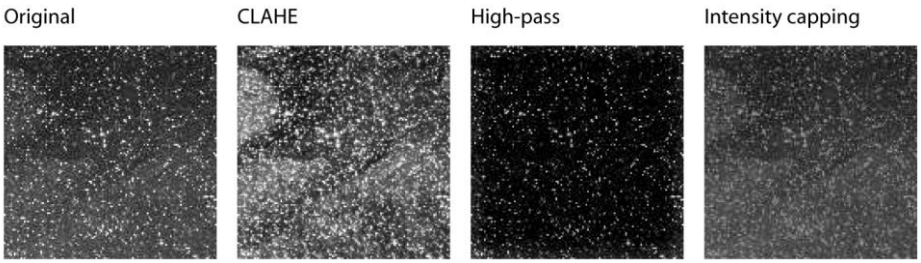

Figure B.2: Effects of the application of the filters during the pre-processing step (Thielicke and Stamhuis, 2014)..

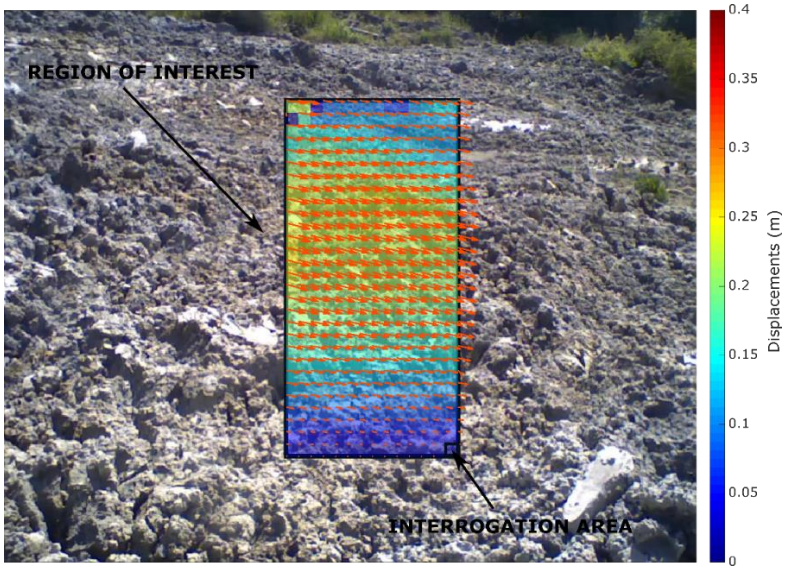

Figure B.3: A typical result of a PIVlab analysis. The orange arrows are the displacement vectors. The region of interest is colored by the displacement intensity values.

References

Pizer, S. M., Amburn, E. P., Austin, J. D., Cromartie, R., Geselowitz, A., Greer, T., ... & Zuiderveld, K. (1987). Adaptive histogram equalization and its variations. *Computer vision, graphics, and image processing*, *39*(3), 355-368.

Thielicke, W. (2014). *The flapping flight of birds: Analysis and application*. University of Groningen.

Thielicke, W., & Stamhuis, E. (2014). PIVlab–towards user-friendly, affordable and accurate digital particle image velocimetry in MATLAB. *Journal of Open Research Software*, *2*(1).

ACKNOWLEDGEMENTS

Three years of PhD studies allowed me to know a bit of the “mysterious” scientific world. I would like to thank my advisor Matteo Berti for the opportunity he gave to me to discover this world, and all the applied geology group for all the discussions and scientific exchanges: in particular, I would say thank you to Benedict Bayer and Alessandro Simoni who helped me in the last months of the PhD period. Thanks also to Lara Bertello, Silvia Franceschini and Wei Shen; thanks to Martino, Matteo, Marco, Cicca, Andrea and all the people I met during the field works: they really helped me in having a different perspective about the PhD.

I would like to thank my friends here for all the support in the difficult situations, for the serious and funny moments we spent together, for the lunch breaks, the coffee breaks, and the “happy hour breaks”: thanks to Maria, Giulia, Leo, Carlotta, Bianca, and Bruno. Many thanks also to my friends outside the department, who supported me even from far away, giving me wise advice.

I started this journey several years ago when I applied for a bachelor’s degree here in Bologna. It seems to me that it's been a long time and the last three years, the PhD years, had been longer than ever. Thus, I really want to say thank you to those who make this period as easy as possible. First of all, thanks to Veronica: all her advice has been useful, and her support has been essential; thanks again to Matteo who taught me a lot, from different points of view; thanks to Jerry, Fede, and Ale: even in three very different ways, they always remembered me why I had chosen this way; finally, thanks to all the “old” professors who, without knowing, helped me a lot.

The last “thank you” is for my family. Even if they have been facing problems of very different sizes, during these three years they never stopped to listen to my empty complaining, supporting and encouraging me for all my choices: thank you.